The Cooling of High-Magnetic-Field Pulsars

Weiwei Zhu
Department of Physics
McGill University
Montréal, Québec
Canada

A Thesis submitted to the
Faculty of Graduate Studies and Research
in partial fulfillment of the requirements for the degree of
Doctor of Philosophy

© Weiwei Zhu, 2010

Contents

List of Figures

LIST OF TABLES

Abstract

Prior to $\sim$ 20 years ago, only two kinds of pulsars were known: Rotation-powered Pulsars (RPPs) and accretion-powered pulsars. The rapid advance of X-ray astronomy in the past few decades has led to the discovery of magnetic-powered pulsars, namely "magnetars". Magnetars were first identified with the Soft Gamma Repeaters (SGRs) which exhibit sporadic soft gamma-ray bursts. More recently, another group of pulsars, the Anomalous X-ray Pulsars (AXPs), characterised by their bright persistent X-ray emission that is more powerful than their spin-down luminosity, were also recognized as members of the magnetar family. Both SGRs and AXPs have very high (10^{14}–10^{15} G) magnetic fields as inferred from their spin-down. Studying AXP behaviour might help us understand the physics of magnetars and their connections with normal pulsars.

In Chapter 3, I present our work on the X-ray afterglow of the AXP 1E 2259+586. It is the first AXP to exhibit a SGR-like outburst. It went through a major outburst in 2002. We studied the X-ray afterglow of this outburst, using ten *XMM* observations taken before and after the outburst. We found that the AXP's flux decayed following a power-law of index -0.69 ± 0.03, remarkably similar what was found from the afterglow of some SGR outbursts. We also found a strong correlation between spectral hardness and X-ray flux, as seen in other AXPs. In Chapter 4 I present our work on searching for X-ray variability from the glitching AXP 1E 1841$-$045. This is one of the most frequent glitchers among AXPs. Magnetar theories and observations suggest that there could be a connection between magnetar glitches and their X-ray variability. However, we found no evidence of glitch-related X-ray variability from archival X-ray data of 1E 1841$-$045 taken between 1993 and 2006. Our finding supports the existence of radiatively silent glitches in AXPs.

Interestingly, there is also a group of RPPs that have spin-down magnetic fields close to those of the magnetars ($\sim 10^{13}$ G). These high-magnetic-field RPPs may share some observational properties with the magnetars. In Chapter 5, I present the first X-ray detection of the high-magnetic-field RPP B1916+14. We found that the pulsar's emission is likely thermal, with a surface temperature in the range of 0.08–0.23 keV. We did not detect pulsations in the data, and set a 1σ upper limit on the pulsed fraction in the 0.1–2 keV band of $\sim$0.7. The origin of the thermal emission is not well constrained. We cannot rule out initial cooling or return current heating for this

pulsar. To look for evidence of magnetic-field-decay heating, a deeper observation is needed. In Chapter 6, I present our work on *Chandra* X-ray observations of the high-magnetic-field RPP J1718−3718. We detected X-ray pulsations at the pulsar's period with 52%±13% pulsed fraction in the 0.8–2 keV band. We found, from a merged spectrum of multiple observations, a blackbody temperature of 0.19±0.02 keV, slightly higher than predicted by standard cooling models. However, the best-fit neutron star atmosphere model is consistent with standard cooling. We also found that the pulsar's bolometric luminosity represents 0.3 of its spin-down power, assuming a distance of 4.5 kpc. Finally, we compared the blackbody temperatures measured for the high-magnetic-field pulsars with those from low-magnetic field rotation-powered pulsars of the same age, and found evidence of the former being on average hotter than the latter, as predicted by magneto-thermal evolution models that attempt to unify high-magnetic-field RPPs with magnetars.

Résumé

Il y a $\sim$20 ans, seulement deux sortes de pulsars étaient connues: ceux dont la source de lunimosité est leur énergie rotationelle et ceux dont la source de luminosité est l'accrétion. Dans les décennies récentes, les progrès rapides de l'astronomie des rayons-X ont permis de découvrir des pulsars dont la source de luminosité est l'énergie magnétique. Ces pulsars sont appelés magnétars. Les premiers magnétars découverts correspondaient aux répéteurs gamma doux (SGR). Ce sont des pulsars d'oú proviennent des pulsations occasionelles de rayons gammas. Plus tard, d'autres magnétars ont été découverts: les pulsars X anormaux (AXP). Ces derniers sont caractérisés par une luminosité en rayons-X qui est plus grande que leurs pertes d'énergie rotationelle. Les SGR et les AXP ont un champs magnétique élevé (10^{14}–10^{15} G) déterminé à partir du taux de ralentissement de leurs rotations. Étudier les AXP pourrait accroître notre compréhension des magnétars et celle de la relation entre les magnétars et les pulsars normaux.

Dans le chapitre 3, je présente mon travail sur la lueur résiduelle de AXP 1E 2259+586. Il s'agit du premier pulsar anormal à partir duquel des pulsations similaires à celles des SGR ont été détectées. Ce pulsar a eu un sursaut énergétique majeur en 2002. Nous avons étudié la lueur résiduelle de ce sursaut àu travers 10 observations faites avec le télescope *XMM* prises avant et après le sursaut. Nous avons trouvé que le flux du pulsar a diminué en suivant une fonction de puissance dont l'indice, -0.69 ± 0.03, est remarquablement similaire à celui trouvé dans le rayonnement résiduel des sursauts des SGR. Nous avons aussi trouvé une corrélation entre la dureté du spectre et le flux en rayons-X, une corrélation qui est aussi observée dans d'autres AXP.

Dans le chapitre 4, je présente mon travail sur la recherche de variations dans la luminosité-X de AXP 1E 1841−045. Ce pulsar est parmi les AXP qui présentent le plus fréquemment des sauts de fréquences, ou glitchs. Plusieurs théories des magnétars suggèrent une connection entre les glitchs et la variation de la luminosité-X. Malgré celà, nous n'avons pas trouvé de preuve de l'éxistence de ces variations dans la luminosité-X de 1E 1841−045 dans des observations prises entre 1993 et 2006 avec des télescopes variés. Ceci démontre l'existence de glitchs silencieux.

Il est intéressant de noter qu'il existe un groupe de pulsars normaux, dont la source de luminosité est leur énergie rotationelle, qui ont un champ magnétique élevé

et proche de celui des magnétars ($\sim 10^{13}$ G). Certaines caractéristiques de ces pulsars à champ magnétique élevé sont similaires à celles des magnétars. Dans le chapitre 5, je présente la première détection en rayons-X du pulsar à champs magnétique élevé B1916+14. Nous avons trouvé que le spectre d'émission de ce pulsar est probablement thermique, avec une température de surface entre 0.08–0.23 keV. Nous n'avons pas détecté de pulsations régulières dans les données, avec une limite supérieure (1σ) de ∼0.7 sur la fraction pulsée entre 0.1 et 2 keV. Il est aussi difficile de déterminer si le spectre d'émission thermique observé est dû à un refroidissement initial ou à un courant qui réchauffe la surface du pulsar en ce moment. C'est pourquoi plus d'observations sont requises afin de prouver que le réchauffement de la surface est dû à une diminution du champ magnétique.

Dans le chapitre 6, je présente mon travail effectué sur des observations faites avec le télescope *Chandra* du pulsar a champ magnétique élevé RPP J1718−3718. Nous avons détecté des pulsations régulières en rayons-X à un interval égal à celui de la fréquence rotationelle de ce pulsar et avec une fraction pulsée de 52%±13% entre 0.8 et 2 keV. Nous avons trouvé, en étudiant le spectre combiné de plusieurs observations, une température de corps noir de 0.19±0.02 keV. C'est une température un peu plus élevée que celle prédite par les modéles standards de refroidissement. Par contre, les modèles numériques d'atmosphère des étoiles à neutrons est en accord avec les modèles standards de refroidissement. Nous avons aussi trouvé que la luminosité bolométrique représente 0.3 de la puissance due à la perte d'énergie rotationelle, si l'on suppose une distance de 4.5 kpc. Finalement, nous avons comparé les températures de corps noirs des pulsars normaux à champ magnétique élevé avec ceux de pulsars normaux du même âge ayant un champ magnétique faible, et nous avons trouvé que les premiers avaient des températures plus élevées, comme le prédisent les modèles magnéto-thermiques ayant comme but d'unifier les pulsars normaux à champs magnétiques élevés et les magnétars.

Acknowledgments

I want to thank my supervisor Vicky Kaspi, for taking me as her student, guiding me through my PhD study, helping me with my English, and for always being so patient and kind to me. I would like to thank my collaborators, Marjorie Gonzalez, Rim Dib, Peter Woods, Fotis Gavriil, Andrew Lyne, Maura McLaughlin, George Pavlov, Stephen Ng, Dick Manchester and Bryan Gaensler for help proposing the observations and for their comments and suggestions for the papers. I thank the under-graduate students, graduate students and post-docs in McGill pulsar group for the wonderful five years, for creating such a friendly environment, and for all the helps and suggestions I received from the group meetings and the neutron star discussions, and for the delicious cookies and pizzas. I thank Anne Archibald and Patrick Lazarus for introducing `python` to me. Special thanks to Rim Dib for translating the thesis abstract into French, to Maggie Livingstone and Antoine Bouchard for reading the thesis manuscript, and to Stephen Ng for helping me with my latex and other software issues. Thanks to Paul Mercure and Juan Gallego for fixing my computer numerous times. Finally, I would like to thank my parents, my wife and my friends for their love and support.

Preface

Statement of Originality and Contribution of Authors

This thesis is a collection of papers published in the *Astrophysical Journal* (Chapters 3, 4, 5 and 6). Each paper reports new and original results based on X-ray observations of a magnetar or a high-magnetic-field rotation powered pulsar. Here we list the contributions of the various co-authors.

Chapter 3: The X-ray Afterglow of AXP 1E 2259+586's 2002 Outburst

The content of this Chapter originally appeared as: Zhu, Weiwei; Kaspi, Victoria M.; Dib, Rim; Woods, Peter M.; Gavriil, Fotis P.; Archibald, Anne M. *The Long-term Radiative Evolution of Anomalous X-ray Pulsar 1E 2259+586 After its 2002 Outburst* ApJ, Volume 686, Issue 1, Page 520-527 (2008).

In this Chapter, we report the analysis of five *XMM* observations of the AXP 1E 2259+586 taken in 2004 and 2005 during its relaxation following its 2002 outburst, and compare the results with those of five previous *XMM* observations taken in 2002 and 2003. We find that the observed flux decay was well described by a power law of index -0.69 ± 0.03, similar to what was found from the X-ray afterglow of some SGRs, and that, as of 2005, the pulsar was still hotter and brighter than pre-outburst. We also find a strong correlation between the spectral hardness and flux of the pulsar. We also studied the pulsed profile evolution of the pulsar but did not find very significant changes.

The contributions of the co-authors are as follows: Prof. Kaspi was the primary investigator of the *XMM* proposal. Dr. Woods, P. and Dr. Gavriil, F. were co-investigators on the proposal. Dr. Dib, R. extracted this pulsar's pulsed flux from *RXTE* data taken between 2001 and 2006, to be compared with the phase-average flux measured using *XMM*. Dr. Dib, R. also extracted a timing ephemeris based on the *RXTE* data. I used this ephemeris to fold the *XMM* data for the pulsed profile analysis. Archibald, A. M. provided the computer code for the estimation of the area pulsed fraction (see Chapter 3 for details). I performed the spectral and pulse profile analysis for the five new *XMM* data sets and five previously published (taken in 2002 and 2003; Woods et al. 2004) archival data sets, using new data reduction tools and calibration files.

Chapter 4: Searching for X-ray Variability in the Glitching AXP 1E 1841−045

The content of this Chapter originally appeared as: Zhu, Weiwei; Kaspi, Victoria, M. *Searching for X-ray Variability in the Glitching Anomalous X-ray Pulsar 1E 1841−045 in Kes 73* ApJ, Volume 719, Issue 1,Page 351-356 (2010).

In this Chapter we report the spectral analysis of archival X-ray data from the AXP 1E 1841−045, obtained between 1993 and 2007 by using *ASCA* , *Chandra* , *XMM* and *Suzaku* observatories. This pulsar has exhibited three glitches between 1999 and 2006, as determined by *RXTE* observations. We find no evidence of significant flux variability associated with the glitches based on the focusing X-ray observations.

In this Chapter we quote *RXTE* measured pulsed fluxes of this pulsar (in Figure 4.2) in order to compare with the phase-averaged fluxes measured in our analysis. These *RXTE* measurements had been published in Dib et al. (2008b). I performed the spectral data analysis for the *ASCA* , *Chandra* , *XMM* and *Suzaku* data.

Chapter 5: X-ray Detection of High-B PSR B1916+14

The content of this Chapter originally appeared as: Zhu, Weiwei; Kaspi, Victoria, M.; Gonzalez, Marjorie E.; Lyne, Andrew G. *XMM-Newton X-ray Detection of the High-Magnetic-Field Radio Pulsar PSR B1916+14* ApJ, Volume 704, Issue 2, Page 1321-1326 (2009).

In this Chapter we present the first X-ray detection of the high-magnetic-field radio pulsar B1916+14.

The contributions of the co-authors are as follows: Prof. Kaspi, V. M. was the primary investigator of the *XMM* proposal. Dr. Gonzalez, M. E. helped writing the proposal. Prof. Lyne, A. G. provided the timing ephemeris for us to search for the pulsar's pulsations. I performed the imaging, spectral analysis and pulsation analysis of the *XMM* data.

Chapter 6: Chandra Observations of High-B RPP J1718−3718

The content of this Chapter has been accepted for publication by ApJ and will be published soon. The accepted manuscript has the following author list and title: Zhu, Weiwei; Kaspi, Victoria, M.; McLaughlin, Maura. A.; Pavlov, George. G.; Ng, Chi Y.; Manchester, Richard N.; Gaensler, Bryan. M.; Woods, Peter. M. *Chandra Observations of the High-Magnetic-Field Radio Pulsar J1718−3718.*

In this Chapter we present the analysis of four new *Chandra* observations of the high-magnetic-field radio pulsar J1718−3718 taken in 2009 as well as the reanalysis of a previously published *Chandra* observation taken in 2002. We detected, for the first time, X-ray pulsations from the pulsar, and constrained the spectral parameters of the pulsar based on a combined spectrum from all five observations. We find that the pulsar's blackbody temperature is somewhat higher than that of the other rotation-powered pulsars of the same age, and that the pulsar's bolometric luminosity is only a fraction of ∼0.3 of its spin-down power, assuming a distance of 4.5 kpc. We compiled the blackbody temperature measurements for a list of high-B and low-B rotation-powered pulsars, and find a hint that those of higher B are generally hotter than the low-B pulsars of the same age. However, deeper observatories of these pulsars are needed to confirm this.

The contributions of the co-authors are as follows: Prof. Kaspi V. M., Prof. McLaughlin, M. A., Prof. Pavlov, G. G. and Dr. Woods, P. M. wrote the proposal for the 2009 *Chandra* observations, and also provided comments and suggestions for the writing of the manuscript. Dr. Ng, C.-Y. and Prof. Gaensler, B. M. performed radio interferometer observations of the pulsar and obtained a precise radio position in order to compare with the pulsar's *Chandra* position. Prof. Manchester, R. N. provided the radio timing ephemeris for detecting pulsations in the X-ray data of the pulsar. I performed the imaging, spectral analysis and the searching of pulsation in the *Chandra* data. I compiled the table of measured parameters of high-B and low-B pulsars.

1

Introduction

1.1 Pulsars

The idea of the neutron star was first proposed by Baade & Zwicky (1934). They suggested that it is possible for a massive star to collapse into a highly compact star consisting mostly of degenerate neutrons during its supernova explosion. Landau (1938) estimated that such a neutron star could, at most, have a mass of $\sim 1.5\mathrm{M}_\odot$ and a radius of $\sim 3\,\mathrm{km}$, based on the same idea as the Chandrasekhar mass limit of a white dwarf. This limit shows how compact the neutron stars can be. Later, more realistic calculations showed that a typical neutron star's mass and radius should be about $1.4\mathrm{M}_\odot$ and $10\,\mathrm{km}$. However, such an object was not observed until the first extrasolar X-ray object, Scorpius X-1, was discovered by Aerobee rocket in 1962 (Giaconni et al., 1962). This object was identified as an accreting neutron star by Shklovsky (1967). Also in 1967, radio pulsars were discovered by Hewish et al. (1968). The famous Crab pulsar and Vela pulsar were among the first few radio pulsars discovered, and both were found to be associated with Supernova Remnants (SNRs; Large et al. 1968; Staelin & Reifenstein 1968; Richards & Comella 1969; Cocke et al. 1969). The very short spin period of radio pulsars (33 ms in the case of the Crab pulsar) indicates that pulsars are very compact objects, most likely more compact than the white dwarfs. It was then argued that neutron stars were the only reasonable explanation for the radio pulsars. Gold (1968) pointed out that a highly magnetized ($B \sim 10^{12}\,\mathrm{G}$) fast rotating neutron star could account for the observed features of pulsars, such as the short, stable and slowly increasing period of milliseconds or seconds. More specifically, pulsars are losing their spin energy through magnetic dipole radiation (Pacini, 1967, 1968; Ostriker & Gunn, 1969). This general idea is now well accepted, though a more realistic model must include pulsar's radiation mechanism.

Pulsar spin parameters P and $\dot{P}$ are their most informative observables (see Figure 1.1 for the distribution of P and $\dot{P}$ for pulsars in the Australia Telescope National Facility (ATNF) pulsar catalog[1]). The periods of most pulsars lie from millisecond to seconds. $\dot{P}$ varies from $\sim 10^{-21}\,\mathrm{s\,s^{-1}}$ to $\sim 10^{-11}\,\mathrm{s\,s^{-1}}$. One can estimate the pulsar's age τ based on the magnetic dipole model, $\tau \simeq P/(2\dot{P})$; this is also known as the characteristic age of the pulsar. The characteristic age of the Crab pulsar is 1.2 kyr, and is close to the actual age of 957 yr according to historical records of its birth supernova event. Most of the early discovered pulsars have characteristic ages smaller than $\sim 10^{7}$ yr. However, this characteristic age of pulsar is estimated based on the assumption that the pulsar was born spinning a lot faster than its current spin rate. This might not always be a good assumption, especially for the young pulsars.

From the spin characteristics of a pulsar, one can infer the loss rate of its rotational energy $\dot{E} \equiv 4\pi^2 I\dot{P}/P^3$ (also called spin-down power), where I is the neutron star's moment of inertia. Assuming $I \simeq 10^{45}\,\mathrm{g\,cm^2}$, which is calculated for a neutron star with nominal mass and radius, one finds that the rotation energy loss rate of observed pulsars varies from 10^{30} to $10^{38}\,\mathrm{erg\,s^{-1}}$. For instance, the Crab pulsar has $\dot{E}$ of $4.6 \times 10^{38}\,\mathrm{erg\,s^{-1}}$, the same order of magnitude as the power needed to power the Crab nebula.

One can also infer the pulsar's surface (equatorial) magnetic field strength from its spin parameters, $B \equiv 3.2 \times 10^{19}(P\dot{P})^{1/2}\,\mathrm{G}$. Most radio pulsars have magnetic fields of $\sim 10^{12}$ G. This is based on the assumption that the pulsar loses all of its rotational energy to magnetic dipole radiation.

For some pulsars, $\dot{P}$ is so high that it is possible to measure the second period derivative, $\ddot{P}$. Based on $\ddot{P}$, one can derive a diagnostic parameter, the braking index, defined as $n \equiv \Omega\ddot{\Omega}/\dot{\Omega}^2$, where Ω is the spin angular velocity. The magnetic dipole

---

[1] http://www.atnf.csiro.au/people/pulsar/psrcat/

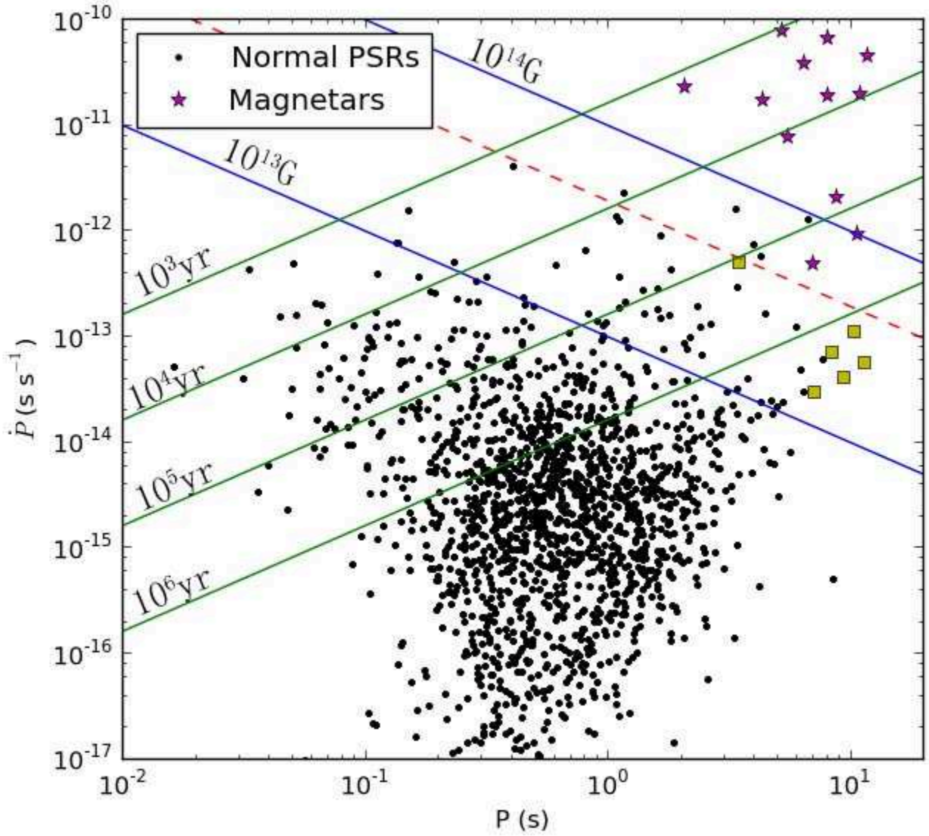

Figure 1.1 The P-$\dot{P}$ diagram of pulsars in the ATNF catalog[1].

model predicts a braking index of $n = 3$ for all pulsars, while n has only been measured for 6 pulsars and lies between 1.0 and 2.91 (Lyne et al. 1993, 1996; Weltevrede et al. 2011; Livingstone et al. 2005a,b, 2010 and Espinoza et al. 2011a). This means that a simple magnetic dipole model is not sufficient to explain the spin-down of all pulsars.

Interestingly, not all pulsars spin down steadily. A few of them, such as the Vela, pulsar exhibit a peculiar phenomenon called a pulsar glitch. A glitch is a sudden spin up of the pulsar. During such an event, the pulsar's spin rate increases by a small fraction ($\Delta\nu/\nu \sim 10^{-9}$–$10^{-6}$). The first pulsar glitch was observed in the Vela pulsar (Radhakrishnan & Manchester, 1969). Today there are over 300 glitches observed (Espinoza et al., 2011b), mostly in radio pulsars, and some in magnetars.

Soon after radio pulsars were discovered, Schreier et al. (1972) and Tananbaum et al. (1972) discovered pulsating X-ray sources, X-ray pulsars Cen X-1 and Her X-1, and found evidence that they are in close binary systems. Today there are many neutron stars found in binaries. Some of them are accreting from their companion star and therefore very luminous in X-rays. Some neutron stars went through so much accretion that they were spun up by the accreted materials and became "recycled" millisecond pulsars. After the material for accretion is depleted, these millisecond pulsars may start to emit in the radio band again, but their magnetic fields would have been significantly weakened, with only $\sim 10^8\,$G left (for more information see Kippenhahn & Weigert 1967; Paczyński 1971 and Ghosh 2007).

1.1.1 Neutron Stars Inside and Out

Like all stars, the internal structure (Figure 1.2) of a neutron star is determined by the Equation of State (EOS) of matter and hydro-static balance. The details of neutron star internal structure and mass radius may vary a lot with different assumed equation of states. Here we briefly introduce one possible neutron star solution. On the surface of a neutron star, there is a thin atmosphere of centimetres thickness made mostly of hydrogen and helium of density $< 100\,\mathrm{g\ cm^{-3}}$. Below the atmosphere lies the outer crust of the neutron star. It is composed of ionized atoms; their atomic number gets higher as we go deeper, until they become the highest-number stable nuclear $^{56}_{26}$Fe. About a kilometre into the surface, at the bottom of the outer crust, the matter density reaches 4×10^{11} g cm^{-3}. This density is called the neutron drip line, because at this density the electrons are highly degenerate, and all of their low energy states are occupied, making it very hard for neutrons to decay. As a result, atomic nuclei start to become neutron rich and some neutrons may "drip" out the nuclei and become free neutrons. Deeper into the star is the inner crust, where matter gets even denser and eventually reaches nuclear density, 2×10^{14} g cm^{-3}, at the bottom of the inner crust about several kilometres into the star. Here the neutron-dominated nuclei are crushed by the pressure and dissolve into a free neutron gas. The inner and outer crust of the neutron star are called 'crusts' because they are likely in the solid state, with the presence of some neutron superfluid. This is because atomic nuclei still exist in these layers, and their Coulomb interactions should be strong enough to form solid state lattices. Below the neutron star crust is the neutron star core. It is dominated by a Fermi-degenerate, non-relativistic neutron gas. The density of the neutron gas reaches $\sim 10^{15}$ g cm^{-3} at the centre of the neutron star, about 10–15 km deep. Exactly what happens to the matter of that density is not clear. Some suggest that the neutrons themselves might dissolve into quarks, and some species of quarks, such as strange quarks, might emerge in order to minimize the free energy. See Pines (1980); Shapiro & Teukolsky (1983); Lattimer & Prakash (2001) for more detailed discussions on neutron star structure.

The higher the total mass of the neutron star, the denser its core becomes; exceeding a certain mass limit ($\sim 2 - 3\mathrm{M}_\odot$), the neutron star's core density will be so high that the degenerate neutron gas becomes relativistic. However, the EOS of a relativistic degenerate Fermi gas is too soft, i.e. pressure increases too slowly as density increases, to support the gravity of the star. Consequently, the neutron star would collapse into a black hole.

The compactness and stable rotation of neutron stars makes them great test grounds for physics of matter at nuclear density. Baym et al. (1969) suggested that the free neutrons in the inner crust could form particle pairs and transition to a su-

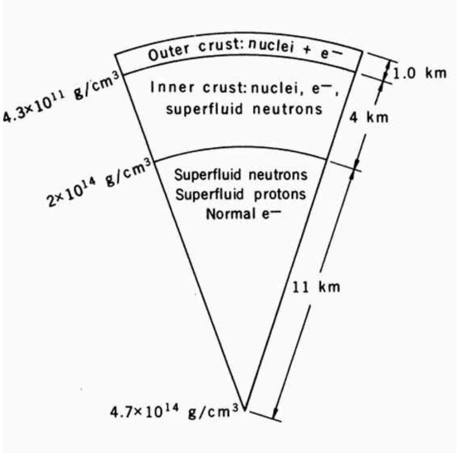

Figure 1.2 The cross section of a neutron star. Figure adapted from Pines (1980).

perfluid state, and having a superfluid inner crust may help explain some pulsar's glitch phenomenon (Radhakrishnan & Manchester 1969; see Section 1.1). Their idea is that there could be two weakly coupled rotational components in a neutron star: one is the charged outer crust to which the outside magnetic fields are anchored, and the other is the superfluid inner crust. The rotation of the superfluid is harder to decelerate than the crust due to the microscopic rotational vortices formed in them. As a result the outer crust would always rotate at a slower rate than the superfluid inner crust. At some point if some mechanism could trigger a sudden increase in the interactions between the superfluid and the outer crust, then one would observe a sudden spin up of the pulsar as the crust catches up with the superfluid. More detailed triggering mechanisms as well as different models for pulsar glitches were also proposed later (see Alpar et al. 1981; Manchester & Taylor 1977 and references there in). There is another glitch model that is worth mentioning: the starquake model (Ruderman, 1969). The starquake model may apply to the glitches of the fast spinning pulsars, or glitches of the slow pulsars with very small fractional changes in the period ($< 10^{-8}$). Due to their fast rotation, some pulsars may be oblate, and the oblateness increases their rotational moment of inertia by a small faction. As the pulsar spins down, the rotation-induced oblateness also decreases. However, the solidified neutron star crust would resist any deformation and as a result, the star will always be a little more oblate than its equilibrium shape. As the equilibrium shape of the star shrinks over time, the crust would become more and more stressed and at some point it would yield. In such an event, the oblateness and the moment of inertia of the star would suddenly drop to the equilibrium values. Consequently, the star would suddenly spin up to conserve the angular momentum. This model can explain some fast-spinning pulsars' glitches, however, it does not work on the slowly rotating neutron stars including the magnetars, simply because they are too slow to have enough rotational oblateness to account for the observed glitches.

In the early years of neutron star study, the immediate surrounding of a neutron star was assumed to be a vacuum (Hoyle et al., 1964; Pacini, 1967). However, Goldreich & Julian (1969) pointed out that the rotating magnetic fields of the neutron star will induce electric fields that are strong enough to pull charged particles from its atmosphere. As a result, the neutron star's magnetosphere must be filled with charge separated plasma of charge density $\rho_{GJ} = -\mathbf{\Omega} \bullet \mathbf{B}/(\mathbf{1} - (\mathbf{\Omega r} \sin\theta/\mathbf{c})^{\mathbf{2}})/(\mathbf{2}\pi\mathbf{c})$ in order to maintain electro-static balance, where $\mathbf{\Omega}$ is the local spin vector and $\mathbf{B}$ is the local magnetic field. However, the extent of such a co-rotating plasma magnetosphere cannot be infinite; it is limited by one of two physical boundaries. One boundary is the light cylinder. It is defined as the cylinder so distant from rotational axis that the magnetosphere has to move at the speed of light in order to co-rotate with the pulsar (the radius of light cylinder is $d_{\mathrm{lc}} \equiv \frac{c}{\Omega}$). That's why instead of co-rotating with the pulsar, the magnetosphere plasma and magnetic field lines would wind up at light cylinder, and travel beyond that point in the form of particle wind and electro-magnetic waves (Goldreich & Julian, 1969). The other boundary is the magnetosphere radius. It is defined as where the magnetic field pressure is balanced by the ram pressure from the surrounding matter. The latter condition is more likely to be applicable when the pulsar is in an accreting binary. The ram pressure from the accreted matter could significantly limit the extent of the pulsar's magnetosphere.

The pulsar's magnetosphere has a boundary. Therefore, depending on the extent of the field lines, the magnetosphere is divided into two parts (see Figure 1.3). In the

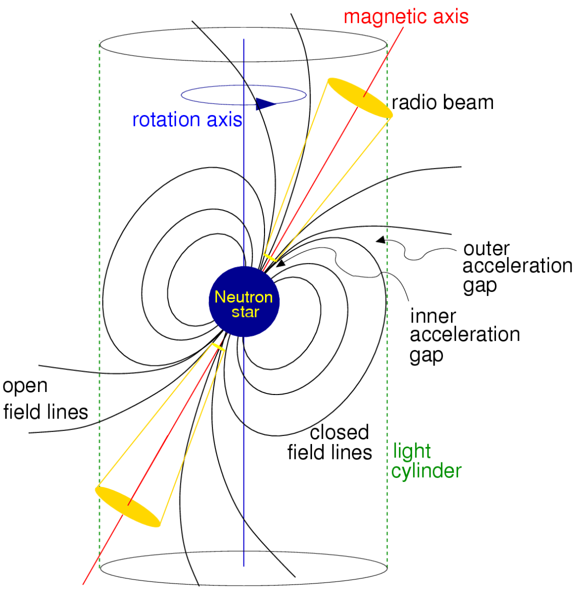

Figure 1.3 Pulsar's magnetosphere. Figure adapted from `http://www.cv.nrao.edu/course/astr534/Pulsars.html`.

open field line region, charged particles are free to move along the field lines and may be able to leave the pulsar magnetosphere. In the closed field line region, particles are trapped by the magnetic field and are dragged by the field to co-rotate with the star. As a result, it is possible to form a constant flow of current in the open field region, but hard to do so in the closed field line region.

Over the past four decades, the pulsar radiation mechanism has been a very active field of research. A general picture was proposed by Ruderman & Sutherland (1975) in which pulsar radiation is caused by a strong current formed in the open-field-line region as particles are continuously pulled off the surface of the star to replenish those lost to the particle wind outside light cylinder. In this scenario, the charged particles were accelerated to relativistic speed in a small "gap"-like region located just above the stellar surface and where the magnetic pole is (the polar cap). As relativistic particles move along the strong magnetic field lines, they emit radiation at radio, X-ray and sometimes even gamma-ray wavelengths. The resulting radiation is highly beamed in the direction of the magnetic field, and polarized along the projected direction of the magnetic field. This explains the narrow pulse shapes and the phase-dependent changes in polarization observed from some pulsars. Various other models, e.g. the slot gap model (Sturrock, 1971; Arons, 1983; Muslimov & Harding, 2004) and outer gap model (Holloway, 1973; Cheng et al., 1986a,b), were proposed based on similar general pictures but differ in their assumed particle accelerating regions or the exact radiation mechanism. Despite the in-depth theoretical work and massive amount of radio observational data, we still haven't completely understood the pulsar radiation mechanism. This is likely due to the difficulty in modeling plasma dynamics and the diversities in pulsar phenomena.

An interesting side effect of the pulsar's radiation is return current heating. The strong current along the open field lines induced by the rotation of the pulsar would also drive particles to collide onto the pulsar and heat up a small polar cap region of the stellar surface. This has been observed from many RPPs (De Luca et al., 2005; Manzali et al., 2007; Misanovic et al., 2008). Some RPPs with high spin-down power were observed to have not only a strong power-law X-ray spectrum (most likely the non-thermal magnetospheric emission) but also some thermal X-ray emission. Such emission usually shows a rather small blackbody radius ($\sim$ 10–100 m), consistent with the size of the polar cap. Being powered by the spin down of pulsar, the return current heating should convert only a part of the pulsar's $\dot{E}$ to thermal emission. Observations of the RPPs and theoretical modeling both show consistently that only $\lesssim 10^{-3}\dot{E}$ are converted to X-rays (De Luca et al., 2005; Harding & Muslimov, 2001, 2002).

1.1.2 Manifestations of Neutron Stars

Over the past few decades, our knowledge about the neutron star family has increased significantly. Previously, only one kind of isolated neutron star was known, the radio pulsars. Powered by their rotational energy, they are also called rotation-powered pulsars (RPPs). Their luminosities are generally much lower than their $\dot{E}$. X-ray observations have led to the discovery of several new classes of isolated neutron stars;

these include magnetars and X-ray Isolated Neutron Stars (XINSs)[1]; see Kaspi (2010) for a recent review. They all exhibit distinctive properties different from those of conventional RPPs.

Magnetars are isolated, slowly rotating (known periods in the range of 2–12 s) X-ray pulsars, having thermal and non-thermal X-ray luminosities that are in many cases much higher than their spin-down luminosities. Some are characterized by repeating X-ray/γ-ray bursting activity and therefore are called Soft Gamma Repeaters (SGRs). Others are less active and are characterised by their persistent X-ray pulsations; these are classified as Anomalous X-ray Pulsars (AXPs). However, the distinction between these two classes has been increasingly blurred, as some sources show properties of both (e.g. Gavriil et al. 2002; Kaspi et al. 2003; Woods et al. 2004; Rea et al. 2009b; Kaneko et al. 2010; Israel et al. 2010; Ng et al. 2011). They generally have very high magnetic fields ($B \sim 10^{14}$–10^{15} G), inferred assuming that their spin-down rates are solely a result of magnetic dipole radiation. It is generally believed that their X-ray luminosities are powered by the decay of the ultra-high magnetic fields (Duncan & Thompson, 1992; Thompson & Duncan, 1995; Thompson & Duncan, 1996; Thompson et al., 2002). For reviews of magnetars, see Woods & Thompson (2006); Kaspi (2007) or Mereghetti (2008a).

XINSs are a small group of slowly rotating (known periods in the range of 3–11 s), nearby (distance $\leq$ 500 pc) neutron stars (see Kaspi et al. 2006, Haberl 2007 and Turolla 2009 for reviews). Emitting apparently thermal X-ray spectra, they show no hard X-ray emission ($>$ 2 keV). No radio counterparts have been found for these neutron stars. Given their long periods and expected small beaming fractions, it is possible that their radio beams are misaligned with our line of sight (Kondratiev et al., 2009). Therefore, it is not clear whether or not they are intrinsically radio quiet. Timing observations of XINSs have revealed relatively high inferred magnetic fields ($\sim$1–3$\times10^{13}$ G), and characteristic ages of the order of 10^6 years (Kaplan & van Kerkwijk, 2005; Zane et al., 2005; van Kerkwijk & Kaplan, 2008; Kaplan & van

---

[1] Also known as X-ray dim isolated neutron stars (XDINSs).

Kerkwijk, 2009a) for some of them. Unlike magnetars, they show no bursting activity and are much less luminous. However, their X-ray luminosities are comparable with their spin-down power and significantly higher than those of normal RPPs of similar ages (Kaplan & van Kerkwijk, 2009a). Therefore, Kaplan & van Kerkwijk (2009a) suggest that the cooling of XINSs is likely affected by magnetic field decay heating as predicted in theory by Arras et al. (2004), Pons et al. (2007) and Aguilera et al. (2008). An alternative explanation is that the XINSs are surrounded by fall-back disks and are heated due to accretion (Alpar, 2007).

One likely crucial group of pulsars for understanding the relationships between RPPs, magnetars and XINSs are the high-magnetic-field RPPs. There are now several known RPPs that have spin-down magnetic fields close to or higher than those of magnetars (Ng & Kaspi, 2010). Some of them are radio pulsars. Sharing properties with both classes, these high-B pulsars could be transition objects between RPPs and magnetars. Indeed, some magnetars are now known to emit at radio wavelengths, and magnetar-like bursting behavior has been seen in one high-B pulsar (Livingstone et al., 2010). XTE J1810−197 is a transient AXP, first detected in outburst (Ibrahim et al., 2004). This magnetar, originally not emitting in the radio band, was observed to have radio pulsations one year after its X-ray outburst (Camilo et al., 2006). Also, the magnetar 1E 1547.0−5408 shows radio pulsations (Camilo et al., 2007a). Though not a radio pulsar, the high-B rotation-powered ($B = 4.9 \times 10^{13}\,\mathrm{G}$) X-ray PSR J1846−0258 exhibited a sudden, magnetar-like X-ray outburst that lasted for a few weeks in 2006 (Gavriil et al., 2008; Kumar & Safi-Harb, 2008; Ng et al., 2008). Thus, it is possible that the high-B RPPs are magnetars in quiescence. Recently, a new magnetar, PSR J1622−4950, was discovered via its active radio emission, yet is relatively X-ray-faint (Levin et al., 2010). Another magnetar, SGR 0418+5729, detected via its bursting activities, was found to have magnetic field $B < 8 \times 10^{12}\,\mathrm{G}$, well below that of the other magnetars, suggesting that a strong dipole magnetic field might not be necessary for magnetar-like behavior (van der Horst et al., 2010; Rea et al., 2010; Esposito et al., 2010). These discoveries further suggest that there could be a large, unseen population of quiescent magnetars, some of which may be 'disguised' as radio pulsars.

1.2 Magnetars

1.2.1 Introduction

The idea of the magnetar was first introduced by Duncan & Thompson (1992) to explain the intriguing phenomenon first observed in late 1970s, the soft gamma repeater. On Jan 7 1979, a soft gamma-ray burst was detected from the constellation of Sagittarius (Mazets & Golenetskii, 1981). It was initially classified as a classical gamma-ray burst. However, an intense reactivation in 1983 clearly distinguished this gamma-ray burst from the classical gamma-ray bursts (Laros et al., 1987). As a result, the object from which the bursts were detected was named soft gamma repeater (SGR) 1806−20. Another soft gamma-ray burst, and one of the most energetic ones, Gamma-ray Burst (GRB) 790305 (the source of this GRB was later named SGR 0526−66) was detected on March 5 1979 (Mazets et al., 1979), soon after the Jan 7 burst of SGR 1806−20. This March 5th burst was composed of a bright spike and a 3-minute long tail with 8 s periodic modulation. Its position coincides with the N49 supernova remnant in the Large Magellanic Cloud (LMC). Inspired by these facts, Duncan & Thompson (1992) argued that SGR 0526−66 might be a neutron star with a very strong magnetic field. The magnetic field of SGR 0526−66 had to be $\sim 5 \times 10^{14} (P/8\ \mathrm{s}) (t_{\mathrm{SNR}}/10^4\ \mathrm{yr})^{-1/2}\,\mathrm{G}$ to spin it down to the current period in the estimated age of SNR N49 ($\sim$ 0.6–1.6 $\times\ 10^4$ yr; Vancura et al. 1992). No prior observed radio pulsar's magnetic field was nearly as high as 10^{14} G. Duncan & Thompson (1992) argued that such a high magnetic field could form in a dynamo process inside a very rapidly spinning newborn neutron star. After the initial 30 s, neutron stars left with a 10^{14}–10^{15} G B field would quickly spin down to $\sim$10 s in period within $\sim 10^4$ yr, which would make them very inefficient in emitting radio pulsations. Therefore, they may not easily be detectable as radio pulsars. Duncan & Thompson (1992) named these highly magnetized neutron stars "magnetars," and suggested that SGRs 1806−20 and 0526−66 could be the first observed examples of magnetars.

More evidence supporting this magnetar idea was found later. Paczyński (1992) pointed out that the super-Eddington peak luminosity ($\sim 2 \times 10^{42}\mathrm{erg\,s^{-1}} \approx 10^4 \mathrm{L_{Edd}}$) observed from the March 5 burst of SGR 0526−66 could be explained if it is a magnetar of $B \sim 8 \times 10^{14}$ G. This is because the ultra high magnetic field can significantly reduce the Thomson and Compton cross sections for photon energies much smaller than the cyclotron energy, thereby increasing the critical luminosity. Furthermore, the total magnetic energy of such a magnetar is approximately:

$$E_B \approx \frac{B^2}{8\pi}\frac{4\pi}{3}R^3 \approx 4 \times 10^{46}\mathrm{erg}\left(\frac{B}{5 \times 10^{14}\mathrm{G}}\right)^2 \left(\frac{R}{10\ \mathrm{km}}\right)^3, \tag{1.1}$$

which is more than enough to power the March 5 burst of 10^{44} erg total energy. A few years later, X-ray pulsations were found from SGR 1806−20 by Kouveliotou et al. (1998) while it is in quiescence. A spin-down magnetic field of 8×10^{14} G and a spin-down age of 1500 yr were measured. They are clearly consistent with the predictions of the magnetar model.

As of 2011, there are seven confirmed SGRs and two candidates[1]. The confirmed SGRs are 1806−20 (Mazets & Golenetskii, 1981), 0526−66 (Mazets et al., 1979), 1900+14 (Hurley et al., 1999), 1627−41 (Woods et al., 1999), 0501+4516 (Enoto et al., 2009), 0418+5729 (Esposito et al., 2010) and 1833−0832 (Göğüş et al., 2010); the two candidates are 1801−23 (Cline et al., 2000) and 2013+34 (The Gamma-ray bursts Coordinates Network, number 4037[2]). They were all discovered through the observation of their gamma-ray bursts. Most SGR bursts can be described as super-Eddington bursts that last for less than a second with a thermal-like spectrum; however some SGRs exhibit major gamma-ray bursts with peak luminosity 10^4 times the Eddington limit, lasting for dozens of seconds. The X-ray afterglows of these events decay over the time scale of weeks to a few years (Woods & Thompson, 2006). We call these major bursts outbursts or giant flares. Outbursts have been observed

---

[1] http://www.physics.mcgill.ca/∼pulsar/magnetar/main.html

[2] gcn.gsfc.nasa.gov/gcn3/4037.gcn3

from SGR 0526−66 on March 5, 1979 (Mazets et al., 1979), SGR 1900+14 on August 27, 1998 (Hurley et al., 1999), SGR 1627−41 in June 1998 (Mazets et al., 1999; Woods et al., 1999) and SGR 1806−20 on December 27, 2004 (Hurley et al., 2005). Smaller bursts were also observed during the outburst epochs of these SGRs. There are also several SGR bursts that lie between the giant flares and the typical short bursts in terms of energy and duration; they are called "intermediate bursts". See Woods & Thompson (2006) for a review of SGRs.

A second manifestation of magnetars is the Anomalous X-ray Pulsars (AXPs). AXPs are isolated neutron stars discovered with persistent X-ray luminosities of $L_X \gtrsim 10^{34}\,\mathrm{erg\ s^{-1}}$, and L_X higher than their rotational energy loss rate $\dot{E}$. Some AXPs are now found to be transient objects, their X-ray luminosities can vary by orders of magnitudes. Their persistent X-ray spectra are usually composed of a blackbody-like thermal component of temperature $kT \sim 0.4\,\mathrm{keV}$ and a power-law-like non-thermal tail of index $\Gamma \sim$2–3. Their anomalously high L_X and isolated nature distinguishes them from the majority of neutron stars – the rotation-powered pulsars and accretion-powered neutron stars. The first observed AXP was 1E 2259+586 (Gregory & Fahlman, 1980). It was originally interpreted as an X-ray binary. However, it was later found spinning down steadily without any evidence of an orbital period. It also has spin-down power of $\sim 6 \times 10^{31}\mathrm{erg\ s^{-1}}$, much lower than its X-ray luminosity (Koyama et al., 1987), which is unexpected for a rotation-powered X-ray pulsar. In the following decades, several other AXPs like 1E 2259+586 were discovered, e.g. 1E 1048.1−5937 and 4U 0142+61. These AXPs have a small scale height above the Galactic plane and some of them are associated with SNRs, therefore they were argued to be probably too young to be low mass X-ray binaries (van Paradijs et al., 1995). Duncan & Thompson (1996) pointed out that the AXPs are similar to the SGRs in terms of their period, inferred magnetic fields and association with young SNRs (Figure 1.1); therefore they could also be magnetars. They suggested that their X-ray luminosity could be powered by the decay of magnetar's magnetic field.

An alternative explanation is that these AXPs are neutron stars accreting from a fossil disk made of matter which fell back from the birth supernova explosion (Corbet et al., 1995; van Paradijs et al., 1995; Chatterjee et al., 2000; Chatterjee & Hernquist, 2000; Alpar, 2007). The fall-back disk model predicts that the AXPs should have bright optical counterparts. Only a dim counterpart was observed from the first optically detected AXP, 4U 0142+61 (Hulleman et al., 2000). One piece of evidence that strongly favours the magnetar model is the detection of spin pulsations from the optical counterpart of 4U 0142+61. This AXP is found to be pulsing in the optical band with a large pulsed fraction (Kern & Martin, 2002), and no disk can reproduce such a significant optical pulsation. However, it has been argued that the putative disk may only be bright in the infrared and infrared pulsations have yet to be observed.

The likely magnetar nature of the AXPs was further confirmed when some of the AXPs showed SGR-like behavior. AXP 1E 1048.1−5937 was observed to emit SGR-like bursts in 2001 (Gavriil et al., 2002). 1E 2259+586 was seen to undergo a major SGR-like outburst in 2002 (Kaspi et al., 2003; Woods et al., 2004). During its outburst epoch, over 80 short SGR-like bursts and a near-infrared enhancement were observed (Gavriil et al., 2004; Kaspi et al., 2003). Subsequently, a variety of different types of activity in AXPs have been seen, including short- and long-term flux variations (Gavriil & Kaspi, 2004; Dib et al., 2007) and slow and rapid pulse profile changes (Iwasawa et al., 1992; Kaspi et al., 2003; Woods et al., 2004; Israel et al., 2007; Dib et al., 2007; Dib et al., 2008c), in addition to bursts and outbursts (Gavriil et al., 2006; Woods et al., 2005; Dib et al., 2007; see Kaspi 2007 for a recent review). Some other AXPs (XTE J1810−197, CXOU J164710.2−455216) have also exhibited transient behaviours that resemble the SGR outbursts but are less energetic (see Section 1.2.2 for details).

By the time this thesis was written, there were 12 observed AXPs including 9 confirmed and 3 candidates. The confirmed AXPs are 1E 1547.0−5408 (Camilo et al., 2007a), XTE J1810−197 (Ibrahim et al., 2004), 1E 1048.1−5937 (Kaspi et al., 2001), 1E 2259+586 (Fahlman & Gregory, 1981; Gavriil & Kaspi, 2002), CXOU

J010043.1−721134 (Juett et al., 2002; McGarry et al., 2005), 4U 0142+61 (Gavriil & Kaspi, 2002), CXO J164710.2−455216 (Israel et al., 2007), J170849.0−400910 (Gavriil & Kaspi, 2002) and 1E 1841−045 (Vasisht & Gotthelf, 1997). The candidates are AX J1845−0258 (Torii et al., 1998), J1622−4950 (Levin et al., 2010) and CXOU J171405.7−381031 (Sato et al., 2010). For an up-to-date source list, see the magnetar catalog.

In recent years, much progress has been made in the observation of magnetars. These include multi-wavelength observations, X-ray/timing monitoring programs (Dib et al., 2008b,a; Dib, 2009), and detection of spectral features. The details of all this progress is out of the scope of this thesis. Please see Kaspi (2007, 2010); Mereghetti (2008b); Rea & Esposito (2011) for extensive reviews.

1.2.2 The Magnetar Model

In the conventional theory of the origin of neutron star magnetism, the $\sim 10^{12}\,$G magnetic field commonly observed in radio pulsars is the result of magnetic flux conservation during the core collapse event. Thompson & Duncan (1993) proposed a new mechanism for the origin of neutron star magnetism. They suggest that neutron star magnetic fields are formed through a dynamo process inside the newborn neutron star. Furthermore, they suggest that there could be two different kinds of dynamo processes: one for pulsars born with spin period $P > 30\,$ms, and one for those born faster. The slow neutron stars get magnetic fields of 10^{12}–$10^{13}\,$G through a convection-driven dynamo process and become normal radio pulsars; the fast ones get 10^{14}–$10^{15}\,$G B fields through both differential-rotation-driven and convection-driven dynamo processes and become magnetars.

Thompson & Duncan (1996) suggested that the ultra-strong magnetic field inside magnetars are not purely dipolar. In fact, there must be a strong toroidal B field inside the star for the system to be stable. But this strong toroidal field will slowly decay and diffuse though neutron star core. This might lead to significant heating in the neutron star core due to the ambipolar diffusion process. Part of the heat generated this way will be dissipated though neutrino emission, however, the rest will be conducted to the neutron star surface and give rise to a persistent surface emission of about 10^{34}–$10^{36}\,\mathrm{erg\,s^{-1}}$. Therefore, this mechanism could explain the persistent X-ray emission observed from most SGRs and AXPs.

It is also suggested by Thompson & Duncan (1995) that the rigid crust of the neutron star may resist the diffusion of magnetic fields. But as magnetic stress builds up, the crust will eventually yield, crack, and result in sporadic magnetic-field interchange/reconnection outside the neutron star. Due to the huge amount of energy the strong magnetic fields contain, if the crust fracture is of small scale, then the resulting small scale magnetic field reconnection will perhaps lead to a sudden burst of pair plasma that radiates away quickly. This mechanism could explain the spectrum, timescale and energy of the smaller SGR bursts. On the other hand, if the crust fails on a large scale, the entire magnetosphere of the neutron star could be filled with a plasma fireball. This fireball could have energy up to $\sim 10^{44}$–10^{45} erg, enough to power the giant flares of SGRs such as the 1979 March 5th event of SGR 0526$-$66. The fireball plasma in the open field line region should immediately expand to infinity, while that in the closed field line region gets trapped and slowly shrink as photons escape. Interestingly, the March 5 event consisted of a 0.15 s-duration initial spike and a ~200 s tail, and the total energy contained in the initial spike was only a factor of 5 smaller than that in the tail. Therefore, this short initial spike could be caused by the fast expanding fireball in the open fields, and the tail could be caused by the trapped fireball.

Thompson & Duncan (1996) predicted that the fractures of the neutron star crust could lead to a sizable spin glitch as well as observable X-ray variabilities. More specifically, the crust fracture could lead to a glitch of fractional frequency change $\Delta P/P$ as large as 10^{-5}, and the energy released in the magnetic field rearrangements would be conducted to the neutron star surface and result in an X-ray brightening of the pulsar. Both phenomena have indeed been observed from some magnetars. The SGR 1900+14 was found to exhibit a transient brightening after its 1998 August 27 giant flare. The X-ray flux of the pulsar stayed above the persistent level for about 40 days (Woods et al., 2001). The SGR 1627−41 went through an active episode that lasted about 6 weeks; X-ray monitoring showed that the pulsar's X-ray flux decayed over a time scale of ∼800 days (Kouveliotou et al., 2003). The AXP 1E 2259+586 went outburst in X-ray in 2002 and, simultaneously, exhibited a large glitch ($\Delta P/P = 3 \times 10^{-6}$; Kaspi et al. 2003; Woods et al. 2004).

Lyubarsky et al. (2002) expanded Thompson & Duncan (1996)'s calculation on the X-ray brightening of a magnetar after a crust fracture. They suggested that the heat released by magnetic field rearrangements could most likely be deposited into the outer crust of the neutron star where magnetic pressure starts to dominate over matter pressure. In such a scenario, the decay of the star's X-ray flux should follow a power law of index $\sim -2/3$. Their model fits the decay of SGR 1900+14's X-ray afterglow very well, in which a power law index of −0.7 was found (Woods et al., 2001). In our paper (Zhu et al. 2008, see Chapter 3 for details) we also find a similar index of -0.69 ± 0.03 in the decay of 1E 2259+586's 2002 outburst. Similarly, the decay trend of SGR 1627−41 followed a power law of index −0.47, but the power-law decay stopped at ∼800 days after the activation of the source and then declined sharply. This decay also can be explained by the heating and cooling of the neutron star crust, however, a more detailed model was needed (Kouveliotou et al., 2003). However, not all magnetar X-ray transient behaviours were observed to be fitted well by this model. The transient AXP XTE J1810−197 is called transient because it was discovered in 2003 when it suddenly became brighter by a factor of 100 (Ibrahim et al., 2004; Gotthelf et al., 2004a). Gotthelf & Halpern (2007) found that the flux of XTE J1810−197 after 2003 followed, surprisingly, an exponential decay of timescale 233.5 days. The AXP CXOU J164710.2−455216 was found to have brightened by a factor of ∼300 between two X-ray Multimirror Mission (*XMM*) observations taken 5 days apart in 2006 September (Israel et al., 2007). Candidate AXP AX 1845−0258, was discovered in an observation made in 1993 by *ASCA* (Gotthelf & Vasisht, 1998; Torii et al., 1998). Follow-up observations in 1999 showed that the source's flux had decreased by a factor of ∼10 (Vasisht et al., 2000). In 2003 Tam et al. (2006) found that AX 1845−0258 was undetectable by *Chandra* observations and inferred that its flux was even fainter (a factor of ∼260-430 fainter than observed in 1993). So far, the AXP outbursts showed decay behaviours similar to those of SGR giant flares, but they are much less energetic. Also, most of the burst energy is released during the afterglows of the AXP outbursts, while for SGR giant flares, the X-ray afterglows have less integrated energy than the flares themselves. More long-term radiative evolution studies of magnetars are needed in order to completely understand magnetar X-ray variability.

An interesting phenomenon was observed from the SGR 1900+14 following its 1998 August 27 giant flare (Woods et al., 1999). Its spin-down rate increased by a factor of ~ 2.3 for an interval of about 80 days. Inspired by this finding and also motivated by the need to explain the observed persistent X-ray spectra of magnetars, Thompson et al. (2002) refined the magnetar model to include a possible large-scale or global twist in the magnetosphere of magnetar (their model is now being referred to as the twisted magnetic field model). Such a global twist in magnetic field has various important possible outcomes. First, a strong current could be induced by the twisted magnetic field. It could up-scatter soft thermal photons into hard non-thermal photons, resulting in a hard spectral tail in the magnetar's X-ray spectrum. Second, the spin-down rate of the magnetar could be enhanced for a long time and could be indistinguishable from simple dipolar spin down. They also argue that the giant flares of magnetars must have been associated with or triggered by a sudden relaxation of the globally twisted magnetic field. This twisted magnetic field model not only explains the non-thermal component in the persistent X-ray spectrum of magnetars and the temporal spin-down increase observed from SGR 1900+14 following its giant flare, it also provided a basis for interpreting time-dependent effects observed in the SGRs and AXPs. Finally, Thompson et al. (2002) suggested that magnetars cannot remain luminous and active forever. Their strong toroidal fields that drive the twist in the magnetosphere will be depleted in $\sim 10^4$ yr, and then the magnetars will likely transition into XINSs (see Section 1.1.2 for an introduction to the XINSs).

There are also other models being proposed to explain the observed persistent X-ray spectra of magnetars. Özel (2001) proposed that a magnetar's X-ray emission originates from the neutron star's hot surface, but thermal emission from the surface is altered by the free-free absorption and scattering processes in the magnetosphere. Furthermore, if the surface magnetic field of the pulsar is as strong as 10^{15} G, the pulsar's X-ray emission would become highly beamed and spectrally hard due to the vacuum polarization resonance. As a result, a hard power-law-like spectral tail could emerge extending to energies as high as 10 keV. Özel et al. (2008) and Güver et al. (2008a) claim that the observed X-ray spectra of magnetars could be well fitted by this model.

Interestingly, magnetar emission has been detected in hard X-rays (20-80 keV), with power-law-like spectra of indices in the range -1.0 to 1.0 (Mereghetti et al., 2005; Kuiper et al., 2006; Kaspi & Boydstun, 2010). Another magnetar emission model is proposed by Beloborodov & Thompson (2007) suggesting that this non-thermal hard X-ray emission comes from a corona around the neutron star. This corona is formed due to particles being pulled out from the NS and accelerated to relativistic speeds by the currents induced by the twisted magnetic fields. These particles can be accelerated to such a high energy that pair creation avalanches could be initiated. The created pair particles will form a corona in the closed magnetosphere of the neutron star. Beloborodov & Thompson (2007) suggested that such a corona could be very hot and would emit in hard X-ray through thermal bremsstrahlung process. The spectrum of optically thin thermal bremsstrahlung emission resembles a power law of index -1 below its cut-off energy. The thermal bremsstrahlung radiation from the corona is expected to be harder for magnetars with stronger magnetic fields. However, Kaspi & Boydstun (2010) compiled a list of magnetars and compared their measured spectral indices in both soft and hard X-ray, and found that magnetars with higher magnetic fields tend to have softer spectral indices in hard X-ray. This is not consistent with the prediction of the corona model. Therefore, Kaspi & Boydstun (2010) suggested that perhaps the hard X-ray emission of magnetar comes from neutron star surface heated by the magnetic-twist-induced return currents. The stronger the magnetic field is, the more likely for the induced current to interact with soft photons through resonant scattering process, and thus leave less current to heat up the surface corona, resulting a softer spectrum in 20–80 keV.

In conclusion, although the magnetar model is very successful in explaining most of the observations, there is still much work to be done both in theory and in observation. We still do not completely understand the origin of magnetar emission. Detailed spectral or phase-resolved-spectral studies may shed a light on this matter. We still need to figure out the physical mechanism behind of the magnetar bursts and outbursts. The study conducted by me and my co-authors on the X-ray afterglow from the AXP 1E 2259+586 following its 2002 outburst established a fine example of an AXP outburst decay (see Chapter 3 for the details). The study by me and my co-authors on the long-term flux variations of AXP 1E 1841$-$045 (Chapter 4) suggested that, contrary to previous claims (Rea et al., 2005; Campana et al., 2007; Israel et al., 2007; Götz et al., 2007), AXP glitches and X-ray variations are not always correlated, i.e. there are radiatively quiet glitches from AXPs.

1.3 High-Magnetic-Field Pulsars

Based on the study of a large sample of isolated neutron stars, including most magnetars, some XINSs, and many ordinary radio pulsars, Pons et al. (2007) reported an intriguing correlation between the pulsar's blackbody temperature T, determined from the X-ray spectrum, and the magnetic field B, inferred from the spin-down ($T \propto B^{1/2}$). They also suggested that this correlation could be explained if the crusts of neutron stars were heated by magnetic-field decay, since it would significantly delay the cooling, particularly if the field were stronger than 10^{13} G. In fact, Pons et al. (2007) point out a simple model could account for the $T \propto B^{1/2}$ correlation. Assuming that the surface emission is powered by the magnetic energy in the neutron star crust ($\Delta R \simeq 1\,\mathrm{km}$ in thickness), then the balance between cooling and heating is expressed by:

$$-A_{\text{eff}}\Delta R\frac{dE_m}{dt} = A_{\text{eff}}\sigma T_{\text{eff}}^4, \tag{1.2}$$

where A_{eff} is the surface area of the neutron star, $E_m = B^2/8\pi$ is the magnetic energy density, σ is Stefan-Boltzmann constant, and T_{eff} is the effective surface temperature. Now if the magnetic field B decays exponentially over a time scale of τ_D,

$$\frac{dB}{dt} = -\frac{B}{\tau_D}. \tag{1.3}$$

Following the above two assumptions, we have $\Delta RB^2 = 64\pi^2\tau_D^2\sigma T_{\text{eff}}^4$ ($T \propto B^{1/2}$).

A similar correlation was also expected if the core of the neutron star is heated by magnetic field decay, with heat transfer out to the surface, leading to an increase of the surface temperature (Arras et al., 2004). Aguilera et al. (2008) expanded the work of Pons et al. (2007) through 2D cooling simulations that included anisotropic thermal conductivity and all relevant neutrino emission processes for realistic neutron stars, in an attempt to unite magnetars and XINS in a simple picture of heating by magnetic field. Their study shows that the XINS could be explained if they are old neutron stars ($\sim 10^6$ yr) born with 10^{14}–10^{15} G magnetic fields, or if they are middle-aged neutron stars born with 10^{13}–10^{14} G magnetic fields. This theory predicts that pulsars with magnetic fields higher than 10^{13} G should be hotter than is predicted by a simple cooling model with lower magnetic field, regardless of whether they are radio-quiet or not. Therefore, observing high-magnetic-field radio pulsars at X-ray energies and measuring the temperature of their thermal radiation may help us unify the different classes of isolated neutron stars.

Observationally, one high-B RPP, although not a radio pulsar, has exhibited magnetar-like bursting behaviour whereas some magnetars are observed to be emitting at radio wavelengths. The magnetar XTE J1810−197 is a transient AXP, first detected in outburst (Ibrahim et al., 2004). This magnetar, originally not emitting in the radio band, was observed to have radio pulsations one year after an X-ray outburst (Camilo et al., 2006). Also, the magnetar 1E 1547.0−5408 shows radio pulsations (Camilo et al., 2007a). Though not a radio pulsar, the high-B rotation-powered ($B = 4.9\times10^{13}$ G) X-ray PSR J1846−0258 exhibited a sudden, magnetar-like

X-ray outburst that lasted for a few weeks in 2006 (Gavriil et al., 2008). Thus, it is possible that the high-B RPPs are magnetars in quiescence. Recently, a new magnetar, PSR J1622−4950, was discovered via its active radio emission, yet is relatively X-ray-faint (Levin et al., 2010). This further suggests that there could be a large, unseen population of quiescent magnetars, some of which may be 'disguised' as radio pulsars.

Several high-B pulsars have been observed by focusing X-ray telescopes (for a more detailed summary, see Ng & Kaspi 2010):

PSR J1847−0130 is a 6.7 s-period radio pulsar discovered by McLaughlin et al. (2003). It has the highest spin-down magnetic field of all known radio pulsars ($B = 9.4 \times 10^{13}$ G), and even higher than that of AXP 1E 2259+586 and SGR 0418+5729. McLaughlin et al. (2003) also looked into archival *ASCA* data that cover this pulsar's coordinates, but failed to detect its X-ray counterpart. Given its distance of ~ 8.4 kpc, an upper limit of 5×10^{33}erg s^{-1} on its 2–10 keV luminosity was derived based on the *ASCA* observation. This equals $10\dot{E}$ of the pulsar, therefore, is not a constraining upper limit. The difficulty is that this pulsar is very distant.

PSR J1734−3333 is a 1.2 s-period radio pulsar with a B field of 5.2×10^{13} G. A faint X-ray counterpart of this pulsar was detected by recent deep *XMM* observations (Olausen et al., 2010). Being not very constraining, the observation revealed a surface temperature of $0.25^{+0.13}_{-0.08}$ keV and a 0.5–2 keV X-ray luminosity of about 0.1 of its spin-down power, not as luminous as the AXPs, but still rather atypical for a rotation powered pulsar. Interestingly, long-term radio timing observations show that this pulsar has a braking index of $n = 1.0 \pm 0.3$. This is not in agreement with the dipolar magnetic field model. One possible interpretation is that the pulsar's magnetic field may be increasing overtime, which means, on the P-$\dot{P}$ diagram this pulsar is moving toward the magnetar region (Espinoza et al., 2011a).

PSR J1819−1458 is one of the Rotating Radio Transients (RRATs) discovered by McLaughlin et al. (2006). RRATs are a peculiar kind of radio pulsar which are detectable only through their sporadic radio bursts, or single pulses (McLaughlin et al., 2006). It has a period of 4.3 s and a magnetic field of $B = 5 \times 10^{13}\,$G. *XMM* observations have detected the X-ray counterpart of this RRAT (Rea et al., 2009a). Its spectrum is approximately thermal and also appears to have an absorption feature at 1 keV. The absorption feature can be well modeled by a Gaussian or resonant cyclotron absorption model (the `cyclabs` model in `xspec`). When fitted with a blackbody plus cyclotron scattering model, the best-fit kT is $0.144^{+0.008}_{-0.006}\,$keV. The 0.3–5 keV unabsorbed flux of the RRAT is 1.5×10^{-13}erg s^{-1} cm^{-2}. This flux corresponds to an X-ray luminosity of $L_X \sim 4 \times 10^{33}$erg s^{-1}, more than an order of magnitude higher than the $\dot{E}$ of the RRAT. Clearly, this thermal emission could not have been powered by return current heating (Section 1.1.1). It could be the result of initial heating, or more likely, the result of magnetic-field-decay heating given the observed blackbody temperature kT. A later *Chandra* observation of this RRAT revealed a possible Pulsar Wind Nebula (PWN) as there was extended structure seen at $\sim 5''.5$ and $13''$ in radius (Rea et al., 2009a). The total power of this extended emission is $L_{\rm PWN;0.5-8\ keV} \sim 6\times10^{31}$erg s^{-1}$\simeq 0.2\dot{E}$. The efficiency seems much higher than that of PWNe from other normal pulsars (Kargaltsev & Pavlov 2008 proposed an empirical trend $\log L_{\rm PWN;0.5-8\ keV} = 1.6 \log \dot{E} - 24.2$). This implies that there has to be an additional source of energy for the PWN, such as the magnetic energy of this pulsar. Another possibility is that this extended emission could be composed of a smaller bow shock ($5''.5$ in radius) and a larger supernova remnant (extending to $13''$ in radius). However, based on the observed size of the emission, the inferred projected speed would be too small for J1819−1458 to power a bow shock; also, this pulsar's spin-down age is $\sim$ 117 kyr, too old to have a supernova remnant. Finally, Rea et al. (2009a) suggest that this extended emission could be a PWN powered by magnetic field energy of this pulsar released through mechanisms such as ambipolar diffusion. So far, no such magnetically powered PWN has been observed around magnetars (Olausen et al., submitted), but magnetars' brightness and large distance could have precluded us from detecting such PWNe. It is also hard to detect such PWN from the other high-magnetic-field pulsars given their large distances (though

PWN has been detected around PSR J1846−0258; see below).

PSR J1846−0258 is a 0.33 s-period, 4.9×10^{13} G high-B X-ray RPP in the centre of the SNR Kes 75. It is one of the youngest known pulsars (~ 800 yr). Its huge spin-down power $\dot{E} = 8.1 \times 10^{36} \mathrm{erg\,s^{-1}}$ powers a bright PWN (Ng et al., 2008). Despite having a magnetar-like magnetic field, PSR J1846−0258 has been spinning down steadily with a braking index of $n = 2.65 \pm 0.01$ (Livingstone et al., 2006). All of these properties fit well into the picture of a RPP, until the pulsar exhibited signature magnetar behaviour in July 2006: a large glitch and a major X-ray outburst (Gavriil et al., 2008; Kumar & Safi-Harb, 2008; Livingstone et al., 2010). This magnetar-like outburst showed that this high-B pulsar might be a transition object between RPPs and magnetars. However, some argue that this outburst still can be explained within the picture of a RPP (Kuiper & Hermsen, 2009).

PSR J1119−6127 is very similar to PSR J1846−0258; it is a young (1.7 kyr), 0.41 s-period, high $\dot{E}$ ($2.3 \times 10^{36} \mathrm{erg\,s^{-1}}$), high-$B$ (4.1×10^{13} G) pulsar in the centre of SNR G292.2−0.5 (Camilo et al., 2000). PSR J1119−6127 was observed using *XMM* (Gonzalez et al., 2005) and *Chandra* (Safi-Harb & Kumar, 2008). Based on the *Chandra* observation, its X-ray spectrum is well fit by a blackbody plus power-law model (BB+PL) with $kT = 0.21 \pm 0.01$ keV and $\Gamma = 1.9^{+1.1}_{-0.9}$ or a Neutron Star Atmosphere model (NSA; Pavlov et al. 1995; Zavlin et al. 1996) plus power law with $kT = 0.14^{+0.03}_{-0.02}$ keV and $\Gamma = 1.5 \pm 0.8$. The *Chandra* observation also revealed a faint PWN around the pulsar. The existence of the PWN and the ratio of X-ray luminosity to spin-down power fit well in the picture of a young and powerful RPP. Curiously, the *XMM* observations shows that the soft part of the pulsar's X-ray radiation is highly pulsed (pulsed fraction $PF = 74\% \pm 14\%$, Gonzalez et al. 2005). However, thermal radiation from the neutron star surface is not expected to be highly pulsed due to gravitational light bending effects. Therefore, current models of thermal emission from neutron stars is being challenged by the observation of PSR J1119−6127. It has been suggested that including the light beaming effects caused by very high surface magnetic field might help explain the observed high pulsed fraction (Gonzalez et al., 2005). An alternative explanation proposed by Melikidze et al. (2007) is that the pulsar's surface magnetic field differs significantly from a pure dipole field, resulting in a particular surface temperature distribution that may lead to highly pulsed thermal radiation.

PSR B0154+61 is a 2.35 s-period, high-B (2.1×10^{13} G) radio pulsar (Davies et al., 1972). It has a spin-down age of 197 kyr, a distance of $\sim$ 1.7 kpc according to its Dispersion Measure (DM) of 30.21 $\mathrm{cm^{-3}pc}$ and the Galactic free electron density model (Cordes & Lazio, 2002), and a spin-down power of $\dot{E} = 5.7 \times 10^{32}\mathrm{erg\,s^{-1}}$. Its close distance and low $\dot{E}$ makes it a good observational target for finding evidence of magnetic field decay heating. Unfortunately, an *XMM* observation of it taken on 2003 March 6 failed to detect it and resulted in only upper limits on its X-ray luminosity $L_X \lesssim 1.4\times10^{32}\mathrm{erg\,s^{-1}}$ and temperature $kT \lesssim 73\,\mathrm{eV}$ assuming a blackbody spectrum (Gonzalez et al., 2004a).

PSR B1916+14 is a 1.2-s radio pulsar, with spin-down-inferred magnetic field $B = 1.6 \times 10^{13}$ G, spin-down age $\tau = 8.8 \times 10^{4}$ yr, and $\dot{E} = 5 \times 10^{33}\mathrm{erg\ s^{-1}}$ (Hulse & Taylor, 1974; Manchester et al., 2005). It is a relatively young pulsar and also relatively nearby (the radio DM indicates a distance of $\sim$2.1 kpc). Given its age and distance, PSR B1916+14 should still be hot enough to be X-ray detectable, according to a minimal pulsar cooling model, without magnetic-field-decay heating (Page et al., 2006). It is also a high-B pulsar and may therefore be hotter because of magnetic-field decay. This makes PSR B1916+14 a good test subject for neutron star cooling models, and hence X-ray observations. We proposed and were granted a $\sim$ 25 ks *XMM* observation of PSR B1916+14 in 2008. Our analysis results are presented in Chapter 5.

PSR J1718−3718 is a radio pulsar discovered in the Parkes Multi-beam Survey (Hobbs et al., 2004). It is a 3.3 s-period radio pulsar, with spin-down inferred characteristic age $\tau_c = 34$ kyr, spin-down power $\dot{E} = 1.6 \times 10^{33}$ $\mathrm{erg\,s^{-1}}$, and surface dipole magnetic field $B = 7.4 \times 10^{13}$ G. Its magnetic field is the second highest of all known RPPs and is higher than that of the lowest field magnetar AXP 1E 2259+586. An X-ray source was serendipitously detected at the radio position of PSR J1718−3718 in a 2002 *Chandra* observation. Kaspi & McLaughlin (2005) found that this X-ray source had a soft, thermal-like spectrum, and therefore is the likely X-ray counterpart of the radio pulsar. However, due to the limited photon statistics (see Table 6.1), the spectral results were not very constraining. Also, the coarse time resolution (3.24 s) in the timed exposure mode observation prevented pulsations from being detected. Deeper *Chandra* observations with higher time resolution were proposed and conducted in 2009. Interestingly, a large period glitch occurred between 2007 September and 2009 January (Manchester & Hobbs, 2011). Four *Chandra* X-ray observations, each separated by ~ 2 months, were taken in the hope of detecting X-ray variability, possibly associated with the glitch, as occurred in the 2006 outburst of PSR J1846−0258 (Gavriil et al., 2008; Livingstone et al., 2010). In Chapter 6 we report on a temporal analysis of the four new *Chandra* observations of PSR J1718−3718 , as well as on a spectral analysis which also includes the archival 2002 observation.

The magnetar-like behaviour observed from high-B pulsar PSR J1846−0258 suggests that the high-B pulsars may be a transition class of objects between RPPs and magnetars. However, the outburst rate of high-B pulsars appears to be low, as so far only one such event have been observed. On the other hand, finding evidence of magnetic field decay heating from high-B pulsars would also help prove the connection between the two classes of objects. This is a part of the motivation of our papers on high-B PSRs B1916+14 and J1718−3718; see Chapters 5 and 6 for details.

2

X-ray Astronomy

2.1 Brief History of X-ray Astronomy

X-rays are photons with energies around 0.1 keV to 500 keV (~0.002 nm–10 nm). Cosmic X-rays mostly come from hot gas/plasma or relativistic electrons accelerated by strong electric and magnetic fields. For example, the solar corona is made of optically thin plasma of temperature 10^6 K, and mainly radiates in X-rays through thermal bremsstrahlung (free-free emission). The hot gas in the centre of clusters of galaxies also emits thermal bremsstrahlung radiation in X-rays, making them an important class of extragalactic X-ray sources. Most of the bright X-ray sources in the Galaxy are neutron stars and black holes accreting from their binary companions. The hot gas on their surface or in their accretion disks emits strong thermal X-ray radiation. There is also non-thermal X-ray radiation coming from X-ray pulsars, and the Crab nebula and other so-called PWN. In most of these non-thermal radiation processes, magnetic fields play a vital role.

X-rays are so powerful that they will easily ionize atoms. This makes X-rays particularly vulnerable to photoelectric absorption. Photoelectric absorption prevents us from observing any celestial X-rays from the ground, because the Earth's atmosphere can almost completely absorb them. This is why X-ray astronomy only started in the 1950s when we started sending rockets with X-ray detectors above the Earth's atmosphere. Even with the X-ray satellites we now have, photoelectric absorption is still a serious problem for X-ray astronomy. For most extrasolar objects, we usually have to model the photoelectric absorption caused by the interstellar gas along the light of sight in order to determine the intrinsic spectrum of the source. Because photoelectric absorption increases exponentially with the amount of gas along the line of sight, many X-ray sources near the Galactic centre are buried by the dense gas and are virtually undetectable.

The first solar X-rays were observed on August 5, 1948, by a detector on a US army V-2 rocket that was launched to above the Earth's atmosphere (Keller, 1995). The first extrasolar X-rays, coming from the accreting neutron star Scorpius X-1, were detected on June 12, 1962 by an Aerobee 150 rocket (Giaconni et al., 1962; Shklovsky, 1967). In the following years, various rocket flights detected dozens of other X-ray sources, including the Crab Nebula and M87. In the mean time, several satellites were launched to study the Sun's electromagnetic radiation. These include the Solar Radiation satellite program (SOLRAD) in the late 1950s, the Orbiting Solar Observatories (OSO) in the 1960s. In the 1970s, some early X-ray all-sky surveys were performed by satellites such as OSO-7, -8 and Skylab (Vanderhill et al., 1975). The first satellite dedicated to X-ray astronomy was the *UHURU* observatory, launched on December 12, 1970. This satellite performed an X-ray all-sky survey and systematic monitoring of some variable Galactic X-ray sources. Many variable Galactic X-ray sources were identified as accreting neutron stars. For a few of the variable sources, the masses of the accreting objects were found to be greater than the upper mass limit of a stable neutron star, make them strong candidates for black holes. *UHURU* also discovered the emission of intergalactic hot gas inside clusters of galaxies (Gursky et al., 1972). This was a very important discovery especially to the field of cosmology. The *UHURU* all-sky survey covered all the 2–6 keV sky. The result was the first comprehensive X-ray catalog (the 4U catalog, Forman et al. 1978), which contained 339 Galactic and extragalactic objects.

The first focus-imaging X-ray observatory was the *Einstein* X-ray observatory, also known as the High Energy Astronomy Observatory 2 (HEAO-2), launched November 13, 1978 (Giacconi et al., 1979). It carried a grazing-incidence focusing X-ray telescope (Wolter type I; see Section 2.2.2 for details) that provided arc-second level angular resolution. It was able to make very deep surveys over a small area of the sky, and detect many different astronomical objects, including normal stars.

Following in the foot steps of the *Einstein* observatory, the *ROSAT* satellite (launched June 1, 1990, stopped observing on February 12, 1999; Truemper 1993) carried a telescope that provided the same angular resolution as that of the *Einstein* observatory, but much larger collecting area. In its ten-year mission, the *ROSAT* satellite greatly increased the number of X-ray sources known. *ROSAT* was also one of the first X-ray missions to open up guest observer opportunities to scientists worldwide.

The *XMM* and *Chandra* observatories (see Sections 2.3 and 2.4 for more details) are the next generation focusing X-ray telescopes after *ROSAT* ; they were both launched in 1999. Both of them use type I Wolter mirrors (see Section 2.2.2). *XMM* 's telescope consists of 58 nested layers of Wolter mirrors (Figure 2.3) made of thin foils, which give *XMM* its very large total collecting area ($\sim$5000 cm^2), $>$ 1 order of magnitude compared to *ROSAT* and $>$ 2 orders of magnitudes greater than *Einstein* (Jansen et al., 2001). *Chandra* 's telescope consists of only 4 sets of mirrors (Figure 2.6) made of glass, which gives them less collecting area than the mirrors of *XMM* . But the glass mirrors are so precisely manufactured that they can achieve sub-arcsecond ($\sim 0.3''$) angular resolution. Both *XMM* and *Chandra* also benefit from technology improvements in the X-ray detectors. Instead of the proportional counters and gas/solid spectrometers used by *Einstein* and *ROSAT* (see Section 2.2.1), they both use Charge Coupled Devices (CCDs), which give them better image quality and energy resolution than those of the past missions. Furthermore, both *XMM* and *Chandra* are equipped with grating instruments with spectral resolution orders magnitude better than that of the *Einstein* and *ROSAT* satellites. The era of *Chandra* and *XMM* is still ongoing, and many exciting discoveries have been made by these amazing observatories. See Sections 2.3 and 2.4 for more information on *XMM* and *Chandra* .

The *ASCA* (Tanaka et al., 1994) and *Suzaku* (Mitsuda, 2007) observatories are also focusing X-ray telescopes like *Einstein* , *ROSAT* , *XMM* and *Chandra* . *ASCA* was launched on February 20, 1993 and decommissioned on March 2, 2001. Onboard it were four X-ray telescopes of total effective area of $1300\,\mathrm{cm}^2$, spatial resolution of $3'$ and Field of View (FOV) of $24'$ in diameter at 1 keV. The readout detectors include the Gas Imaging Spectrometers (GISs; Burke et al. 1994; 0.8–12 keV) and the Solid-state Imaging Spectrometers (SISs; Ohashi 1996; 0.4–12 keV). *Suzaku* was launched on July 10, 2005 and is still operating. Onboard are five nested conical thin-foil grazing incidence X-ray Telescope (XRT), with angular resolution of $\sim 2'$; one X-ray spectrometer (XRS; FOV $2\overset{'}{.}9 \times 2\overset{'}{.}9$ in 0.3–12 keV) and four X-ray Imaging Spectrometers (XISs Koyama 2007; FOV $18' \times 18'$ in 0.2–12 keV) are installed on the focal plane of these telescopes.

The multi-wavelength observatory *Swift* was launched on December 11, 2004. It is dedicated to the study of GRB science. Its three instruments, Burst Alert Telescope (BAT, gamma-ray telescope; Barthelmy et al. 2005), X-ray Telescope (XRT; Burrows et al. 2000) and Ultraviolet/Optical Telescope (UVOT) are designed to capture the X-ray, Ultraviolet and Optical afterglow of GRBs. The BAT monitors a large fraction of the sky for gamma-ray bursts of 15–150 keV. Once a gamma-ray burst is detected by BAT, its coded-aperture mask design enables it to locate the burst to $1'$–$4'$ accuracy in a short time. Then the satellite quickly slews toward the event location, allowing the XRT and UVOT to observe the immediate burst afterglow. The XRT uses a type I Wolter telescope (Section 2.2.2) and a Metal Oxide Semiconductor (MOS) CCD camera as a backend. It has $18''$ spatial resolution at 1.5 keV, 50–190 eV spectral resolution and a total effective area of $110\,\mathrm{cm}^2$ at 1.5 keV. *Swift* is not only a great observatory for studying gamma-ray bursts, it is also excellent for observing transient gamma/X-ray events such as magnetar bursts and outbursts.

Although most of the X-ray satellites were designed to look deeper into the sky and gain better spatial/spectral resolution than their precursor, there is one satellite that aimed differently, the Rossi X-ray Timing Explorer (*RXTE*; Jahoda et al. 2006)[1]. *RXTE* was launched on December 30, 1995, after *Einstein* and *ROSAT* observatories. It does not have a focus-imaging telescope with it. Its primary instrument is an array

---

[1] http://heasarc.gsfc.nasa.gov/docs/xte/rxte.html

of five proportional counters a.k.a Proportional Counter Array (PCA) with a total of 6500 cm^2 collecting area in the 2–60 keV range. It covers a wide 1 square degree field of view, as defined by its collimator. The PCA is notable for its unprecedented 1-μs time resolution. The second instrument, the High Energy X-ray Timing experiment (HEXTE) is a hard X-ray (15–250 keV) detector, consisting of two clusters of 4 NaI/CsI scintillation counters with a total collecting area of 1600 cm^2, a FOV of 1 square degree and a time resolution of 8 μs. The third instrument on-board *RXTE* is the All Sky Monitor (ASM) (Levine et al., 1996). It consists of three wide angle coded-aperture telescopes with position-sensitive Xenon proportional counters (operates in 1.5–12 keV) as backends. It is designed to monitor bright X-ray sources for variations. *RXTE*'s very high time resolution and large collecting area make it an idea tool for studying transient X-ray sources such as high-energy pulsars and accreting binaries. Discoveries made by *RXTE* have greatly extended our knowledge of the varying X-ray sky.

2.2 Instruments for X-ray Observations

2.2.1 X-ray Detectors

In this section, I introduce contemporary X-ray detectors, including proportional counters, scintillation detectors, CCDs and transition edge sensors. Most of these X-ray detectors are based on a similar basic idea: detecting the electrons emitted in the photoelectric process.

The proportional counter consists of a tube or box filled with inert gas and with a positively charged wire down the middle. An incident X-ray photon knocks out a high energy electron from a gas atom, and this electron has enough energy to ionize even more atoms around it. As a result, every X-ray photon will be able to create a number of free electrons proportional to its energy when it hits the gas tube. Subsequently, the electrons accelerate toward the positively charged wire. The voltage on the wire is chosen such that the electrons would be accelerated so rapidly that they will lead to a cascade of even more electrons. Eventually a electronic pulse would be detected on the middle wire with the amount of charge proportional to the energy of the incident X-ray. This detector works for X-rays below the energy of 20 keV, because harder X-rays tend to pass through the gas medium without being absorbed.

Photoelectric absorption also happens in solids, except that in a gas one creates an electron-ion pair by the photoelectric process, while in a solid one creates electron-hole pairs. It turns out that, because the atomic nuclei are very close to each other in the solid, it takes less energy to liberate an electron from solid lattice ($\sim 3\,\mathrm{eV}$ for silicon) than it takes from a single atomic nucleus ($\sim 30\,\mathrm{eV}$). This means an X-ray photon would create 10 times more electrons in a solid medium than it would in the gas. As a result a solid proportional counter would have better energy resolution than a gas one. However, the difficulty in making a solid proportional counter is that the solid medium has to be very pure and insulated. Even a small conductivity would lead to a large leakage current and significantly reduce the signal-to-noise ratio. With careful manufacturing, such problems can be mitigated using semiconductors. However, because of the technological advancement in semiconductors, the CCDs have been introduced to X-ray astronomy. An X-ray CCD is also a kind of solid state detector, but instead of applying a strong field to induce an electron cascade, rows of potential wells are set up in the silicon to trap those liberated electrons, and by moving the potential wells one can transport the electrons to read-out nodes attached to one side of the CCD. The advantage of a CCD is not only its better spectral resolution, but also the fact that one can infer the location of the incident X-rays on the CCD. Nowadays, CCDs are widely used as the backends of focus-imaging X-ray missions. For more details see Longair (1997).

In recent years, technology advancement has led to some new detector designs, such as microchannel plate detectors (Joseph, 1979), and super-conducting Transition Edge Sensor (TES) micro-calorimeter (Irwin et al., 1996).

The microchannel plate is a plate of highly resistive material, with a lot of microchannels (micrometers in diameter and separation) on it. The channels are usually parallel to each other and enter the plate with an angle (degrees from normal). The plate is typically $\sim$ 2 mm in thickness, and there is a strong electric field applied through the plate along that 2 mm distance. Each channel works like a photomultiplier. An electron liberated by an incident X-ray will go through a channel and bounce off the channel wall multiple times, and each time more electrons would be liberated and eventually an electron cascade happens in the 2 mm channel and a detectable electric pulsed would be detected on the backside of the plate. *Chandra*'s High Resolution Camera (HRC) has a microchannel detector as backend. It has very high time resolution (16 μs; Zombeck et al. 1995).

A calorimeter generally contains a thermometer that detects tiny changes in temperature in a substance. The use of calorimeter in astronomy usually involves measuring the change of temperature in some substance after it absorbed the radiation from astronomical objects. There are many ways to measure the temperature. One of the best ways in astronomy is to use the TES. The TES is a very accurate thermometer for a narrow range of temperature. It is made of super-conductive materials kept at almost the exact temperature of its super-conductive phase transition. This way if the temperature of the material changes even by a very small fraction, the resistance of the material will change a lot. This property made the TES very a sensitive thermometer. If carefully designed, the TES could be used to detect the temperature changes caused by X-ray photons. It is possible that the future X-ray mission International X-ray Observatory (IXO)/Advanced Telescope for High Energy Astrophysics (ATHENA) will use a TES microcalorimeter as the backend of its spectroscopy X-ray telescope.

Using these detectors, the best spectral resolution one can achieve is about $E/dE \sim$ 50 (using CCDs; section 2.3). However, progress in observational techniques, especially the use of focus-imaging telescopes, made it possible for grating spectrometers to be used at X-ray energies (*XMM* Reflecting Grating Spectrometer (RGS), den Herder et al. 2001; *Chandra* Low Energy Transmission Grating (LETG)[1]; High Energy Transmission Grating (HETG)[2]). These grating spectrometers can achieve a

---

[1] http://cxc.harvard.edu/cal/letg/

[2] http://cxc.harvard.edu/cal/Hetg/

spectral resolution as high as $E/dE \sim 1000$, at the cost of losing a significant portion of collecting area.

2.2.2 Wolter Mirrors

To focus X-ray photons is very difficult because X-rays are hard to reflect or deflect at a normal incident angle. Most of them will be absorbed through the photoelectric process. As a result, in the early days of X-ray astronomy, the collimator was one of the only options to achieve angular resolution. The collimator is just a long metal tube that blocks light from a wider angle, and limits the field of view of the detector to a small region of the sky. However, X-rays can be reflected, if they strike in a very shallow angle close to the reflecting surface (usually $< 2^\circ$ for 0.1–10 keV X-rays, for grazing incidence reflection). Based on this principle, Wolter (1952) proposed three designs of grazing incidence telescope systems (Figure 2.1). The type I Wolter telescope is now widely used by modern focus-imaging X-ray missions (e.g. *Einstein*, *ROSAT*, *XMM*, *Chandra*, *NuSTAR*; see section 2.1 for details). In the Wolter telescopes, the X-rays are reflected twice by two sections of grazing incidence mirrors, the first one in a paraboloid shape, the second in a hyperboloid shape. The second reflection is designed to reduce the effect of aberrations and give the telescope a larger field of view (see Smith 1995 for a more detailed discussion). One set of mirrors has very small effective area; therefore, to increase the filling factor, many sets of mirrors can be nested in a coaxial configuration. For instance, *XMM* 's telescope is made of 58 sets of nested Wolter type I mirrors.

2.2.3 Coded Aperture Mask Imaging

Focusing of hard X-rays (> 20 keV) is very difficult even for the grazing incidence telescopes. This is because the maximum grazing angle becomes extremely small for them and so the telescope must have a focal length much longer than tens of metres. This idea of the coded aperture mask is somewhat similar to that of the pinhole camera, which is an imaging device with only straight-line optics. The problem of using a pinhole camera for astronomy is that one must sacrifice collecting area to

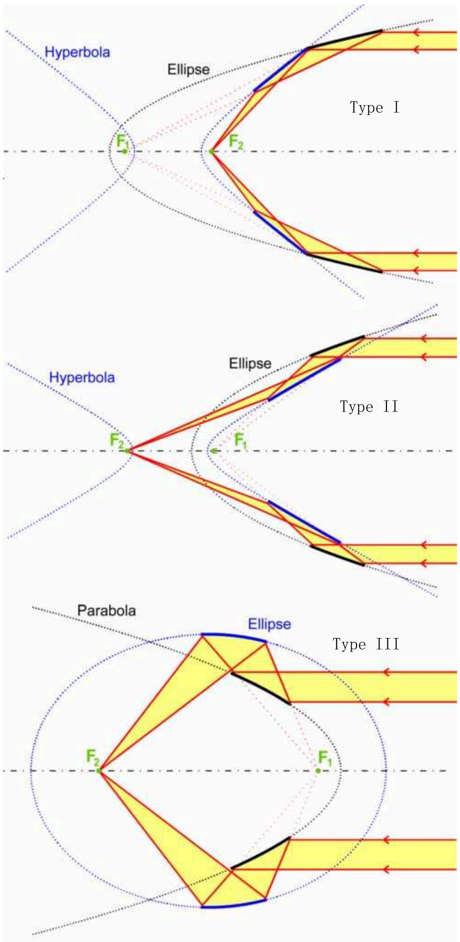

Figure 2.1 Wolter Telescope optics type I, II, and III.

Figure adopted from `http://www.x-ray-optics.com` gain angular resolution. What if one could combine multiple pinhole cameras to gain both collecting power and imaging resolution? The coded aperture mask (Barrett & Horrigan, 1973) is designed to do exactly this. The coded aperture mask is a plate mask with many carefully selected semi-random “pinholes” on it. The images on the detector created by these “pinholes” are convolved with each other. With a carefully designed mask, it is possible to deconvolve these images and restore the original image. To make this possible, the coded mask must satisfy one condition: the autocorrelation of the mask pattern should be a delta function. It turns out there are certain patterns that satisfy this condition (Gunson & Polychronopulos, 1976; Fenimore & Cannon, 1978). The detailed construction and design of coded aperture mask telescopes have evolved over years, as well as the deconvolving techniques (see Busboom et al. 1998 and references therein). Coded aperture masks have been used in some X-ray missions such as *RXTE*-ASM (Levine et al., 1996), *Swift*-BAT (Barthelmy et al., 2005).

2.3 The XMM-Newton Telescope

The work presented in the following chapters was based mostly on data collected by the *XMM* and *Chandra* observatories; in Chapter 4 we also used the *ROSAT* and *Suzaku* observatories. In this and the next section I will introduce the primary instruments that I used during my PhD study: the European Photon Imaging Camera (EPIC) onboard *XMM* and the ACIS on *Chandra*.

The *XMM-Newton* space observatory (Jansen et al., 2001) was launched on December 10, 1999 by the European Space Agency. The spacecraft is in a 48-hr, highly eccentric Earth orbit, with a perigee of 7000 km and an apogee of 114,000 km. The EPIC instrument on board this spacecraft is composed of three X-ray mirrors and three sets of CCD cameras at the focus of each mirror (see Figure 2.2); the mirrors are 58 Wolter type I mirrors nested in a coaxial and confocal configuration (see Figure 2.3; Jansen et al. 2001), with focal length of 7.5 m and largest diameter of 70 cm. The three X-ray mirrors have an angular resolution of $15''$ half-energy width at 1.5 keV and 8 keV [corresponding to a $6.6''$ Full Width of Half Maximum (FWHM) Point

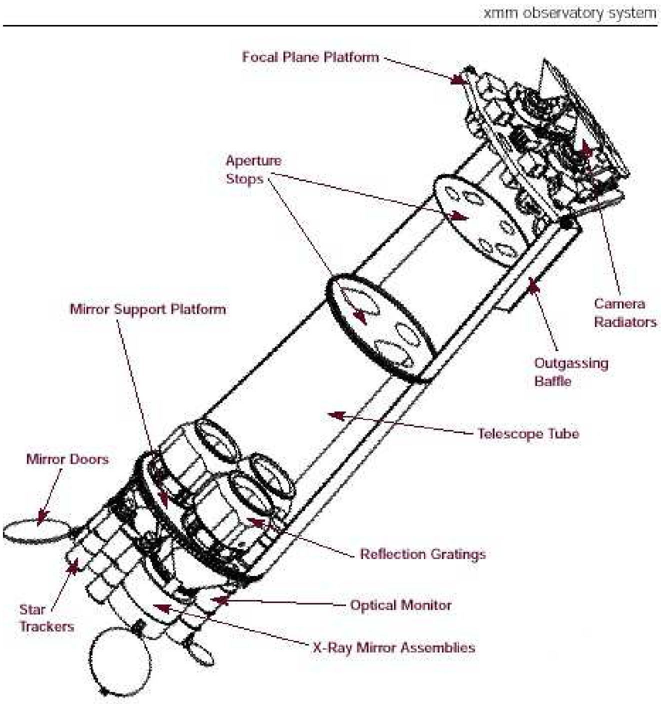

Figure 2.2 The schematics of the *XMM* observatory.

`http://sci.esa.int/science-e/www/object/index.cfm?fobjectid=47056`

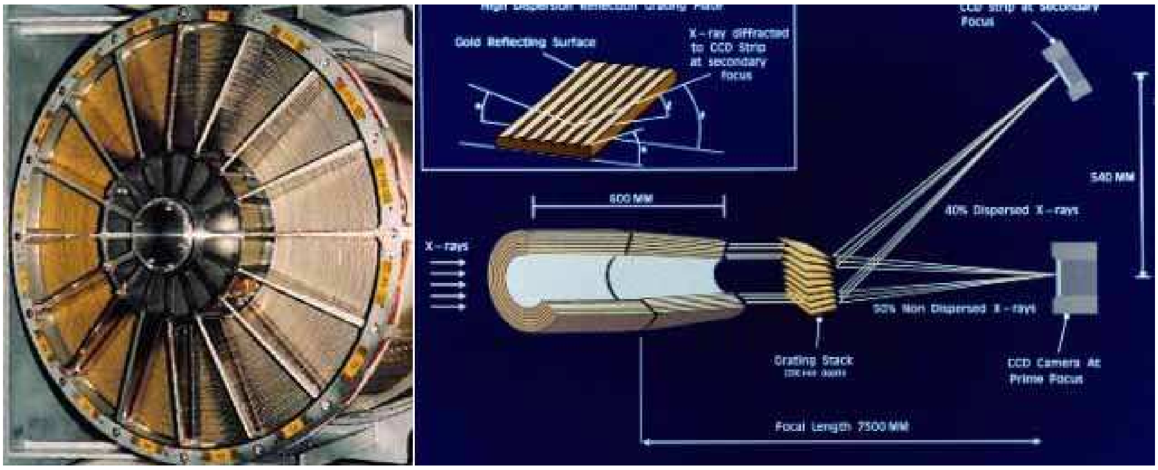

Figure 2.3 Left: The 58 type I Wolter mirrors of *XMM* observatory. Right: A schematic view of *XMM* observatory's optic system.
`http://sci.esa.int/science-e/www/object/index.cfm?fobjectid=39320`

Spread Function (PSF)] and a 30′ diameter circular FOV. The nested mirrors give each of *XMM* 's three cameras a collecting area of about 1500 cm^2. Two of the CCD cameras contain seven MOS CCDs (Turner et al., 2001), and third contains twelve pn CCDs (Strüder et al., 2001). However, the light path to the MOS cameras is obscured; $\sim$ 50% of the X-rays are diverted to the RGS (den Herder et al., 2001), leaving only 44% of the original flux to the MOS CCDs.

The layouts of the pn CCDs are shown in Figure 2.4. A total of 12 $3{\times}1\,\mathrm{cm}^2$ (200×64 pixels) CCDs were put together in a $6{\times}6$ cm^2 square that covers a 27′ diameter field of view. The CCD pixel size is $150\,\mu\mathrm{m}{\times}150\,\mu\mathrm{m}$ (4.1″ in angular size), designed to be slightly better than the 6.6″ FWHM of the telescope's point spread function. Onboard tests show that an extended source in the centre of the FOV can be studied with $\sim 5''$ spatial resolution.

In the CCDs, the electrons liberated by the X-rays are transported to the readout node on the side of the CCDs during the readout time (see Section 2.2.1). The readout takes a small amount of time during which the CCD cannot properly register photon information. It is usually much smaller than the exposure time of the CCD, also known as its frame time. The on-board computer can reconstruct the image and

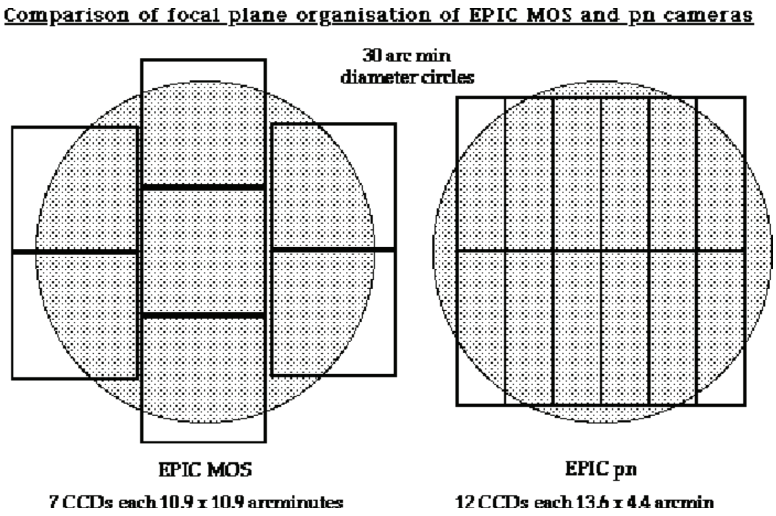

Figure 2.4 The layout of the MOS and pn CCDs. See the *XMM* user hand book for the original plot.

`http://xmm.esa.int/external/xmm_user_support/documentation/uhb/node24.html`

spectrum of the source based on the number and order of the electrons it collected from the readout nodes. For the *XMM* pn CCDs, the frame time depends on the observational mode, but the readout time is always about 4.6 ms.

In order for such a CCD spectrometer to work, each of its pixels must read out no more than one photon at a time in order to properly register the energy of the photon, but this requires a faster read out rate (shorter frame time) if the source is very bright. If the read out rate is not sufficient, and a pixel is hit by two or more photons during the frame time, then the on-board computer will assume that the electrons knocked out by the two photons are from a single photon event of a higher energy. This is called a “pile-up” event. Too many pile-up events could significantly alter the observed source spectrum, and it can be hard to reconstruct the original spectrum. Therefore, different readout modes were implemented in order to observe different brightness sources. The “extended full frame mode” is designed for observing faint extended sources. It has all CCDs in operation and the longest frame time (199.2 ms). The “full frame”, “large window” and “small window modes” are used in observing faint, medium or bright point sources. For the latter two modes, only part of the

Table 2.1. Parameters of the six different readout modes for the pn camera. Table adapted from Strüder et al. (2001).

Mode	FOV(pixels)	Frame time (ms)	Readout time (ms)	Count rate limit[a]	$f_{\rm limit}$[b]
Extended full frame	398×384	199.2	4.6	⋯	⋯
Full frame	398×384	73.3	4.6	6	8.1×10^{-12}
Large window	198×384	47.7	0.72	9	1.2×10^{-11}
Small window	63×64	5.7	0.72	104	1.4×10^{-10}
Timing	199×64	0.03	very small	4000	5.9×10^{-9}
Burst	20×64	0.007	very small	60000	8.1×10^{-8}

[a] The brightness of the brightest point source that can be observed in this mode, in units of counts per second. The extended full frame mode is for observations of extended sources only.

[b] The brightness of the brightest point source that can be observed in this mode, in units of $\mathrm{erg\,cm^{-2}s^{-1}}$.

CCDs are in operation. The timing and burst modes are designed to observe very bright or bursting sources. In these two modes, we not only discard photon events from the outer part of the CCDs, we also give up the positional information for the rest of them, to speed up the read out. Please see Table 2.1 for the detailed parameters of the different readout modes.

The energy resolution of the pn CCD is determined mainly by the statistical fluctuations of the ionization process, the charge transfer properties of the CCD and the electronic noise of the readout node. In-flight calibration showed that the energy resolution of the pn camera is between 105 eV and 161 eV depending on the energy, readout mode and position. It is best at the focal point. The quantum efficiency of the pn CCDs is above 0.5 between 0.15 and 15 keV.

The MOS CCDs are slightly different from the pn CCDs. Their quantum efficiency varies from 0.2 to 0.9 in 0.2–10 keV range, slightly worse compared with the pn CCDs. Although there are two MOS cameras, they together collect fewer photon events than the one pn camera due to obstruction by the RGS. The MOS cameras also have similar windowed readout modes as for the pn camera. The faster readout mode should be used for bright sources. They have a time resolution of 2.6 s in the standard readout

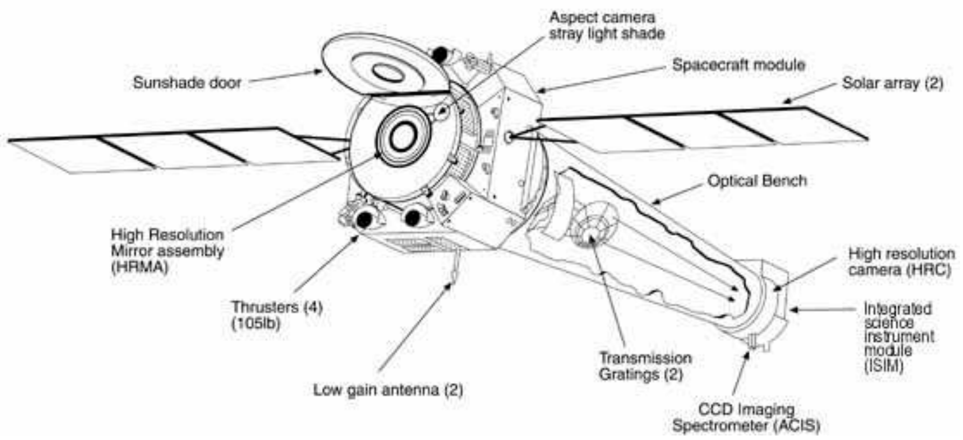

Figure 2.5 A schematic view of the *Chandra* observatory.

`http://chandra.harvard.edu/about/specs.html`

mode, and 0.3 s in the small window mode (100×100 pixels). The angular resolution of the MOS cameras is slightly better than that of the pn. It is $4.5''$ and $6''$ FWHM at 1.5 keV and $4.2''$ and $5.1''$ at 8 keV, respectively. In addition to the choice of modes, the MOS cameras also have four different filters: two thin filters, a medium filter and a thick one. They are designed to filter the low energy radiation from bright stars in the background. The thicker filter should be used when a very bright star is present in the FOV.

Both the pn camera and MOS cameras suffer from some background contamination, the source of which includes the diffuse X-ray background, cosmic rays, electronic noise and highly ionized particle flares. The cosmic rays can be removed by the on-board computer system. The electronic noise only affects a few pixels, so can be removed by flagging the bad pixels. The ion flares are flares of heavy and light ions and low energy protons, which last for minutes to hours. These flares can be removed by excluding periods when they are present.

2.4 The *Chandra* Telescope

The *Chandra* X-ray Observatory (Weisskopf et al., 2002) was launched by NASA on July 23, 1999. It has a 63.5-hr eccentric orbit with a perigee of 16,000 km and an apogee of 133,000 km. The telescope onboard *Chandra* also uses a type I Wolter mirror with mirror cones that distribute in circles with largest diameter of 1.2 m and a focal length of 10 m (see Figure 2.5 for a schematic view of the observatory). *Chandra*'s mirrors are made of glass layers, which were very precisely shaped to achieve angular resolution of $\sim 0\farcs5$, much better than those of the *XMM* mirrors. However, glass is a rather dense material, which made the mirrors much heavier than those of *XMM*. As a result, *Chandra* only has 4 sets of mirrors. Their total unobscured aperture is only 1145 cm^2 (the effective area is 40–600 cm^2 for ACIS-I and 133–277 cm^2 for HRC-I; see below). There are two focal plane instruments on board *Chandra*: the Advanced CCD Imaging Spectrometer (ACIS; Garmire et al. 2003) and the HRC. The ACIS CCDs can simultaneously collect imaging and spectral information of the observed object, and are designed to work in the 0.2–10 keV range. The HRC is made of micro-channel plates. They provide high time resolution (16 ms) images in 0.1–10 keV, but have poorer energy resolution when compared with CCDs. Both ACIS and HRC can be used in conjunction with the HETG or LETG to obtain high resolution spectra from bright point-like sources, but in these cases there will be no spatial resolution and the effective area will be significantly smaller (HETG+ACIS: 28–200 cm^2; LETG+ACIS: 4–200 cm^2; LETG+HRC: 1–25 cm^2). Only one of ACIS and HRC can be switched on and moved into the focal plane position during every observation.

ACIS is composed two CCD arrays (Fig 2.7). The ACIS-I is a 2×2 array of 4 CCDs for imaging observations of extended FOV. The ACIS-S is a 1×6 array of CCDs arranged to serve either imaging or grating observations. Each CCD has 1024×1024 pixels and covers an $8\farcm4 \times 8\farcm4$ FOV; the size of each CCD pixel is $24\times24\,\mu\mathrm{m}^2$, corresponding to $0\farcs492 \times 0\farcs492$ in the FOV, and comparable to the size of the telescope PSF near the centre of the FOV. The PSF of the mirror is much better at the centre of the FOV than it is off-centre. For an on-axis source, 90% of its photons will arrive within a 2–2.5 pixel radius circular region. For an off-axis source, however, the 90% encircling region becomes sometimes as large as 5 pixels in radius, and also deviates

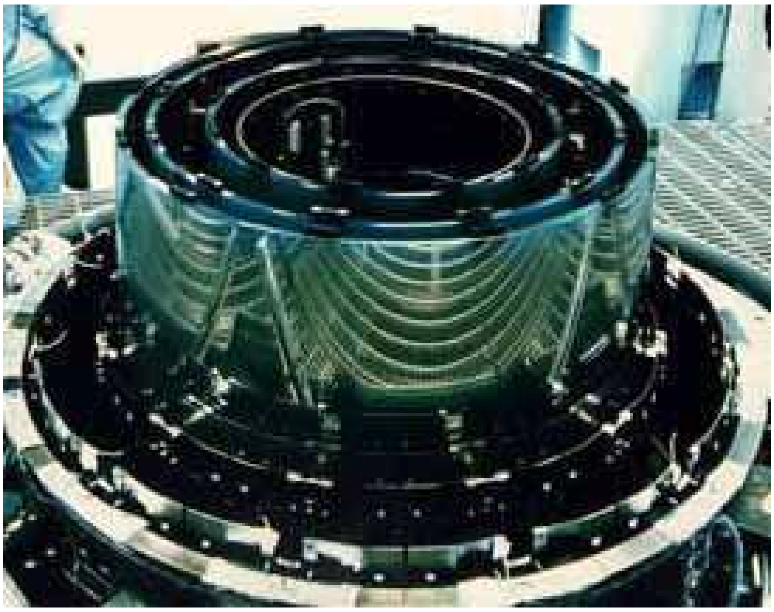

Figure 2.6 The 4 type I Wolter mirrors of the *Chandra* observatory.
`http://chandra.harvard.edu/resources/illustrations/mirrorFab.html`

from a circular shape.

The telescope is designed to dither, following a Lissajous pattern during all observations in order to provide some exposure in the CCD gaps and to smooth out pixel to pixel variations in the response. For ACIS observations, the dither pattern spans $16''$ peak to peak and is slow ($0\farcs1$ per frame), therefore, it does not affect the imaging resolution. In some cases, it is possible to de-convolve the images to better than $0\farcs5$ resolution.

There are two types of ACIS CCD chips: the front illuminated (FI) CCDs and the back illuminated (BI) CCDs. They have slightly different energy responses and background rates. ACIS-I CCDs are all front-illuminated, whereas two of the six ACIS-S CCDs are back-illuminated. The basic working principle of these CCDs is similar to that of the *XMM* CCDs. Currently, the differences between the FI and BI CCDs are mostly in their quantum efficiency and energy resolution. The BI CCDs have better quantum efficiency for lower energy photons ($< 3\,\mathrm{keV}$). However, the FI CCDs have better energy resolution than the BI ones (FI: E/dE =20–50 in 1–6 keV;

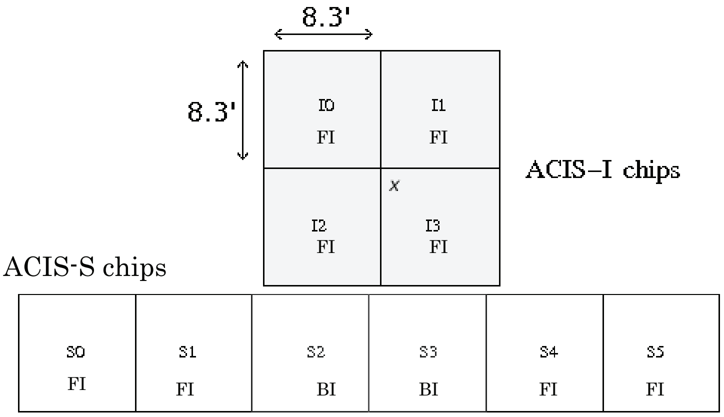

Figure 2.7 The layout of the ACIS CCDs; FI: front illuminated, BI: back illuminated. Figure adopted from `http://cxc.harvard.edu/cal/Acis/`.

BI: E/dE =9–35 in 1–6 keV).

Like the pn and MOS instruments, the ACIS instrument also has several observational modes. A nominal Time Exposure (TE) mode with a 3.2-s frame time is commonly used in imaging observations of faint or extended sources. In order to deal with bright point sources, a subarray mode can be used. Much like the windowed mode of the *XMM* pn and MOS instuments, in the subarray mode, only events from part of the CCD are read out, and the frame time can be reduced accordingly. In our *Chandra* observations of PSR J1718−3718 (Chapter 6), a 1/8 subarray mode was used in order to obtain sufficient time resolution for detecting pulsations. The time resolution can be further improved in the continuous clocking (CC) mode at the expense of one dimension of spatial resolution. In this mode, a 1×1024 pixel image will be produced with 3-ms time resolution. One problem with the CC mode is that with only one a dimensional image, it is hard to remove the background from the source. This is more of a problem when the source is faint or when there are other bright sources in the FOV.

2.5 X-ray Spectroscopy

In this section, I introduce how to analyze spectral data, including how to fit the spectra with models.

Before analysing the spectrum, one must first reduce the raw data collected by the telescope, remove instrumental artifacts and data from bad observation intervals, and then extract the spectrum of the source along with a background spectrum from the cleaned-up data. These are generally done using specific software. For the *XMM* data analysis presented in this thesis, I used the Science Analysis System (SAS)[1] package recommended by the *XMM* science team, along with the most up-to-date (at the time when the work was done) *XMM* calibration files [2]. For the *Chandra* data analysis, I used the `CIAO`[3] software package along with the most up-to-date calibration files in the `CALDB`[4] package. The analysis of *ASCA* and *Suzaku* data are fairly straightforward; the `xselect` tool in the `HEASoft`[5] software package was used along with the necessary calibration files. Most of the data, including raw data and data products such as image and spectrum, are stored in FITS format (flexible image transport system, Wells et al. 1981) files. Details regarding the analyses are provided in the following Chapters.

In the raw data, a detected photon event is usually stored as a row of values including the detector position of the event and the energy channel in which the event was detected. A spectrum file is a filtered subset of the collected data, with a column that stores the number of photons $N(i)$ in every channel of the detector, where i is the channel number. A count rate spectrum $C(i)$ is just $N(i)$ divided by the exposure time t (usually stored in the FITS header). Sometimes the spectrum extracted from the source also contains a significant number of background photons. In this case we need to extract both the source spectrum ($S(i)$) and background spectrum ($B(i)$). The background spectrum is usually extracted from a region close

---

[1] xmm.esac.esa.int/sas/

[2] xmm2.esac.esa.int/external/xmm_sw_cal/calib/index.shtml

[3] cxc.harvard.edu/ciao/index.html

[4] cxc.harvard.edu/caldb

[5] heasarc.gsfc.nasa.gov/docs/software/lheasoft/ftools/xselect/index.html

to the source so that they have virtually the same instrument response. A source spectrum can be calculated as:

$$N(i) = \frac{S(i)}{a_S} - \frac{B(i)}{a_B}\frac{t_S}{t_B}, \tag{2.1}$$

where t_S and t_B are the source and background exposure times, and a_S and a_B are the area of the source and background regions. Sometimes an extra scaling factor must be multiplied to the background part of the equation in order to take into account the detector sensitivity difference between the source and background regions.

The instrument response $R(i, E)$ is proportional to the probability that an incoming photon of energy E is detected in channel i. $R(i, E)$ is a continuous function of E, but the instrument team usually provides a discrete version of it:

$$R(i, j) = \frac{\int_{E_{j-1}}^{E_j} R(i, E)dE}{E_j - E_{j-1}}, \tag{2.2}$$

where E_j is called the energy grid, and $R(i, j)$ is called the response matrix. They are both stored in a FITS response matrix file. For some detectors such as CCDs, the energy response matrix $R(i, j)$ could vary by pixel on the detector.

The effective area of the instrument, especially that of a focus-imaging telescope, $A(E)$, also depends on the source's position on the detector and the size and shape of the source extraction region. In this case, an auxiliary response file that contains a discrete array of the effective area, $A(j)$ is also needed. The response matrix $R(i, j)$ is usually interpolated based on the previously known response of the detector. The effective area $A(j)$ is usually calculated based on the source's detector location and averaged over the extraction region.

The relation between the measured spectrum $C(i)$ $(N(i)/t_S)$ and the source's real spectrum $f(E)$ is:

$$C(i) = \int f(E)R(i, j)A(j)(E_j - E_{j-1})dj. \tag{2.3}$$

As one can see, this an equation of integration; one must deconvolve the right side to get $f(E)$. Unfortunately, this is generally impossible, as the solution is usually non-unique and unstable to small changes in $C(i)$. Therefore, instead of solving the spectrum by force, we can fit the spectrum with a spectral model and see if we can get a statistically acceptable fit. The spectral model $f_{\mathrm{p}}(E)$, which depends on some model parameters p, can be integrated with the same response matrix to generate a predicted spectrum: $C_{\mathrm{p}}(i) = \int f_{\mathrm{p}}(E)R(i,j)A(j)(E_j - E_{j-1})dj$. The most commonly used statistic for such a hypothesis test is the χ^2 test:

$$\chi^2 = \sum [C(i) - C_{\mathrm{p}}(i)]^2/\sigma(i)^2, \tag{2.4}$$

where $\sigma(i)$ is the uncertainty on each $C(i)$. Based on Poisson statistics, for $N(i) > 15$, $\sigma(i) \simeq \sqrt{N(i)}/t_S$.

Much of my work on X-ray spectroscopy introduced in this thesis is about finding the right spectral model and constraining its best-fit parameters. I use the software `xspec`[1] (Arnaud et al., 1992) to perform these tasks.

---

[1] http://heasarc.nasa.gov/docs/xanadu/xspec/

3

The X-ray Afterglow of AXP 1E2259+586's 2002 Outburst

The content of this Chapter is reported in the paper "The Long-term Radiative Evolution of Anomalous X-Ray Pulsar 1E 2259+586 After its 2002 Outburst" published in the *Astrophysical Journal* (Zhu et al., 2008).

3.1 Introduction

As introduced in Section 1.2, 1E 2259+586 was the first AXP to exhibit an SGR-like outburst. The outburst took place on June 18th, 2002. During 1E 2259+586's 2002 outburst, the pulsed and persistent fluxes rose suddenly by a factor of $\geq$20 and decayed on a timescale of months. Coincident with the X-ray brightening, the pulsar suffered a large glitch of fractional frequency change 4×10^{-6} (Kaspi et al., 2003; Woods et al., 2004). In the first few hours of the outburst, the pulsar's pulse profile changed significantly, its pulsed fraction decreased, and its spectrum hardened dramatically. Over 80 short SGR-like bursts from the pulsar were observed at the same time (Gavriil et al., 2004). A near-infrared (K_s) enhancement was also observed during the epoch of the outburst (Kaspi et al., 2003).

Combining *Rossi X-Ray Timing Explorer* (*RXTE*) observations and *XMM* observations of 1E 2259+586 taken during and after the outburst, Woods et al. (2004) found that the decay of 1E 2259+586's unabsorbed flux (mostly inferred from *RXTE* pulsed fluxes) after the outburst was well characterized by two power-law components: a rapid steep decay visible only during the first several hours (< 1 day) of the outburst, and a slower decay of index -0.22 for the next several months. Tam et al. (2004) found that the near-infrared enhancement at late times decayed at the same rate as the slow X-ray decay, although there were no infrared (IR) observations during the first few hours of the outburst.

Other AXPs have also exhibited transient behaviour that could be explained by SGR-like outbursts. AXP XTE J1810−197 is called 'transient' because it was discovered in 2003 when it suddenly became brighter by a factor of 100 (Ibrahim et al., 2004; Gotthelf et al., 2004a). Gotthelf & Halpern (2007) found that the flux of XTE J1810−197 after 2003 followed an exponential decay of timescale 233.5 days. Similarly, the AXP CXOU J164710.2−455216 was found to have brightened by a factor of ∼300 between two *XMM* observations taken 5 days apart in 2006 September (Israel et al., 2007). Candidate AXP AX 1845−0258, was discovered in an observation made in 1993 by *ASCA* (Gotthelf & Vasisht, 1998; Torii et al., 1998). Follow-up observations in 1999 showed that the source's flux was smaller by a factor of ∼10 (Vasisht et al., 2000). Tam et al. (2006) found that AX 1845−0258 remains undetected in *Chandra* observations taken in 2003, with its flux ∼260-430 times fainter than observed in 1993.

The transient AXP phenomena are qualitatively similar to the 1998 August 27 flare of SGR 1900+14, in which the X-ray flux decayed with a power law of index ~ -0.9 (Feroci et al., 2003), and the flux decay of SGR 1627−41 since 1998, which followed a power law of index ~ -0.47 and lasted for ∼800 days (Kouveliotou et al., 2003). However, thus far, the AXP outbursts have been much less energetic than most SGR outbursts. Also, most of the burst energy was released during the afterglows of the AXP outbursts, while for SGR outbursts, the X-ray afterglows have less integrated energy than the burst itself.

With now a handful of AXP and SGR outbursts and subsequent relaxations observed, we can begin to look for correlations between different outburst and relaxation properties in the hope of constraining magnetar physics. For example, SGR outburst recoveries have been modeled as crustal cooling following impulsive heat injection, and in principle can yield constraints on the nature of the crustal matter (Lyubarsky et al., 2002). Alternatively, the AXP events have been interpreted in terms of magnetospheric twisting (Thompson et al., 2002; Beloborodov & Thompson, 2007), whose recovery depends on electrodynamics in the region of the magnetosphere immediately outside the stellar surface. On the other hand, Güver et al. (2007) suggest that AXP recoveries can be modeled with a stationary magnetosphere, with only the surface temperature changing. They argue that their model, which includes the stellar atmosphere, can be used to quantitatively determine the source's magnetic field.

In this Chapter we present a spectral and pulsed flux analysis of ten *XMM* observations of AXP 1E 2259+586 taken between 2002 and 2005, as the source relaxed back toward quiescence following its 2002 outburst. We compare the X-ray flux and spectral evolution of 1E 2259+586 with those of other magnetars, and interpret these results in terms of the magnetar model.

3.2 Observations

3.2.1 XMM-Newton Observations

Ten *XMM* (Section 2.3; Jansen et al. 2001) observations were analyzed for this Chapter. The first five observations of 1E 2259+586 were taken between 2002 and 2003, just prior to and after the 2002 June outburst. Data from these five observations have already been presented in Woods et al. (2004). We re-analyzed these observations using the *XMM* calibrations published on 2007 September 4 (XMM-CCF-REL-239[1]). The later five observations were taken between 2004 and 2005. Most of these observations pointed at 1E 2259+586, with the EPIC pn camera (Strüder et al., 2001) in Small Window Mode. However, three observations were obtained with *XMM* pointing at a portion of the SNR CTB 109's shell and with the pn camera in extended Full Frame Mode. Details about the observational modes, pointing offsets, and exposure times are presented in Table 3.1. The EPIC mos cameras (Turner et al., 2001) were operating in Full window mode with the medium filter in four of the first five observations, the exception being the third, and therefore the observed spectra are highly piled-up. The mos cameras were operated in Small Window Mode with the thick

---

[1] See http://xmm.esac.esa.int/external/xmm_sw_cal/calib/rel_notes/index.shtml

filter (see Section 2.3) in the remaining observations, and hence with lower efficiency than for the pn camera. Nevertheless, we analyzed the mos data and found the resulting fluxes and parameters were quantitatively in agreement with those from pn data, given the current knowledge of cross-calibration uncertainties between the two instruments.[1] In this Chapter we report only the higher quality EPIC pn data.

The data were analyzed with the *XMM* SAS version 7.1.0[2] and the latest calibrations. Strong background flares can sometimes contaminate source events. To exclude possible flares, we extracted light curves from the entire field of view for events having energy > 10 keV. We then examined these light curves for flares. We defined bad time intervals to be when flares occurred, and excluded these intervals for all subsequent analyses. For all the *XMM* observations, we filtered a total of 20 ks of bad time intervals. Then we corrected the event times to the barycenter using the SAS `barycen` tool.

3.2.2 RXTE Observations

AXP 1E 2259+586 has been regularly observed since 1997 with *RXTE* (see Chapter 2; e.g., Gavriil & Kaspi 2002). PCA data were obtained and analysed by my collaborator R. Dib. For completeness, this Section reports her analysis of the *RXTE* data, which were used to monitor the pulsed flux, and frequency evolution of 1E 2259+586 using phase-coherent timing, and to look for bursts and pulse profile changes.

For the purposes of this work 193 observations were analysed. They took place between 2001 April 1 (MJD 52,000) and 2006 September 22 (MJD 54,000): 15 pre-outburst observations, 1 observation during the outburst, and 177 post-outburst observations. All 193 observations with the exception of the two observations immediately following the outburst were taken in `GoodXenonwithPropane` or `GoodXenon` data modes. Both data modes record photon arrival times with 1 μs resolution and bin photon energies into one of 256 channels. To maximize the signal-to-noise ratio,

---

[1] See http://xmm.esac.esa.int/docs/documents/CAL-TN-0018-2-6.pdf, on the current calibration status of the EPIC cameras.

[2] See http://xmm.esac.esa.int/sas/7.1.0/

Table 3.1. *XMM* observation log for 1E 2259+586.

Name	*XMM* Obsid	Date (MJD TDB)	Date (YY-MM-DD)	on-times [a] (ksec)	Off-axis angle (arcmin)	Frequencies [b] (s^{-1})
Obs1[cd]	0057540101	52,296.791	02-01-22	8.5	8.7	0.1432871204(7)
Obs2[c]	0038140101	52,436.413	02-06-11	26.3	2.0	0.143287000(9)
Obs3	0155350301	52,446.446	02-06-21	16.4	2.0	0.14328759(1)
Obs4[d]	0057540201	52,464.368	02-07-09	5.2	10.7	0.14328754(1)
Obs5[d]	0057540301	52,464.602	02-07-09	10.2	10.3	0.14328754(1)
Obs6	0203550301	53,055.596	04-02-20	3.6	1.9	0.143286974(7)
Obs7	0203550601	53,162.655	04-06-06	4.8	2.0	0.143286882(4)
Obs8	0203550401	53,178.634	04-06-22	3.4	2.0	0.143286868(2)
Obs9	0203550501	53,358.014	04-12-19	3.5	2.0	0.143286714(1)
Obs10	0203550701	53,579.970	05-07-28	3.3	1.9	0.143286523(7)

[a] The pn on-times quoted here reflect on-source times after filtering of background flares.

[b] Frequencies are from contemporaneous *RXTE* observations.

[c] Observations taken before the outburst, Modified Julian Date (MJD) 52,443.13 (Woods et al., 2004).

[d] These three observations were taken in extended Full Frame Mode; all the others were taken in Small Window Mode.

only those events from the top xenon layer of each Proportional Counter Unit (PCU) were analyzed. The remaining two observations were in event modes with a time resolution of $\sim$125 μs, a smaller number of energy channels, and no possibility of layer selection. For each of the observations barycentered light curves were created in the 2–10 keV band with 31.25 ms time resolution.

Each of the light curves were then folded using an ephemeris determined iteratively by maintaining phase coherence (see, e.g., Gavriil & Kaspi 2002). The folded profiles were used to calculate the pulsed flux for each observation using both an rms estimator (see, e.g., Woods et al. 2004) and an area estimator after baseline subtraction. The results obtained using the two methods were consistent with each other. Here we only report the area pulsed flux because, while more sensitive to noise, it is the quantity of primary interest.

To calculate the area pulsed flux for a given folded time series, the following equation was used:

$$PF_{area} = \sum_{i=1}^{N}(p_i - p_{min})/N, \tag{3.1}$$

where p_i refers to the count rate in the ith bin, N is the number of phase bins, and p_{min} is the average count rate in the off-pulse phase of the profile, determined by cross-correlating with a high signal-to-noise ratio template, and calculated in the Fourier domain after truncating the Fourier series to six harmonics. Finally, the pulsed flux numbers from each of two consecutive weeks were combined into a single number, with the exception of the burst observation and the two observations that followed it, which remained unbinned. The results are presented in Figure 3.1*a*.

3.3 Analysis and Results

3.3.1 Spectrum Evolution

Our spectral analysis was done using *XMM* EPIC-pn data (see Section 2.3).

Source spectra were extracted from circular regions of $32''.5$ radius around the source center, using the barycentered, filtered event file described in §3.2.1. Back-

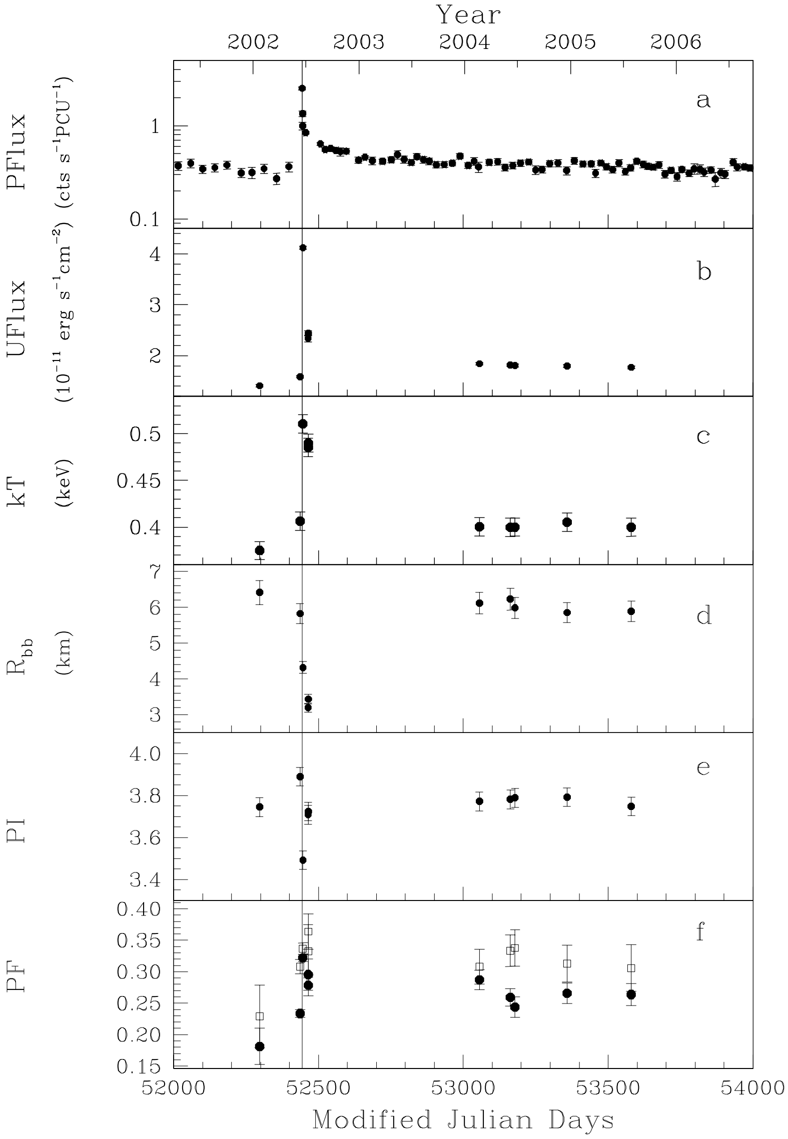

Figure 3.1 Spectral and pulsed fraction evolution of 1E 2259+586 during and following its 2002 outburst. (*a*) 2–10 keV area pulsed flux measured in *RXTE* monitoring observations; (*b*) 2–10 keV unabsorbed phase-averaged flux from *XMM* observations (all lower panels are also from *XMM* observations); (*c*) blackbody temperature (kT), (*d*) blackbody radius; (*e*) photon index; (*f*) 0.1–2 keV area pulsed fraction (*filled circles*) and 2–10 keV area pulsed fraction (*open boxes*). A distance of 3 kpc (Kothes et al., 2002) is assumed to calculate the blackbody radius. The vertical line denotes the 2002 glitch epoch, MJD 52,443.13 (Woods et al., 2004).

ground spectra were extracted from circular regions of $50''$ radius centered $\sim 3'$ away from the source center. For the observations taken in Small Window Mode, we extracted single- and double-photon events and excluded events on or close to a bad pixel using the filter expression "FLAG = 0 && PATTERN <= 4". In the Full Frame Mode observations, the source is highly off-center in the CCD image (Table 3.1), and bad pixels were found close to the source center region. For these observations, the event list was filtered using the selection expression #XMMEA_EP to exclude only photons which fall directly on the bad pixels. However, we did not exclude photon events located adjacent to the bad pixel (which normally would be excluded by the expression FLAG = 0), because when there is a bad pixel close to the center of the source region, the effective area is evaluated more accurately with pixels around the bad ones taken into account by the SAS command `arfgen` (*XMM* help desk 2008, private communication). In order to avoid events that affected multiple pixels, we used only single events (PATTERN= 0) in the Full Frame Mode data. Event lists thus extracted were input to `ftool grppha`, which grouped the events by at least 25 photons per bin. A systematic uncertainty of 2% was also appended to the output spectra using `grppha` in order to characterize the current level of calibration accuracy.[1]

The resultant spectra were fitted in XSPEC 12.3.0[2] with the commonly used photoelectrically absorbed blackbody plus power-law model in the energy range 0.6-12 keV. Because the hydrogen column density N_H is not expected to be variable, we fixed this parameter for all the data sets and performed a joint fit. The goodness of fit is reasonable (see χ^2_ν in Table 3.2). The best-fit N_H is $(1.012 \pm 0.007) \times 10^{22}\,\mathrm{cm}^{-2}$.

This value is consistent with that estimated from fitting individual absorption edges of elements O, Fe, Ne, Mg, and Si in the *XMM* RGS spectra (Durant & van Kerkwijk, 2006). The other parameters were set free to vary and their best-fit values are presented in Table 3.2. The best-fit blackbody temperature, blackbody radius, and power-law index are plotted versus time in Figure 3.1.

---

[1] See http://xmm.esac.esa.int/docs/documents/CAL-TN-0018.pdf, (*EPIC Status of Calibration and Data Analysis)*

[2] See http://heasarc.gsfc.nasa.gov/docs/xanadu/xspec/

Table 3.2. 1E 2259+586's best-fit spectral parameters and pulsed fractions.

Parameter[ab]	Obs1	Obs2	Obs3	Obs4	Obs5	Obs6	Obs7	Obs8	Obs9	Obs10
Blackbody plus power-law model										
N_H (10^{22} cm^{-2})	1.012(7)	1.012(7)	1.012(7)	1.012(7)	1.012(7)	1.012(7)	1.012(7)	1.012(7)	1.012(7)	1.012(7)
kT (keV)	0.37(1)	0.406(2)	0.510(4)	0.48(2)	0.49(1)	0.400(7)	0.400(5)	0.400(7)	0.405(7)	0.400(7)
Γ	3.75(4)	3.89(2)	3.49(2)	3.71(5)	3.72(4)	3.77(3)	3.78(3)	3.79(3)	3.79(3)	3.75(3)
Flux[c]	1.15(2)	1.29(1)	3.45(3)	1.95(5)	2.03(4)	1.51(2)	1.48(2)	1.48(2)	1.47(2)	1.45(2)
Unabs Flux[d]	1.41(3)	1.59(1)	4.12(3)	2.34(7)	2.44(5)	1.84(3)	1.82(2)	1.81(3)	1.80(3)	1.77(3)
PL/BB ratio[e]	1.8(3)	1.2(2)	1.6(2)	2.6(4)	2.1(3)	1.6(2)	1.5(2)	1.7(2)	1.5(2)	1.7(2)
Hardness [f]	0.93(3)	0.94(1)	1.43(1)	1.13(4)	1.15(4)	0.98(2)	0.98(2)	0.97(2)	0.98(2)	0.99(2)
$\chi^2_\nu(\nu)$	1.02(5800)		$(P = 0.12)$[g]							
Double blackbody model										
N_H (10^{22} cm^{-2})	0.568(3)	0.568(3)	0.568(3)	0.568(3)	0.568(3)	0.568(3)	0.568(3)	0.568(3)	0.568(3)	0.568(3)
Cooler kT (keV)	0.362(5)	0.372(2)	0.390(3)	0.330(7)	0.335(5)	0.371(3)	0.380(3)	0.371(3)	0.370(4)	0.371(3)
Hotter kT (keV)	0.77(4)	0.82(1)	0.86(1)	0.74(3)	0.73(2)	0.85(3)	0.94(2)	0.89(3)	0.85(3)	0.86(3)
Flux[c]	1.12(6)	1.27(2)	3.34(4)	1.85(9)	1.93(7)	1.48(4)	1.46(3)	1.44(4)	1.44(4)	1.41(4)
Unabs Flux[d]	1.26(6)	1.42(2)	3.69(4)	2.05(11)	2.15(8)	1.65(5)	1.63(4)	1.62(5)	1.61(5)	1.58(5)
HB/CB ratio[h]	0.8(1)	0.6(1)	1.2(2)	2.1(3)	2.0(3)	0.7(1)	0.53(7)	0.64(9)	0.7(1)	0.7(1)
Hardness [f]	0.91(5)	0.92(1)	1.37(2)	1.07(6)	1.09(4)	0.96(3)	0.95(2)	0.94(3)	0.95(3)	0.96(3)
$\chi^2_\nu(\nu)$	1.11(5800)		$(P = 4.6 \times 10^{-9})$[g]							
Pulsed fractions										
PF(0.1–2 keV)[i]	0.18(3)	0.234(6)	0.322(6)	0.30(2)	0.28(2)	0.29(2)	0.26(1)	0.24(2)	0.27(2)	0.26(2)
PF(2–10 keV)[i]	0.23(5)	0.30(1)	0.339(9)	0.33(4)	0.36(3)	0.30(3)	0.33(2)	0.34(3)	0.31(2)	0.29(3)

[a] Numbers in parentheses indicate the 1σ uncertainty in the least significant digit. Note that these uncertainties reflect the 1σ error for a reduced χ^2 of unity.

[b] Best-fit parameters from a joint fit to all data sets. N_H in all data sets was set to be the same; other parameters were allowed to vary from observation to observation.

[c] (10^{-11} ergs s^{-1}cm^{-2}). Observed flux from both spectral components in the range 2–10 keV.

[d] (10^{-11} ergs s^{-1}cm^{-2}). Unabsorbed flux from both spectral components in the range 2–10 keV.

[e] The ratio of power-law flux to blackbody flux in the 2–10 keV band (corrected for absorption).

[f] Spectral hardness defined as the ratio of 2–10 keV absorbed flux to 0.1–2 keV absorbed flux.

[g] The probability for the χ^2_ν to be higher than that was observed, assuming the model is correct.

[h] The ratio of hot blackbody flux to cool blackbody flux in the 2–10 keV band (corrected for absorption).

[i] The area pulsed fractions.

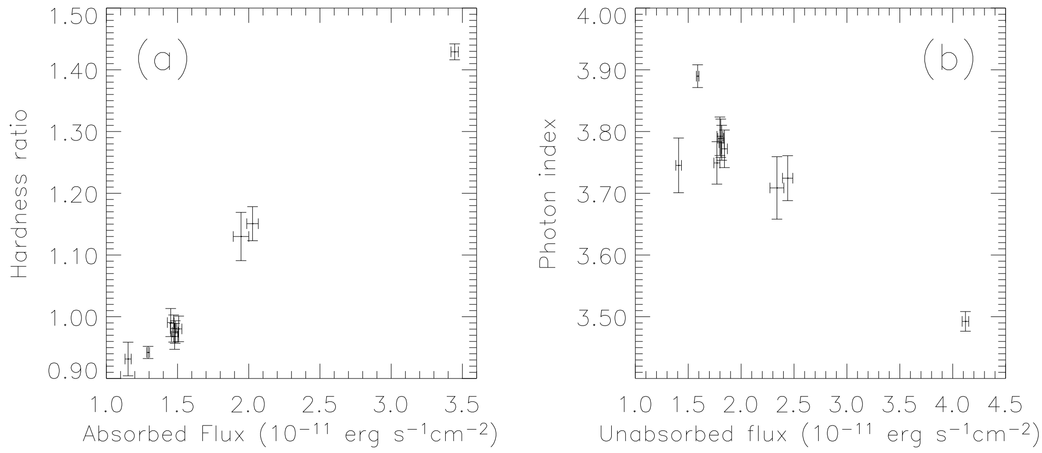

Figure 3.2 (*a*) Hardness vs. absorbed flux. Hardness ratio is defined as the ratio of 2–10 to 0.1–2 keV absorbed flux. (*b*) Photon index vs. 2–10 keV unabsorbed flux.

In order to look for correlations between spectral hardness and flux as observed in other AXPs (Rea et al., 2005; Campana et al., 2007; Tam et al., 2008; Gonzalez et al., 2010), we have looked for a correlation between hardness ratio and observed flux. We define the hardness ratio to be the ratio of 2–10 keV absorbed flux to 0.1–2 keV absorbed flux. We find the hardness ratio to be strongly correlated with the 2–10 keV absorbed flux (as shown in Fig. 3.2*a*) in our observations. An anti-correlation between photon index and 2–10 keV unabsorbed flux is also seen, but has more scatter (as shown in Fig. 3.2*b*). This is likely because the photon index is not a perfect measure of spectral hardness, as it can be strongly influenced by the spectral fit at the low end of the band.

3.3.2 Pulsed Fractions

We folded the 0.1–2 and 2–10 keV light curves of each *XMM* observation at the pulsar's period, determined using an ephemeris derived by phase coherent timing, from *RXTE* monitoring (Table 3.1; see Dib et al. 2007 for details). Each pulse profile was constructed by folding the photons into 32 phase bins. We measured area pulsed flux of the *XMM* as for the *RXTE* data (see Equ. 3.1), except that we used eight

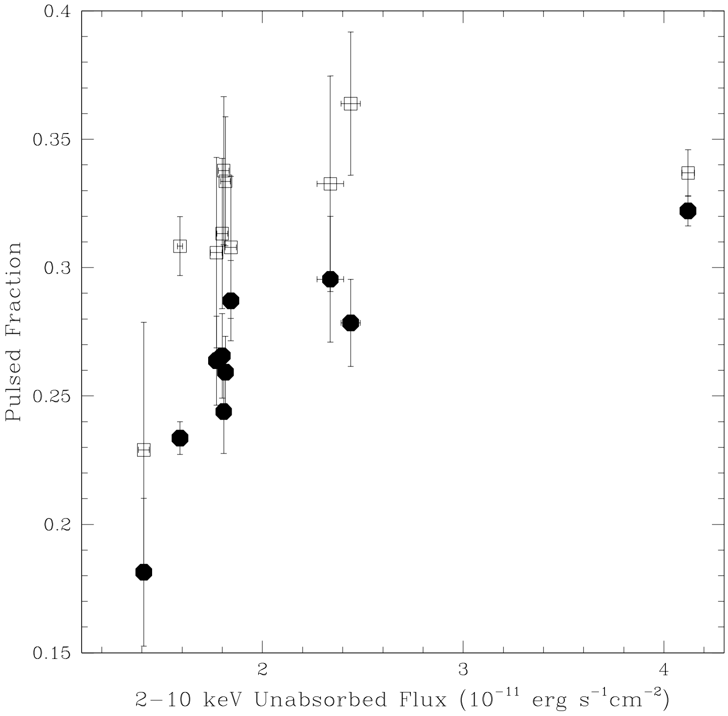

Figure 3.3 The 2–10 keV area pulsed fraction (*open boxes*) vs. 2–10 keV unabsorbed flux ; 0.1–2 keV area pulsed fraction (*filled circles*) vs. 2–10 keV unabsorbed flux.

harmonics instead of six when smoothing the light curves.

The measured area pulsed fractions are plotted in Figure 3.1*f*. A possible correlation between the 0.1–2 keV area pulsed fraction and the 2–10 keV unabsorbed flux is seen (Fig. 3.3, *filled circles*). A similar correlation was also found between the 0.1–2 keV area pulsed fraction and the 0.1–2 keV absorbed flux. However, the correlation between 2–10 keV pulsed fraction and flux is not significant (Fig. 3.3, *open boxes*).

We also measured the rms pulsed fraction from the profiles to compare with the area pulsed fraction results. The 2–10 keV rms pulsed fractions are consistent with being constant, while the 0.1–2 keV rms pulsed fractions have some variance, but no significant trend or correlation with other parameters. The area and rms pulsed fractions are different by a factor that depends on the shape of the profile; as the pulse profile of 1E 2259+586 did change temporarily after the outburst (from a simple double peaked profile to triple peaked; Kaspi et al., 2003; Woods et al., 2004),

Table 3.3. Best-fit parameters for the 1E 2259+586 flux decay

Power law decay[a]	$F_q (10^{-11} \mathrm{ergs\,s^{-1}cm^{-2}})$	$F_b (10^{-11} \mathrm{ergs\,s^{-1}cm^{-2}})$	α	χ^2	χ^2/ν
XMM UF (BB+PL) [b]	(1.75 ± 0.02)	(5.40 ± 0.21)	-0.69 ± 0.03	3.31	0.66
XMM UF (BB+BB) [c]	(1.58 ± 0.01)	(5.07 ± 0.22)	-0.73 ± 0.04	1.22	0.24
RXTE PF [d]	(0.14 ± 0.06) cts $\mathrm{s^{-1}PCU^{-1}}$	(1.4 ± 0.1) cts $\mathrm{s^{-1}PCU^{-1}}$	-0.27 ± 0.05	81.3	1.18
Exponential decay[e]	$F_q (10^{-11} \mathrm{ergs\,s^{-1}cm^{-2}})$	$F_p (10^{-11} \mathrm{ergs\,s^{-1}cm^{-2}})$	τ (days)	χ^2	χ^2/ν
XMM UF (BB+PL) [b]	(1.81 ± 0.01)	(2.97 ± 0.06)	13.3 ± 0.7	5.39	1.08
XMM UF (BB+BB) [c]	(1.62 ± 0.01)	(2.69 ± 0.05)	12.7 ± 0.7	1.737	0.35
RXTE PF [d]	(0.362 ± 0.005) cts $\mathrm{s^{-1}PCU^{-1}}$	(0.46 ± 0.03) cts $\mathrm{s^{-1}PCU^{-1}}$	134 ± 15	113.5	1.65

[a] Power law decay model defined as $F(t) = F_b((t - t_g)/(1 \text{ day}))^\alpha + F_q$, where $F(t)$ is unabsorbed flux, F_q is the quiescent flux, α is the power-law index and t_g is the glitch epoch MJD 52,443.13.

[b] *XMM* unabsorbed flux decay measured using a blackbody plus power-law spectral model.

[c] *XMM* unabsorbed flux decay measured using a double-blackbody spectral model.

[d] *RXTE* area pulsed flux in units of cts $\mathrm{s^{-1}PCU^{-1}}$.

[e] Exponential decay model, defined as $F(t) = F_p e^{-(t-t_g)/\tau} + F_q$, where $F(t)$ is unabsorbed flux, F_p is the peak flux, F_q is the quiescent flux, τ is the decay timescale and t_g is the glitch epoch MJD 52,443.13.

the different result is not surprising.

3.3.3 Flux Evolution

We fit the unabsorbed fluxes measured in our *XMM* observations after the outburst with a power law plus constant decay model, $F(t) = F_b[(t - t_g)/(1 \text{ day})]^\alpha + F_q$, where $F(t)$ denotes the unabsorbed flux, F_b is the unabsorbed source flux one day after the onset of the outburst, F_q is the quiescent flux and t_g marks the glitch epoch MJD 52,443.13 (Woods et al., 2004). A good fit of $\chi^2_\nu(\nu) = 0.66(5)$ (Fig. 3.4, *dashed line*) was found. The best-fit power-law index $\alpha = -0.69 \pm 0.03$ (Table 3.3). The quiescent flux level we found from this power-law fit is $(1.75 \pm 0.02) \times 10^{-11}\,\mathrm{ergs\,s^{-1}cm^{-2}}$, considerably higher than that measured one week before the outburst [$(1.59 \pm 0.01) \times 10^{-11}\,\mathrm{ergs\,s^{-1}cm^{-2}}$; Table 3.2]. We also fit the *XMM* unabsorbed fluxes with an exponential decay plus quiescent level model, $F(t) = F_p e^{-(t-t_g)/\tau} + F_q$, where $F(t)$ is unabsorbed flux, F_p is the peak flux, F_q is the quiescent flux, τ is the decay timescale and t_g marks the glitch epoch. The fit is acceptable, with $\chi^2_\nu(\nu)$ of 1.08(5). The best-fit decay timescale τ is 13.3 ± 0.7 days. Best-fit flux decay parameters are presented in Table 3.3.

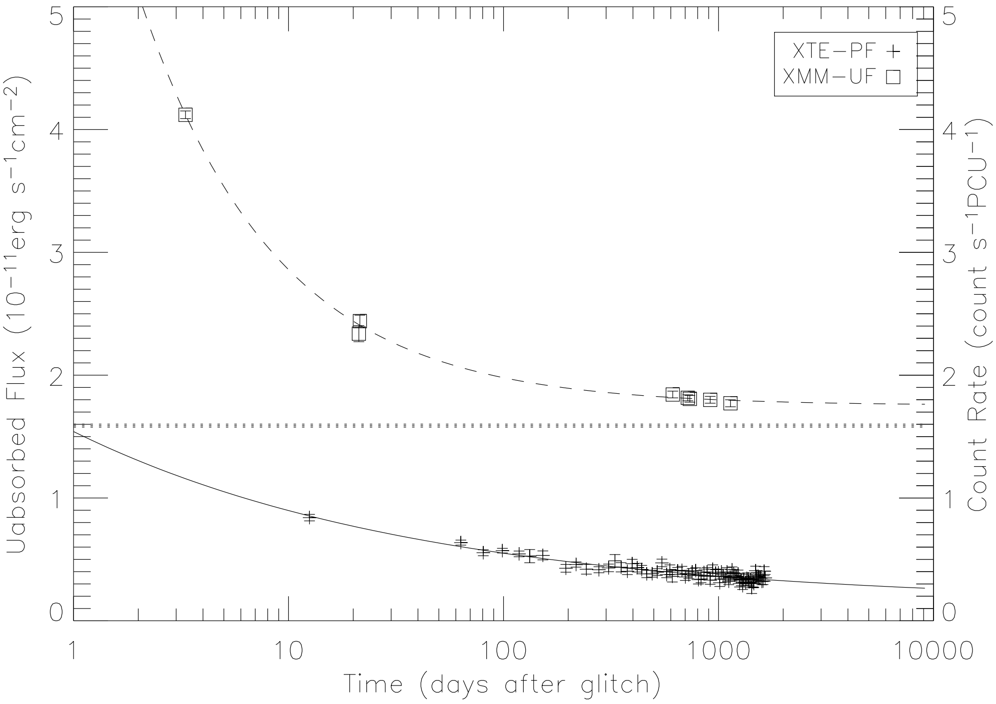

Figure 3.4 Evolution of 1E 2259+586's 2–10 keV unabsorbed phase-averaged flux (*squares*) measured from *XMM* observations and 2–10 keV area pulsed flux (*cross*) from *RXTE* observations following its 2002 outburst. *XMM* unabsorbed fluxes are in units of 10^{-11}ergs s^{-1}cm^{-2}. *RXTE* area pulsed fluxes are in units of count s^{-1}PCU^{-1}. The time axis is relative to the estimated glitch epoch (MJD 52,443.13). The solid line is the power law plus constant model fit to the *RXTE* area pulsed fluxes. The dashed line is a fit of the same model, although having different best-fit parameters, to the *XMM* fluxes. See Table 3.3 for the best-fit parameters. The dotted line is the flux level in 10^{-11}ergs s^{-1}cm^{-2} observed with *XMM* one week before the outburst. The uncertainty on this pre-outburst flux is approximately the width of the line.

We also fit power-law and exponential models to the area pulsed flux of 1E 2259+586 measured by *RXTE* from 12 to 1649 days after the glitch. A power-law model fits the data much better than the exponential model [$\chi^2_\nu(\nu) = 1.18(69)$ for the power-law model, $\chi^2_\nu(\nu) = 1.65(69)$ for the exponential decay model; Table 3.3], which is evidence against the latter. The best-fit exponential decay timescale for *RXTE* data is 134 ± 15 days, an order of magnitude different from the ~ 13 day timescale found for the *XMM* data.

The best-fit power law plus constant model for the evolution of the *RXTE* pulsed fluxes is different from that of the *XMM* total fluxes. This suggests that the 2–10 keV pulsed fractions were varying. In principle, we can check this with the pulsed fraction measurements made with *XMM* (see § 3.3.2). Given the uncertainties on the *XMM* 2–10 keV pulsed fractions (Table 3.2), as well as those of the best-fit evolution models (Table 3.3), we find that the two are in agreement.

Gotthelf & Halpern (2007) fit the spectrum of XTE J1810−197 using a double-blackbody model when studying that source's relaxation following its outburst. In order to compare the spectrum and evolution of 1E 2259+586 to that of XTE J1810−197, we also fit a photoelectrically absorbed double-blackbody model to 1E 2259+586's spectra jointly. A double-blackbody model does not fit the spectra as well as the blackbody plus power-law model (see Table 3.2 for details). The best-fit N_H for the double-blackbody model [$(0.568 \pm 0.003) \times 10^{22}\,\mathrm{cm}^{-2}$] is smaller than that from our blackbody plus power-law fit and is not consistent with the value measured model independently from RGS spectra [$(1.12 \pm 0.33) \times 10^{22}\,\mathrm{cm}^{-2}$; Durant & van Kerkwijk, 2006], but is consistent with the best-fit N_H [$(0.5\text{-}0.7) \times 10^{22}\,\mathrm{cm}^{-2}$] of CTB 109 measured by Sasaki et al. (2004).

Unabsorbed fluxes obtained using the double-blackbody spectral model can also be fitted to a power law decay or an exponential decay model. The best-fit power-law index is -0.73 ± 0.04, and the best-fit exponential timescale is 12.7 ± 0.7 days (Table 3.3), consistent with what we obtained using the blackbody plus power-law spectral model. This indicates that our results for the decay parameters are independent of the choice of spectral model. In the analysis of XTE J1810−197 by Gotthelf & Halpern (2007), they found that both of the two-blackbody components' flux followed an exponential decay after XTE J1810−197's 2003 outburst. However, we find that the flux of 1E 2259+586's soft blackbody component measured from our fourth and fifth observations (only ~21 days after the outburst and glitch) were lower than that measured for the last five observations (see Table 3.2 for details). This flux variation of the soft blackbody component therefore cannot be well fitted with an exponential or power-law decay model. The temperatures of both the hotter and cooler components were also lower in the fourth and fifth observations than in the last five observations. The non-monotonic variation of the soft blackbody flux and the two components' temperature are different from what was observed by Gotthelf & Halpern (2007) and suggest that the double-blackbody model is not a reasonable representation of the spectrum of 1E 2259+586. On the other hand, the spectral evolution from the blackbody plus power-law spectral fit looks more reasonable. Using this spectral model, the blackbody radius in the first post-outburst observation was small compared to that of the pre-outburst observations and was even smaller in the second and third post-outburst observations (Fig. 3.1*d*), suggesting that one or more hot spots formed after the outburst and were fading away in the next few months. In the last five observations, the blackbody radius was as large as the pre-outburst value, suggesting that the putative hot spots had completely faded away and the thermal radiation then mostly came from the bulk surface of the neutron star as it did before outburst. Perhaps a more realistic spectral model such as that of Güver et al. (2007, 2008b) could describe the spectral evolution of 1E 2259+586 better, but such an analysis is outside the scope of this thesis.

Based on *RXTE* observations, Woods et al. (2004) found that the decay of 1E 2259+586's 2002 outburst consisted of two parts: a steeper power-law decay in the first few hours, and a slower power-law decay afterwards. They also found that the total energy released (2–10 keV) in the slower decay was 2.1×10^{41} ergs, which is much larger than the total energy (2–60 keV) released in the bursts (6×10^{37}ergs; Gavriil et al., 2004).

We also studied the slower decay, by fitting a power law plus constant model, instead of the simple power-law model used by Woods et al. (2004). The total released energy, according to our best-fit model, is roughly consistent with that calculated by Woods et al. (2004): we find $\simeq 3 \times 10^{41}$ ergs (2–10 keV), assuming that the outburst will be over in 10000 days. However, based on our best-fit exponential model, the total energy released was somewhat smaller, $\simeq (3-4) \times 10^{40}$ ergs (2–10 keV).

3.4 Discussion

Here we discuss the properties of this recovery, compare them with those of other magnetar outbursts, and consider how they constrain the magnetar model.

3.4.1 Return To "Quiescence"

In our 2004 and 2005 *XMM* observations, the source's temperature and unabsorbed fluxes were still higher than the pre-outburst value (Fig. 3.1). This suggests that the source was not fully back to the pre-outburst flux level. Our power-law fit to the flux decay shows that the after-outburst quiescent flux level is $(1.75 \pm 0.02) \times 10^{-11}\,\mathrm{ergs, s^{-1} cm^{-2}}$, which is significantly higher than the pre-outburst value $[(1.59 \pm 0.01) \times 10^{-11}\,\mathrm{ergs\,s^{-1} cm^{-2}}$; Table 3.3]. Either the 2005 flux had still not returned to its quiescent level, or perhaps it had returned to quiescence but the flux just before the event was unusually low. Also possible is that this (and other) AXPs do not have well-defined constant quiescent fluxes, but have long-term flux variations. Indeed, there is evidence for some X-ray flux variability in 1E 2259+586 over the years since its discovery in 1981 (Baykal & Swank, 1996). Other AXPs also show variability on a variety of timescales (see Kaspi, 2007 for a review).

3.4.2 Comparison with Other Magnetar Recoveries

It is useful to compare the behaviour observed from 1E 2259+586 with that of other magnetars. SGR 1900+14's flux was found to follow a power law of index $-0.713 \pm$

0.025 after its 1998 August 27 flare (Woods et al., 2001).[1] This has been interpreted as the cooling of the magnetar outer crust following a sudden release of magnetic energy (Lyubarsky et al., 2002). This model predicts a power-law decay of index $\sim -2/3$. The flux of SGR 1627−41 was found to decay following a power law of index ~ -0.47 since its 1998 source activation. Approximately 800 days after the source activation, SGR 1627−41's flux suddenly declined by a factor of 10. This behaviour is also well fitted by the crust cooling model, although with some fine tuning (Kouveliotou et al., 2003). We fit the *XMM* 2–10 keV unabsorbed fluxes of 1E 2259+586 with a power law plus constant model, and found the best-fit power-law index to be -0.69 ± 0.03, close to that of SGR 1900+14, and that predicted by the model. This suggests that the 1E 2259+586 outburst afterglow may also be explained by the diffusion of heat in the outer crust.

The transient AXP XTE J1810−197 exhibited an outburst in 2003. Ibrahim et al. (2004) found that the afterglow of the XTE J1810−197 outburst as observed by *RXTE* could be described by a power-law decay model ($F \propto t^{-\beta}$) with $\beta = 0.45{-}0.73$. This is similar to the behaviour of 1E 2259+586 and other SGRs. However, Gotthelf & Halpern (2007) found that, with more observations taken by *Chandra* from 2003 to 2006, the afterglow of the XTE J1810−197 outburst actually followed an exponential decay of timescale 233.5 days. As we have shown in this Chapter, the pulsed and unabsorbed X-ray flux decay of 1E 2259+586 favors the power-law decay model over the exponential decay. Perhaps the physical processes involved in the 2003 outburst of XTE J1810−197 were different from those in 2002 outburst of 1E 2259+586.

3.4.3 Twisted Magnetosphere Model

Thompson et al. (2002) reported that, if there exists a global twist of the magneto-

---

[1] Later the afterglow of the SGR 1900+14 August 27 flare was fitted with a power law plus constant model instead of the single power-law model used by Woods et al. (2001), and a decay index of ~ 0.9 was obtained (Feroci et al., 2003).

sphere, the decay timescale τ of this twist would be

$$\tau = 40\Delta\phi^2 \left(\frac{L_X}{10^{35}\mathrm{ergs\,s^{-1}}}\right)^{-1} \left(\frac{B_{\mathrm{pole}}}{10^{14}\mathrm{G}}\right)^{2} \left(\frac{R_{\mathrm{NS}}}{10\mathrm{km}}\right)^{3} \mathrm{yr}, \tag{3.2}$$

where L_X is the pulsar's X-ray luminosity, B_{pole} is the pulsar's magnetic field strength, R_{NS} is the radius of the star, and $\Delta\phi$ is the twist angle. Woods et al. (2004) argued that, for 1E 2259+586, the twist angle $\Delta\phi$ should be $\sim 10^{-2}$ rad. Thus, the predicted twist relaxation timescale of 1E 2259+586 is several hours, which is consistent with the timescale of the steeper flux decay observed at the beginning of the afterglow.

However, Beloborodov & Thompson (2007) have shown more recently that this decay timescale is actually expected to be much larger than equation (3.2) suggests. This is because, in their model, the self-induction of the twisted portion of the magnetosphere accelerates particles from the stellar surface and initiates avalanches of pair creation which forms the corona. This corona persists in dynamic equilibrium, maintaining the electric current, as long as dissipation permits. The relevant timescale in this picture for the decay of a sudden twist is given by

$$\tau \simeq 0.3 \left(\frac{L_X}{10^{35}\mathrm{ergs\,s^{-1}}}\right) \left(\frac{e\Phi_e}{\mathrm{GeV}}\right)^{-2} \left(\frac{R_{\mathrm{NS}}}{10\mathrm{km}}\right) \mathrm{yr}, \tag{3.3}$$

where L_X is the peak X-ray luminosity and $e\Phi_e$ is the voltage along the twisted magnetic field lines and should nearly universally be ~1 GeV (see Beloborodov & Thompson, 2007). For 1E 2259+586, we find $\tau \simeq 1.2$ yr, given the peak luminosity $L_X \sim 4 \times 10^{35}(d/3\ \mathrm{kpc})$ ergs s^{-1}. Thus, the longer observed decay after the initial steep decline may indeed correspond to the untwisting of a coronal flux tube in the Beloborodov & Thompson (2007) picture, although the predicted timescale is somewhat smaller than the observed time to return to quiescence. We note that the Beloborodov & Thompson (2007) model predicts a linear flux decline, in contrast to what we have observed for 1E 2259+586 and what has been observed for XTE J1810−197 (Gotthelf & Halpern, 2007). Moreover, in the ~5 yr of *RXTE* monitoring of 1E 2259+586 prior to its 2002 outburst (Gavriil & Kaspi, 2002), its pulsed X-ray luminosity in the 2–10 keV band was roughly constant at $\sim 2 \times 10^{34}$ ergs s^{-1}. This also is puzzling given the Beloborodov & Thompson (2007) prediction that if the time between large-scale events is longer than the decay time from the previous event, the magnetar should enter a quiescent state in which the observed luminosity is dominated by the surface blackbody emission. Why should the "quiescent" blackbody emission from 1E 2259+586 be a full order of magnitude larger than that from XTE J1810−197, especially given the latter's much larger inferred magnetic field (1.7×10^{14} versus 6×10^{13} G)? This disparity in "quiescent," steady luminosities is even larger when considering AXP 1E 1841−045, which has an apparently steady 2–10 keV luminosity of 1.4×10^{35} ergs s^{-1}, and comparing with probable AXP AX 1845−0258, which has quiescent luminosity approximately 2 orders of magnitude smaller (Tam et al., 2006). Distance uncertainties may contribute but not on a scale that can significantly alleviate this problem. This remains an interesting puzzle in magnetar physics.

The twisted magnetosphere or flux tube models generically predict that the flux and spectral hardness of magnetars in outburst should be roughly correlated due to increased scattering optical depth when the twist is larger. However, a similar prediction for a flux/hardness correlation was made by Özel & Guver (2007) in their thermally emitting magnetar model, using a simple prescription for the magnetosphere and scattering geometry, with the latter stationary, i.e. invoking no variable magnetospheric twists. Güver et al. (2007) found that their model could reproduce the existing data for XTE J1810−197. We note that hardness-intensity correlations have now been observed for RXS J170849.0−400910 (Campana et al., 2007), 1E 1048.1−5937 (Tam et al., 2008), and as we report, in our 1E 2259+586 *XMM* observations. It would be interesting to apply the analysis of Özel & Guver (2007) to these data, but it is outside the scope of this thesis.

3.4.4 Other Observed Recovery Properties

The fact that the rms and area pulsed fractions remained largely constant while the blackbody radius (in the blackbody plus power-law model) changed by a factor of ~2 (Fig. 3.1) is worth considering, if the empirical blackbody plus power-law spectrum model somehow resembles the real radiation mechanism. Pulsed fraction should generally decrease when the thermally radiating region on the star grows, provided that this region is not very small compared to the entire surface. Any realistic spectral model which takes radiative transfer in the atmosphere and scattering through the magnetosphere into account should be able to reproduce the observation in this regard as well.

A clear anti-correlation between 1E 1048.1−5937 's pulsed fraction and unabsorbed flux has been observed (Tiengo et al., 2005; Gavriil et al., 2006; Tam et al., 2008). However, we found no such correlation in the 2–10 keV band for 1E 2259+586. On the contrary, its 0.1–2 keV area pulsed fractions seem to be correlated with both 0.1–2 and 2–10 keV unabsorbed fluxes (see Fig. 3.3). Gotthelf & Halpern (2007) found that XTE J1810−197 's pulsed fraction measured between 2003 and 2006 after its outburst decreased with the decay of its flux, i.e. XTE J1810−197 's pulsed fraction is also correlated with flux. Thus, the striking anti-correlation between pulsed fraction and flux observed from 1E 1048.1−5937 is clearly not universal.

Finally, we note that the near-infrared flux decay of 1E 2259+586 as observed by Gemini Observatory, was found to follow a power law of index $-0.75^{+0.22}_{-0.33}$ when fitted to a power law plus constant model (Tam et al., 2004). This decay index is close to what we found for the X-ray flux decay, thus confirming the reported correlation between near-IR and X-ray fluxes post-outburst.[1] Tam et al. (2008) and Wang et al. (2008) showed that the near-IR flux of 1E 1048.1−5937 does show correlation with X-rays at times of outbursts. However, Camilo et al. (2007b) show that the near-IR flux variation of XTE J1810−197 is not simply correlated with X-ray flux nor even monotonic post-outburst. Thus, the AXP picture with regard to near-IR variability is not yet fully clear.

---

[1] The −0.22 X-ray decay index reported by Woods et al. (2004) and the −0.21 near-infrared flux decay index reported by Tam et al. (2004) were obtained from a simple power-law fitting, i.e. with no quiescent level included in the fit.

3.5 Summary

In this Chapter, we present the analysis of five *XMM* observations of the AXP 1E 2259+586 taken in 2004 and 2005 during its relaxation following its 2002 outburst. We compare these data with those of five previous *XMM* observations taken in 2002 and 2003, and find that the observed flux decay is well described by a power law of index -0.69 ± 0.03, similar to what was found from the X-ray afterglow of some other SGRs (see Section 1.2.2). As of mid-2005, the source may still have been brighter than pre-outburst, and was certainly hotter. This result suggests that the decay of the 2002 outburst of 1E 2259+586 may be the result of a sudden release of magnetic energy in the outer crust of the magnetar (Lyubarsky et al., 2002). However, we could not rule out that the X-ray afterglow was caused by the slow relaxation of the magnetic twist as suggested in the twisted magnetosphere model of magnetars (Thompson et al., 2002). A strong correlation between hardness and flux was found, as seen in other AXPs (Section 1.2.2). This is qualitatively consistent with the prediction the twisted magnetosphere model (Thompson et al., 2002) in which both the spectral hardness and total flux increase as the twist increase. However, such a correlation may also be explained by a thermally emitting magnetar model (Özel & Guver, 2007), in which the magnetic field twist is assumed to be constant.

4

Searching for X-ray Variability in the Glitching AXP 1E 1841−045

The content of this Chapter is reported in the paper "Searching for X-ray variability in the Glitching AXP 1E 1841−045" published in the *Astrophysical Journal* (Zhu & Kaspi, 2010).

4.1 Introduction

As discussed in Section 1.2, AXPs are known to be very variable at X-ray energies. Their fluxes and spectra vary significantly on a variety of different time scales, from a few milliseconds (e.g. Gavriil et al. 2002), to several years (Dib et al., 2007). They are also known to be prolific glitchers, and include some of the most active glitchers known in the neutron-star population (Dib et al., 2008b). One of the largest glitches seen so far, from AXP 1E 2259+586, was accompanied by major radiative changes, including bursts and a factor of ∼20 pulsed and persistent flux increase (Kaspi et al., 2003; Woods et al., 2004). Dib et al. (2009) showed that glitches in AXP 1E 1048.1−5937 were also accompanied with radiative enhancements. Such events are thought to be the result of sudden yielding of the neutron-star crust due to internal stresses caused by the decay of the magnetar-strength field. The restructuring results in changes to the stellar interior – as evidenced by the glitch – and to the stellar exterior – as evidenced by the dramatic radiative changes. Observations of such AXP outbursts are a potentially powerful probe of the physics of magnetars (e.g. Eichler & Shaisultanov, 2010).

Links between the X-ray variability and glitches of AXP RXS J170849.0−400910 have also been reported (Rea et al., 2005; Campana et al., 2007; Israel et al., 2007;

Götz et al., 2007). These authors suggest the existence of a general correlation between magnetars' flux and glitch epochs. Specifically, Götz et al. (2007) reported ∼40% flux changes in RXS J170849.0−400910 based on eight observations made over the course of ∼9 yr, during which they report four glitches. If correct, this suggests that glitches are usually, and possibly always, accompanied with radiative changes. However, the sparsity of observing epochs compared to the number of glitches for this AXP thus far is problematic in proving the variability is glitch-correlated. Additionally, no comparable pulsed flux changes were observed in the same time span, during which such measurements were available regularly on a monthly basis (Dib et al., 2008b). This apparent conflict could, however, be explained if the pulsed fraction were precisely anti-correlated with flux. An anti-correlation between pulsed fraction and flux has been seen in AXP 1E 1048.1−5937 (Tiengo et al., 2005; Tam et al., 2008), although not to a degree that render pulsed flux variations absent.

Here we investigate the hypothesis that AXP glitches are generically accompanied by radiative changes by considering AXP 1E 1841−045 in SNR Kes 73, one of the most frequent glitchers among AXPs. From *RXTE* monitoring, we know that 1E 1841−045 has had three glitches between 1999 and 2008 (Dib et al., 2008b). The glitches occurred on 2002 July 9, 2003 December 24, and 2006 March 29, and had $\Delta\nu/\nu$ of 5.63×10^{-6}, 2.45×10^{-6} and 1.39×10^{-7}, respectively, and were not accompanied by any X-ray pulsed flux changes. If, as seen in 1E 2259+586 and 1E 1048.1−5937 and reported for RXS J170849.0−400910 , glitches are generically accompanied by radiative changes, and, if as for RXS J170849.0−400910 , such radiative changes are not necessarily apparent in the pulsed flux data, it is possible that the phase-averaged flux (unavailable from *RXTE* monitoring) varies in concert with glitches in 1E 1841−045 . We investigate this possibility here. Also worth noting is that Gotthelf et al. (1999) studied the timing of AXP 1E 1841−045 using archival *GINGA*, *ASCA* , *ROSAT* and *RXTE* data taken between 1993 and 1999 and found no glitches with $\Delta\nu/\nu > 5\times10^{-6}$.

In this Chapter, we report on our analysis of archival X-ray data for 1E 1841−045 collected by *ASCA, Chandra, XMM* and *Suzaku* during the past 17 years, including two observations that were made fortuitously very closely following glitches. We have looked for correlations between the AXP's flux variability and glitch epochs. In Section 4.2 we describe the observations and data reduction process. In section 4.3 we describe our spectral analysis and AXP flux extraction method. Our results and conclusions are discussed in Section 4.4.

4.2 Observations

For this study, we searched online X-ray archives for all existing observations of the Kes 73 field. We found a total of eleven observations from four different focussing X-ray observatories (listed in Table 4.1). We do not include in our analysis the many *RXTE* observations, as due to its non-focussing nature, these provide only pulsed flux measurements, and are already published (Dib et al., 2008b). Next we report on our analysis of the eleven focussing-telescope observations.

4.2.1 *ASCA* Observations

Seven *ASCA* (Tanaka et al. 1994; Section 2.1) observations of the AXP 1E 1841−045 and the SNR Kes 73 were taken between 1993 and 1999 (see Table 4.1). Our analysis began with the screened data from the two Gas Imaging Spectrometers (GISs, Burke et al. 1994), which were filtered with the standard revision 2 screening criteria. Given the angular resolution of the GISs, the SNR ($\sim 2'$) was unresolvable in the images, therefore the spectra we extracted from the GISs contain photons from both the AXP and the SNR. Using the `ftool xselect`[1], we extracted spectra from source regions of $9'.8$ radius (a region large enough to encircle the extended emission from AXP 1E 1841−045 and Kes 73) and background spectra from regions of radius $\sim 5'$, away from the source region for all the *ASCA* GIS observations. The GIS spectra were then combined with Redistribution Matrices File (RMF) of the GISs and Auxiliary Response File (ARF) files generated using the `ftool ascaarf`, and grouped with a minimum of 25 counts per bin. Finally the exposure of the grouped spectra were

---

[1] http://heasarc.gsfc.nasa.gov/ftools/xselect/

Table 4.1. X-ray observations of AXP 1E 1841−045 used in this study.

Date	Observatory	t^{a}(ks)	Offset[b]($'$)
1993 Oct 11	*ASCA*	40	6.8
1997 Apr 21	*ASCA*	9	7.3
1998 Mar 27	*ASCA*	39	6.5
1999 Mar 22	*ASCA*	20	5.3
1999 Mar 29	*ASCA*	20	5.2
1999 Apr 06	*ASCA*	19	5.2
1999 Apr 13	*ASCA*	21	5.2
2000 Jul 29	*Chandra*	10	0.097
2002 Oct 05	*XMM*	3.8	1.152
2002 Oct 07	*XMM*	4.4	1.144
2006 Apr 19	*Suzaku*	98	3.9

[a] The effective exposure time of the instrument used for the spectral analysis in this Chapter.

[b] The pointing offsets of the observations relative to the position of the AXP.

corrected for the deadtime effect using the `ftool deadtime`. In this study, we did not include the spectra extracted from the two Solid-state Imaging Spectrometers (SISs, Ohashi 1996), primarily because of the significantly fewer counts collected by these instruments.

4.2.2 Chandra Observations

The AXP and SNR were observed by the *Chandra X-ray Observatory* (see Section 2.4) with the ACIS (Garmire et al., 2003) in timed exposure (TE) mode on 2000 July 23 and in continuous clocking (CC) mode on 2000 July 29 (Table 4.1). The data were analyzed and reported by Morii et al. (2003). Here we used `Ciao` version 3.4[1]. Because the spectrum of the pulsar in TE mode was heavily affected by pile-up, we did not use these data; instead we extracted the spectrum of AXP 1E 1841−045 from the CC mode data. In these data, the image of the pulsar and SNR were collapsed into one dimension. From the level 2 event list provided by the *Chandra* X-ray Center, we extracted the spectrum of the pulsar using a box-shaped region capturing a $2''.5$ long segment along the one-dimensional image and centered on the pulsar. The background spectrum was extracted from two $7''.5$ long segments adjacent to the source region. The resulting source and background spectra were then combined with RMF and ARF files generated using the `psextract` command and grouped with a minimum of 25 counts per bin.

4.2.3 XMM-Newton Observations

The AXP was observed by the *XMM-Newton X-ray observatory* (Jansen et al. 2001; see Section 2.3) on 2002 October 5 and 2002 October 7 (Table 4.1) with the EPIC pn (Strüder et al., 2001) camera operating in large window mode and the EPIC MOS cameras (Turner et al., 2001) in full window mode. For our analysis, we used the *XMM* Science Analysis System (`SAS`) version 8.0.0[2] and calibrations (updated 2008 Oct 3). Given the pn and MOS cameras' angular resolution, 1E 1841−045 can be

---

[1] http://131.142.185.90/ciao3.4/index.html

[2] See http://xmm.esac.esa.int/sas/8.0.0/

resolved from Kes 73. For the two *XMM* observations, we used only the data from the EPIC pn camera to take advantage of its larger photon collecting area and to avoid cross-calibration issues between the pn camera and the mos cameras. Two sets of spectra were extracted from each *XMM* observation: the spectrum of only the pulsar, and the spectrum of the entire SNR Kes 73 including the pulsar. We extracted the pulsar's spectrum from a circular region of radius $32''.5$ (a radius large enough to capture more than 90% of the photon events from the point source) centered on the pulsar. Background spectra were extracted from an annular region of radius between $35''$ and $115''$ centered on the pulsar which included most of the emission from Kes 73, in order to remove the SNR contribution left in the source region. For the spectrum of the entire SNR, we used a circular source region of radius $115''$ and a circular background region located on the same CCD as the pulsar but at a different Y position. Ideally we want to extract background photons from region centered on the same Y position of the CCD, however this is not possible because the extended emission of the SNR. So we verified our result by choosing a different background region on an adjacent CCD, and found that the difference it makes in the final spectrum is negligible. Both of the spectra were grouped with a minimum of 25 counts per bin and then combined with the background spectrum and RMF and ARF files generated by the `SAS` software.

4.2.4 *Suzaku Observations*

AXP 1E 1841−045 and Kes 73 were also observed by the *Suzaku* observatory (Mitsuda 2007; see Section 2.1) on 2006 April 19 (Table 4.1). The data analysis was reported by Morii et al. (2008). Here we present a spectral analysis of the *Suzaku*-XIS data only. Given the angular resolution of the XIS, the SNR was unresolvable in the XIS image. Therefore the spectra we extracted from the XIS detectors contain photons from both the AXP and the SNR. We used cleaned events screened by the standard pipeline processing version 2.0.6.13[1]. The source spectra were extracted from a circular region of $260''$ radius. Background spectra were extracted from an annulus region of radius

---

[1] http://heasarc.nasa.gov/docs/suzaku/processing/criteria_xis.html

between 260″ and 520″. The extracted spectra were grouped with a minimum of 25 counts per bin, and then combined with the RMF and ARF files generated using the `ftools` `xisrmfgen` and `xissimarfgen`.

4.3 Spectroscopy

Among the eleven observations we used, the AXP can be resolved from the SNR Kes 73 only in the *Chandra* and *XMM* observations. For these, it is possible to extract either the neutron star's spectrum or the combined spectrum of the neutron star and the SNR. By contrast, only combined spectra can be extracted from the *ASCA* and *Suzaku* observations.

The spectra of AXPs are often parametrized by a blackbody plus a power-law (although this is known to be an approximation to a likely Comptonized blackbody spectrum – see Thompson et al. 2002 and, for example, Rea et al. 2008). The spectra of SNRs are often fit with models like, for example, VSEDOV (a plane-parallel shock radiation model with separate ion and electron temperatures), VNEI (a non-equilibrium ionization collisional plasma model), or VPSHOCK (a plane-parallel shocked plasma model). See (Borkowski et al., 2001) for a review of these models. In this Chapter, we modeled the neutron star radiation with a blackbody plus power-law (BB+POW), and the SNR radiation with a VSEDOV model, using `xspec 12.5.0`[1]. The focus of our investigation is on the AXP's X-ray flux; in modelling the SNR we sought only a suitable parameterization to allow us to subtract off its flux reliably. As we show below, the VSEDOV model is adequate for these purposes. We modeled the interstellar absorption by multiplying a WABS (a photo-electric absorption model, in which the interstellar absorption is characterized by a single parameter N_H, the neutral hydrogen column density along the line of sight) model to both the BB+POW and VSEDOV models.

Figure 4.1 shows the combined spectra from *XMM* and the components of the best-fit model. The AXP power-law component clearly dominates the spectra above

---

[1] http://heasarc.nasa.gov/docs/xanadu/xspec/

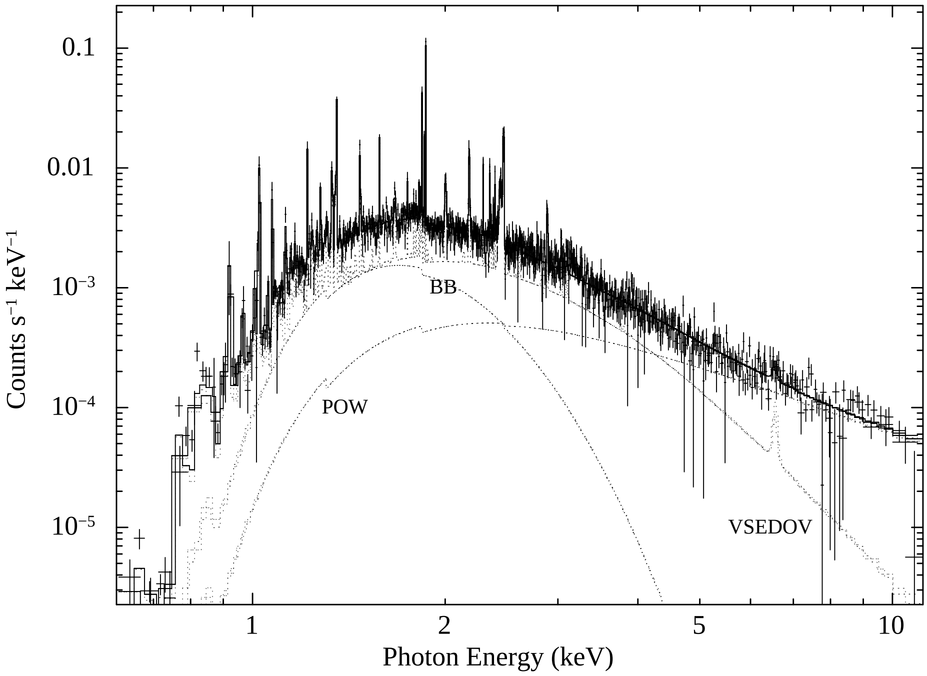

Figure 4.1 The unfolded *XMM* pn spectra and components of the best-fit BB+POW+VSEDOV model.

∼4 keV. Therefore, we chose to study the AXP flux in the 4–10 keV band only, in order to minimize SNR contamination. Nevertheless, we still attempted to remove the remaining small contribution of SNR in this band for the fluxes measured from *ASCA* and *Suzaku* observations, so that we could compare them with the neutron-star-only fluxes measured with *Chandra* and *XMM*.

It is reasonable to assume that both the interstellar absorption and SNR radiation do not change over a time scale of about a decade. Consequently, in our attempt to remove the SNR flux, we used the same N_H and VSEDOV parameters for all the spectra of the different observations, and allowed only the BB+POW model to vary from observation to observation.

When fitting a WABS(BB+POW+VSEDOV) model to those spectra containing emission from both the AXP and SNR, it is challenging to constrain the normalization parameters of both the BB and VSEDOV models simultaneously, because these two models dominate the same energy band and their parameters are highly covariant. Fortunately, the neutron star can be spatially resolved out in the *XMM* observations, so we can use them to determine the relative strength of the two spectral components. We therefore fit a WABS(BB+POW+VSEDOV) model to the combined (AXP+SNR) *XMM* spectrum. To ensure that we had the correct BB+POW model for the neutron star, we simultaneously fit the spectrum extracted from only the neutron star, requiring common neutron-star spectral parameters. Hence we could determine the parameters and normalization of the VSEDOV model for the SNR.

To further improve the spectral model, next we included the *ASCA* and *Suzaku* spectra and the *Chandra* CC-model neutron-star spectrum and performed a large joint fit, which required multiple iterations in order to converge. The result was a value for N_H and for the VSEDOV model parameters that fit all the SNR spectra reasonably well, albeit not perfectly (reduced $\chi^2 = 1.36$ for 3801 degrees of freedom for the joint fit). The best-fit N_H and VSEDOV parameters can be found in Table 4.2.

Note that for all the spectral fitting described above, we used the 0.8–10 keV band. However for *Suzaku*, we found that there were always significant residuals in the range 1.7–3.5 keV and above 9 keV, and in general, these residuals differed significantly among the four XIS instruments. Therefore, we ignored the 1.7–3.5 keV band and above 9 keV for the *Suzaku* spectra. Furthermore, the SNR Kes 73 is larger than the field-of-view of the *Suzaku* XISs and was not entirely captured. Therefore, when fitting the *Suzaku* spectrum, we allowed the VSEDOV normalization parameter to vary.

Finally, by using the best-fit N_H and VSEDOV model, we could remove the SNR flux contribution from the *ASCA* and *Suzaku* observations in separate fits to their spectra, hence measuring the AXP fluxes. For the *Chandra* and *XMM* observations, we simply fitted the resolved AXP spectra with an absorbed BB+POW model. The best-fit BB+POW parameters, the measured 4–10 keV unabsorbed fluxes of the AXP and the reduced χ^2 are presented in Table 4.3. The fluxes are also plotted in Figure 4.2. The uncertainties we report on the 4–10 keV unabsorbed AXP fluxes were estimated by the measured fractional uncertainties on the 4–10 keV absorbed total fluxes.

Table 4.2. WABS and VSEDOV parameter values

Parameter	Value
N_H	$2.77 \times 10^{22}\mathrm{cm}^{-2}$
kT_a	0.56 keV
kT_b	0.56 keV
Mg	0.63[a]
Si	1.10
S	1.92
Ca	0.32
Fe	0.57
Ni	2.51
τ	1.50×10^{11} s
Redshift	0.00
Norm[b]	0.33
$H...Ar$[c]	1.0

[a] The element abundances quoted here are the relative abundances based on the Solar mixture abundances.

[b] Normalization parameter for the VSEDOV model, $\frac{10^{-14}}{4\pi[D_A(1+z)]^2 \int n_e n_H dV}$ where D_A is the angular diameter distance to the source (cm), and n_e, n_H (cm^{-3}) are the electron and hydrogen densities respectively.

[c] Elements $H...Ar$: H He C N O Ne and Ar were fixed to the solar abundance because the SNR spectra are not sensitive to them.

Table 4.3. Measured model parameters and fluxes for 1E 1841−045.

Date	Observatory	MJD	kT[a](keV)	Γ	F_{NS}[b]	$\chi^2(\nu)$
1993 Oct 12	*ASCA*	49272.1	0.20	2.7	1.16(4)	2.3(293)
1997 Apr 21	*ASCA*	50559.6	0.19	3.0	1.2(1)	1.2(433)
1998 Mar 28	*ASCA*	50900	0.20	2.7	1.36(4)	2.0(294)
1999 Mar 22	*ASCA*	51259.7	0.20	2.9	1.29(4)	1.6(254)
1999 Mar 30	*ASCA*	51267.0	0.19	2.8	1.39(6)	1.6(254)
1999 Apr 06	*ASCA*	51274.6	0.21	2.7	1.39(4)	1.6(256)
1999 Apr 14	*ASCA*	51282.3	0.21	2.7	1.36(4)	1.4(261)
2000 Jul 29	*Chandra*	51754.32	0.40	2.1	0.975(3)	0.9(274)
2002 Oct 05	*XMM*	52552.16	0.22	2.6	1.05(4)	1.4(174)
2002 Oct 07	*XMM*	52554.16	0.21	2.5	1.08(3)	1.8(279)
2006 Apr 20	*Suzaku*	53846	0.38	1.9	1.03(2)	0.8(1163)

[a] The reported best-fit kT and Γ parameters of the BB+POW model vary depending on the assumed SNR model; we do not report the fit uncertainties of these parameters as they do not reflect the true uncertainties. The values, determined while assuming the VSEDOV model for SNR, are provided for reference only.

[b] Phase-averaged unabsorbed neutron-star flux in the 4–10 keV band the unit of 10^{-11}erg cm^{-2}s^{-1}. The number in parenthesis represents the 1σ uncertainties in the last digit. See text for details.

For those observations in which the best-fit reduced χ^2 was larger than unity, we multiplied the reported flux uncertainties by the square root of the reduced χ^2. This is to account for systematic errors in our imperfect modelling of the SNR spectrum.

Some of the reduced χ^2 values of the separate fits are large (see Table 3), with the largest value of 2.3 from the first *ASCA* observation. These appear to be caused by residual features in the spectra that could not be fitted by the VSEDOV model. This is not necessarily surprising given that probably the summed, overall spectrum of the entire SNR Kes 73 is more complicated than a single VSEDOV model can describe. However this issue likely affects the overall flux normalization for the SNR

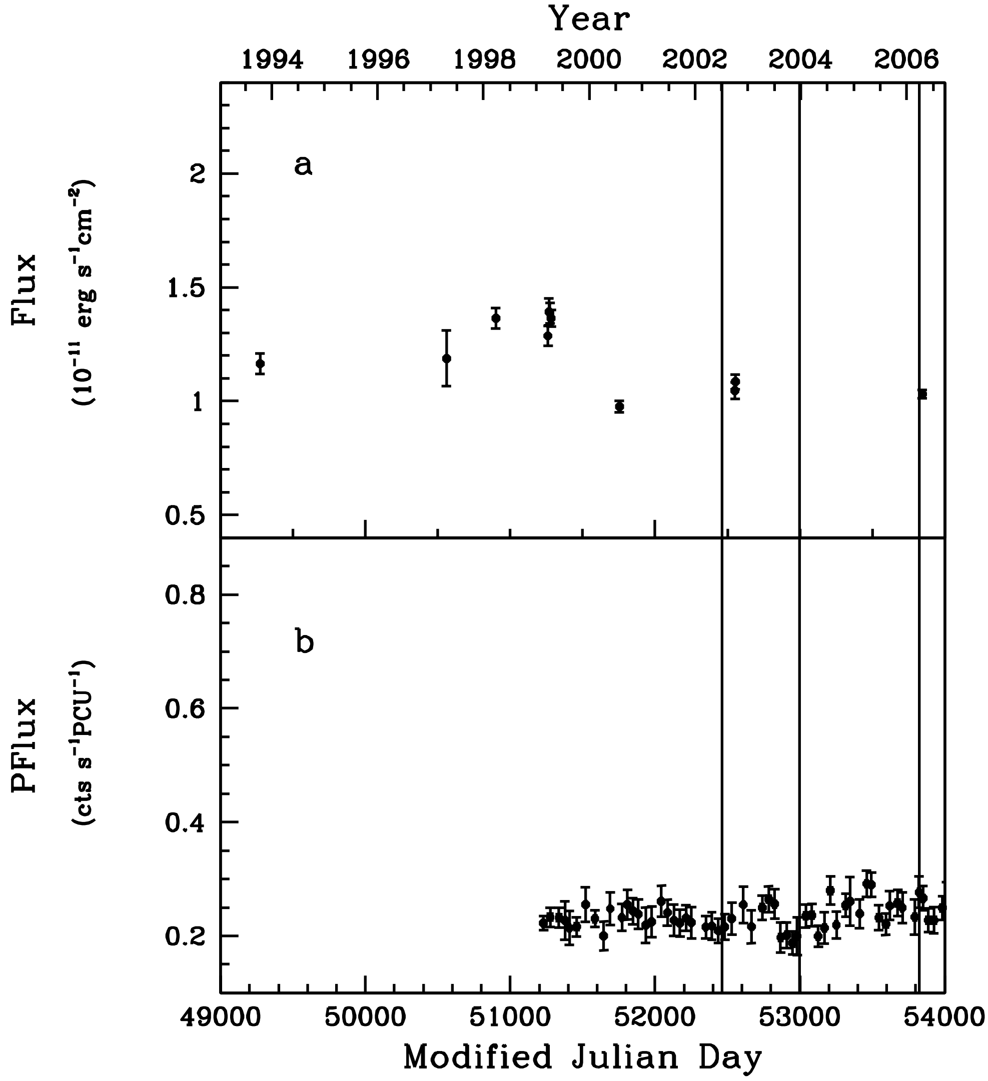

Figure 4.2 (a) 4–10 keV unabsorbed phase-averaged fluxes from AXP 1E 1841−045, as determined by our analysis. (b) 2–10 keV pulsed fluxes from the pulsar as measured by *RXTE* , in units of counts per second per Proportional Counter Unit (PCU) (see Dib et al., 2008b, for details).

spectrum very little. Since here we are concerned with the flux of the AXP only, not the spectrum of the SNR, the SNR flux normalization should be good enough for our purposes.

Indeed, to confirm the robustness of the measured AXP flux values, we repeated the entire above analysis by modelling the SNR spectra in different ways. We found that both the VNEI and VPSHOCK models can fit the SNR spectra as well as the VSEDOV model, and that the 4–10 keV unabsorbed neutron star fluxes we measured using these models are consistent within reported uncertainties with the values we found using the VSEDOV model. Therefore, we feel confident that the phase-averaged AXP flux values we report are well constrained and robust. However, the BB+POW spectral parameters we measured when fitting the SNR with different models were not as robust as the 4–10 keV fluxes, changing significantly with SNR model. As we do not believe them to be reliably determined, we do not quote their uncertainties in Table 4.3, and do not consider them further.

Also in Figure 4.2, we show the AXP's 2–10 keV pulsed flux as measured in monitoring observations with *RXTE* since early 1999. Details about how these pulsed fluxes were determined are provided in Dib et al. (2008b). The *RXTE* pulsed fluxes show no significant variations. The vertical lines in Figure 4.2 indicate the epochs of the three observed glitches (Dib et al., 2008b).

4.4 Discussion

The goal of this study was to see whether the prolific glitching AXP 1E 1841−045 shows phase-averaged flux variability, in spite of showing no evidence for pulsed flux variability. Also, we wished to determine whether any variability is correlated with its glitches as has been seen in AXP 1E 2259+586 in its 2002 major outburst, in 1E 1048.1−5937, and also reported for RXS J170849.0−400910 .

As is clear from of Figure 4.2(a), in the 4–10 keV band, the neutron star's flux did not vary by more than ∼30% in 13 years. Interestingly the largest variations we find are in the multiple pre-1999 *ASCA* observations: in those seven observations, a fit to a constant flux results in a reduced χ^2 of 3.7 for 6 degrees of freedom, which has a probability of occurring by chance of ∼0.001. However, during this time, there were certainly no large glitches ($\Delta\nu/\nu < 5 \times 10^{-6}$) (Gotthelf et al., 1999).

The *ASCA* fluxes appear to be ∼ 30% higher than the fluxes measured from other observations. Snowden (2002) studied the cross-calibration accuracy between *ASCA*, *XMM* and *Chandra* , and found that their flux difference due to calibration should be < 20%. This suggests that the AXP's flux dropped around 2000. However, we did not see any significant changes in the pulsed flux as monitored by *RXTE* at that epoch (Figure 4.2(b)). In principle, it is possible for the pulsar's total flux to vary while the pulsed flux remain constant. In that case, the pulsed fraction of the pulsar must have also changed during the same epoch and it must be precisely anti-correlated with the total flux. An anti-correlation between pulsed fraction and flux has been observed from AXP 1E 1048.1−5937 during one of its active phase, but the variability in its pulsed flux was still very significant (Tiengo et al., 2005; Tam et al., 2008).

The fluxes measured from the last four observations taken by *Chandra* , *XMM* and *Suzaku* can be fitted with a constant flux model (reduced $\chi^2 = 1.9$ for 3 degrees of freedom, corresponding to a probability of having occurred by chance of 0.125). Thus we conclude that the phase-averaged 4–10 keV fluxes of the last four observations were consistent with being constant, and we put an upper limit of 11% on long-term variability in this energy band. Importantly, the two *XMM* observations were taken only 88 and 90 days after the first glitch, and the *Suzaku* observation was taken only 27 days after the third glitch. By contrast, the 4–10 keV flux of 1E 2259+586 was 50% higher than in quiescence 21 days after its 2002 glitch (Zhu et al., 2008), that of 1E 1048.1−5937 was a factor of 6 higher ≥38 days after its 2007 glitches (Tam et al., 2008), and was 50–70% higher for RXS J170849.0−400910 ∼53 days after its first 2005 glitch as inferred from Götz et al. (2007)[1]. Therefore, we con-

---

[1] This is calculated based on the reported 1–10 keV fluxes of RXS J170849.0−400910 from its 2003 *XMM* observation and 2005 *Swift* observation. We assumed a power-law to blackbody flux ratio of 3 for the 1-10 keV fluxes, and then calculated the 4–10 keV fluxes using webPIMMS (http://heasarc.gsfc.nasa.gov/Tools/w3pimms.html).

clude that unlike the glitches observed in 1E 2259+586, 1E 1048.1−5937 and possibly RXS J170849.0−400910, the 2002 and 2006 glitches of 1E 1841−045 were not accompanied by significant X-ray flux variations when compared to the 2000 *Chandra* flux. More generally speaking, we found no evidence for glitch-correlated flux changes in AXP 1E 1841−045 after 1999. However, we cannot rule out glitch-correlated flux changes before 1999 due to the sparsity of the observations.

One caveat of our study is that we were limited to the harder part of the neutron star's emission spectrum. The flux from the blackbody component was not well constrained. Therefore, we cannot rule out changes in the neutron star's thermal radiation, only changes in the power-law component in the 4–10 keV band, which we note constitutes ∼0.25 of the stellar flux (BB+POW) in the 1–10 keV band.

Thus our results support the existence of radiatively silent glitches in AXPs, further supporting the argument that glitches in AXPs can be either radiatively loud or radiatively silent (Dib et al., 2008b). There is of course precedent for radiatively silent glitches in neutron stars, in that no rotation-powered pulsar glitch has ever been reported to be accompanied with any radiative change, although rapid X-ray follow-up has been accomplished in only one case (Helfand et al., 2001). Any physical model of magnetar glitches will have to explain the simultaneous existence of both types. This is true of even a single source, as there is evidence that AXP 1E 2259+586 has both, given that its most recent glitch showed no pulsed flux change (Dib et al., 2008a). Recently Eichler & Shaisultanov (2010) have argued that AXP glitches are triggered by energy releases at depths below ∼100 m in the crust, with angular momentum vortex unpinning being due to global mechanical motion triggered by the energy release, not by heat as has been proposed in the context of rotation-powered pulsars glitches (Link & Epstein, 1996; Link & Cutler, 2002). If mechanical triggering occurs, then radiatively silent glitches of the same amplitude as radiatively loud glitches are possible since less energy is required to trigger a glitch than to cause a substantial X-ray brightening. If so, then Eichler & Shaisultanov (2010) predict that all radiatively loud AXP glitches should occur simultaneously with or before the observed X-ray brightening; this can be tested with continuous (daily or better) X-ray monitoring observations. Moreover, although mechanical unpinning of vortices by activity in the lower crust does result in heat release, the latter could take as much as several years to reach the surface. This could help explain the long-term X-ray variability trends that have been reported in some AXPs (e.g. Dib et al., 2007).

4.5 Summary

This Chapter reports an analysis of archival X-ray data from the AXP 1E 1841−045, obtained between 1993 and 2007. This AXP had exhibited three glitches between 2002 and 2007, as determined by *RXTE* monitoring since 1999. We searched for evidence of phase-averaged flux variability that could be present if glitches in AXPs are usually accompanied by radiative changes (see Section 1.2.2). No such evidence was found from this source after 1999. This suggests that AXP glitches are not generically accompanied by significant radiative changes.

5

X-ray Detection of the High-B PSR B1916+14

The content of this Chapter is reported in the paper "*XMM-Newton* X-Ray Detection of the High-Magnetic-Field Radio Pulsar PSR B1916+14" published in the *Astrophysical Journal* (Zhu et al., 2009).

5.1 Introduction

High-magnetic-field RPPs (See Section 1.3) are a crucial group of pulsars. They may be transition objects between RPPs and magnetars. Some of them may even be quiescent magnetars. Recent observations have revealed magnetar-like behaviours in one of the high-B pulsars. In theory, the decay of their strong magnetic field may change their cooling history, rendering some of them hotter than other RPPs of the same age. If this field decay theory is true, then the high-B RPPs may be the progenitors of the XINS (see Section 1.1.2). In this Chapter, we seek to test this theory by observing one of the closest known high-B RPPs, PSR B1916+14.

PSR B1916+14 is a radio pulsar having period P =1.181 s, with spin-down-inferred magnetic field $B \equiv 3.2 \times 10^{19}(P\dot{P})^{1/2}$ G= 1.6×10^{13} G, spin-down age $\tau \equiv P/(2\dot{P}) = 8.8 \times 10^{4}$ yr, and $\dot{E} \equiv 4\pi^{2}I\dot{P}/P^{3} = 5 \times 10^{33}$erg s^{-1} (Hulse & Taylor, 1974; Manchester et al., 2005). It is a relatively young and nearby pulsar. Given its age and distance, PSR B1916+14 should still be hot enough to be X-ray detectable, according to a minimal pulsar cooling model, without magnetic-field-decay heating (Page et al., 2006). It is also one of the highest-magnetic-field radio pulsars known and may therefore be hotter because of magnetic-field decay. This makes PSR B1916+14 a good test subject for neutron star cooling models, and hence X-ray observations.

5.2 Observations and Results

PSR B1916+14 was observed by the *XMM-Newton* observatory (Jansen et al. 2001; see Section 2.3) on 2008 March 25. Both the EPIC pn (Strüder et al., 2001) camera and the EPIC MOS cameras (Turner et al., 2001) were operating in full window mode with the thin filter, and with a pointing offset of $1'.107$. We analyzed the data taken in this *XMM* observation, and found that PSR B1916+14 was clearly detected in both the pn and MOS data.

5.2.1 Imaging and Source Detection

The *XMM* data were analyzed with the *XMM* Science Analysis System (SAS) version 8.0.0[1] and the latest calibrations (updated 2008 Oct 3). To exclude strong background flares that sometimes contaminate *XMM* data, we extracted light curves of photons above 10 keV from the entire field-of-view of the pn and MOS images, and excluded the time intervals in which background flares occurred for all subsequent analyses. The total exposure time of the observation is $\sim$ 25 ks. However, after excluding the bad time intervals within which the background flux was very high (>10 counts per second) and showing significant burst-like features, only 12 ks of pn, 11 ks of MOS1 and 13 ks of MOS2 data were used in our analysis. The data were also corrected to the barycenter using the SAS `barycen` tool after background flares were excluded, using the nominal pulsar position (J2000) R.A. 19:18:23.638(7) Decl. +14:45:06.00(15) (Hobbs et al. 2004).

In order to find the X-ray counterpart of PSR B1916+14, we used the SAS tool `edetect_chain` to perform a blind search for point sources. `edetect_chain` is designed to find point sources using a sliding cell technique and to calculate the significance of any detection using a maximum likelihood method. It generates an output source list file containing information like total counts, position and significance of detected sources. In the pn image, a point source was detected coincident with the position of PSR B1916+14 (Fig. 5.1) by `edetect_chain`. The source has 133 ± 15[2]

---

[1] See http://xmm.esac.esa.int/sas/8.0.0/

[2] Unless otherwise specified, the uncertainties quoted in this Chapter represent the 1σ range.

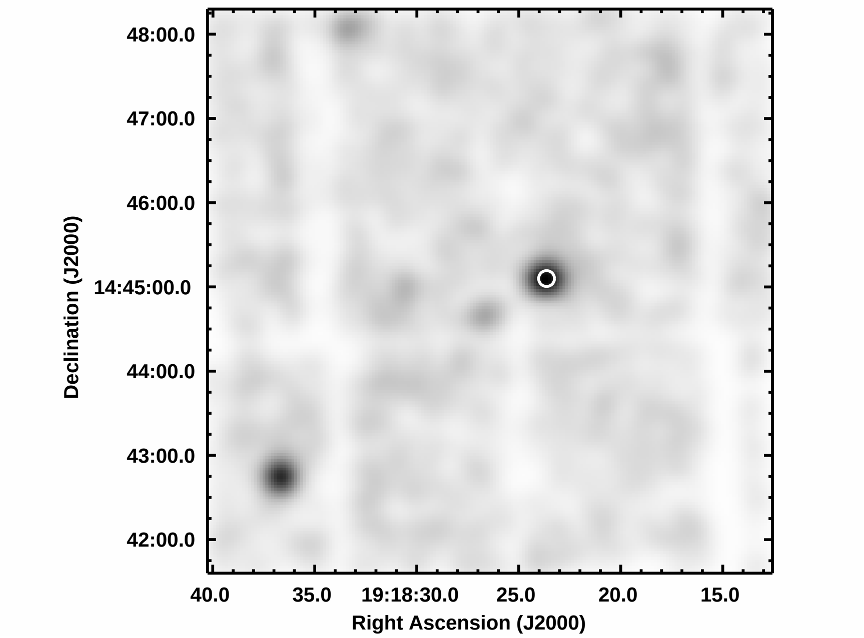

Figure 5.1 *XMM* image in the 0.2–2 keV energy band, smoothed by a Gaussian profile of 8.2″ radius (a profile that is slightly oversampling the telescope's PSF). The radio position of PSR B1916+14 is labeled by the white circle. Note that the radius of the circle is much larger than the uncertainty on the radio position.

counts in 0.1–10 keV band and a likelihood ratio of $L_2 = -\ln(P) \simeq 143$ (where P is the probability for a random Poissonian fluctuation to have caused the observed source counts). This source was also detected in the MOS 1 image with 22 ± 7 counts and $L_2 \simeq 11$, and in the MOS 2 images with 46 ± 9 counts and $L_2 \simeq 48$, both in the 0.1–10 keV range. Thus, this point source was clearly detected in the pn and the MOS data.

Figure 5.1 is the pn image, smoothed with a Gaussian profile of radius $\sigma = 8''.2$. The small circle in the center of the image marks the radio position of PSR B1916+14 . The position uncertainty is smaller than the size of the circle (Hobbs et al., 2004). The best-fit position of the detected source given by `edetect_chain` is (J2000) R.A. 19:18:23.74(5) Decl. +14:45:06.2(8), consistent with the radio position of PSR B1916+14 . Therefore, it is very likely that the source we detected is the X-ray counterpart of PSR B1916+14 .

The radially averaged profile of *XMM* 's point spread function can be approximated by an analytic function – the King function $\rho(r) = A[1 + (\frac{r}{r_0})^2]^{-\alpha}$, where $\rho(r)$ is the number density of counts at radius r, A is a normalization parameter, r is the radial distance between the events and the center of the source, r_0 and α are parameters reflecting the size and shape of the point spread function (PSF) and are functions of energy and off-axis angle.[1] In order to search for evidence of extended emission from PSR B1916+14 , we extracted 0.2-12 keV photon events from a circular region of $35''$ radius around the best-fit position, and calculated the radial distance between every photon event and the pulsar, to get the radially averaged profile. Using the Kolmogorov-Smirnov (K-S) test, we then compared the observed radially averaged profile to a model composed of a King function. Given the small off-axis angle, and the energy distribution of the source, we chose $\alpha = 1.6$ and $r_0 = 5.25$ pixels= $21''.525$ and a uniform background (0.05 photons/acrsec^2, inferred from the 397 photons found in a circular background region of $50''$ radius and $\sim 3'$ away from PSR B1916+14). The K-S test shows that the radially averaged profile can be well matched by the specified King function. Therefore, there is no evidence for extended emission near PSR B1916+14 from this observation.

5.2.2 Spectroscopy

We extracted the X-ray spectrum of PSR B1916+14 from the pn data using a circular region of $32''.5$ radius encircling the source. The source region should contain more than 80% of the counts from a point source. The background spectrum was extracted from a circular region of $50''$ radius and $\sim 3'$ away from the pulsar where no source was detected. Both single- and double- events were selected, but events that hit or were close to a bad pixel or CCD gap were excluded using the filter expression FLAG = 0&&PATTERN <= 4. A response file and an auxiliary response file were generated using the SAS command `rmfgen` and `arfgen`. The spectrum was grouped to have a minimum of 15 photons per bin using the `ftool grppha`, and was then fed

---

[1] See http://xmm.esac.esa.int/docs/documents/CAL-TN-0018-2-6.pdf, page 6

to XSPEC 12.3.0[1] for spectral fitting.

We also extracted spectra from the data of the two MOS detectors using source circular regions of 36″ radius and background regions of $\sim 60''$ radius. Single- to quadruple- photon events were selected except those that landed on a bad pixel or CCD gap, using the filter expression of XMMEA_EM&&PATTERN <= 12. We then combined the two MOS spectra into a single MOS spectrum and averaged their background, response and auxiliary files using the `ftool addspec`. The resulting MOS spectrum was also grouped to have a minimum of 15 photons per bin and was fitted jointly with the pn spectrum.

The X-ray spectra of PSR B1916+14 can be well fit with an absorbed blackbody model. However, due to the small number of counts, the column density N_H was poorly constrained. The best-fit N_H is $\sim 1\times10^{19}$ cm^{-2}, too small given the estimated distance and location of the pulsar. Therefore, we estimated the N_H for this pulsar based on the total N_H (1.58×10^{22} cm^{-2}) of the Galaxy along the line-of-sight[2] and the distance to the pulsar (2.1 ± 0.3 kpc, estimated from the 27.2 pc cm^{-3} dispersion measure of the pulsar; Cordes & Lazio, 2002), and find a moderate value of $\sim 0.14 \times 10^{22}$ cm^{-2}. Fixing N_H to this value, the best-fit blackbody temperature for the 0.1–2 keV spectra (Fig. 5.2) is 0.13 ± 0.01 keV (Table 5.1). The model-predicted absorbed flux in the 0.1–2 keV range is $1.4{\pm}0.3{\times}10^{-14}$ erg s^{-1} cm^{-2}. Assuming a distance of 2.1 kpc, we find the bolometric X-ray luminosity of PSR B1916+14 to be $\sim 3 \times 10^{31}$ erg s^{-1}.

By fixing N_H while fitting the pn and MOS spectra, we underestimate the uncertainties of the best-fit parameters. In order to get a sense of the real uncertainty of kT, we tried fitting with a range of N_H. N_H likely lies between 0.07×10^{22} cm^{-2} and 0.3×10^{22} cm^{-2}. It is probably not smaller than 0.07×10^{22} cm^{-2} because the distance estimated from the dispersion measure is unlikely to be incorrect by more than 50%. Also, an absorbed blackbody model with N_H higher than 0.3×10^{22} cm^{-2} cannot fit the spectra well for any kT. With N_H restricted to lie between these two values, the

---

[1] http://heasarc.gsfc.nasa.gov/docs/xanadu/xspec/

[2] http://cxc.harvard.edu/toolkit/colden.jsp

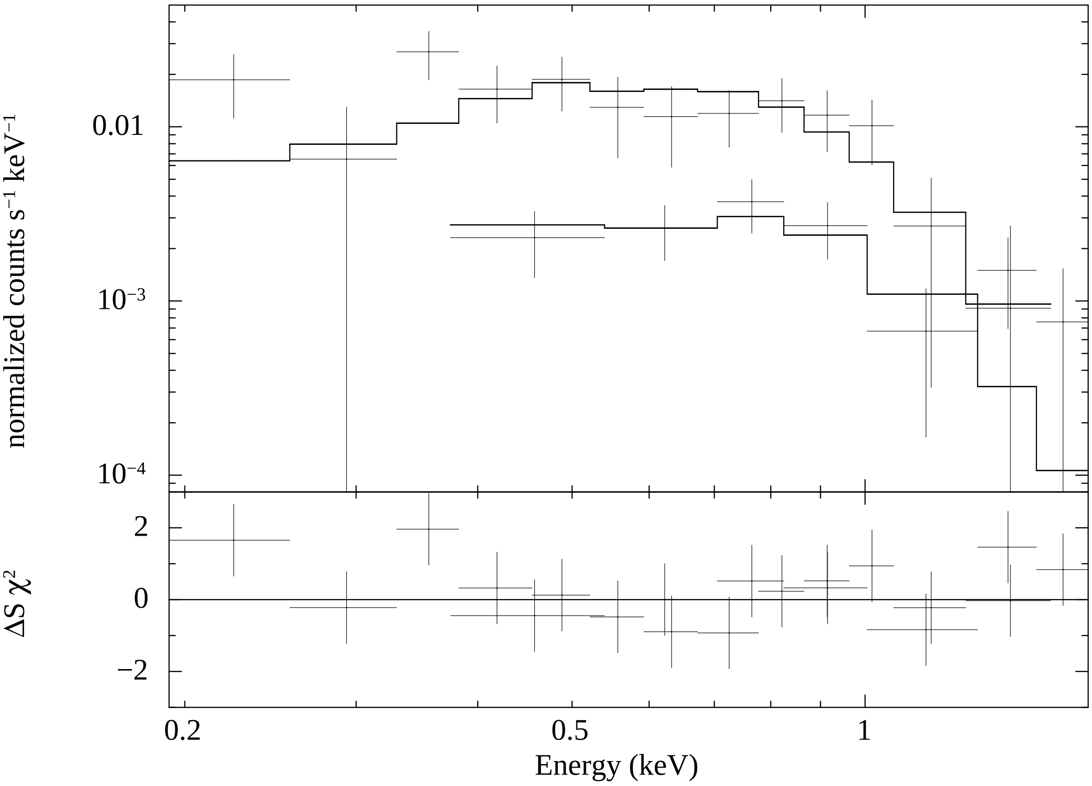

Figure 5.2 *XMM* spectra (upper is pn, lower is combined MOS) of PSR B1916+14, with the best blackbody fit (see Table 5.1). The spectra are binned to contain a minimum of 15 counts per bin.

Table 5.1. Best-fit Spectral Parameters for PSR B1916+14

Parameter	Blackbody model[a]	Power-law model	NSA model[d]
N_H (10^{22} cm^{-2})	0.14	$0.12^{+0.05}_{-0.07}$	$0.23^{+0.09}_{-0.04}$
kT (keV)	0.13±0.01	—	0.10 ± 0.04
R_{bb} (km)	0.8 ± 0.1	—	—
R_{NS} (km)	—	—	~6
Γ	—	$3.5^{+1.6}_{-0.7}$	—
χ^2(dof)	14.1(18)	13.9(17)	14.3(17)
$f_{\rm abs}$[b](erg s^{-1} cm^{-2})	$1.4 \pm 0.3 \times 10^{-14}$	$1.7^{+0.4}_{-0.6} \times 10^{-14}$	$(1.7 \pm 0.3) \times 10^{-14}$
$f_{\rm unabs}$[c](erg s^{-1} cm^{-2})	$(5 \pm 1) \times 10^{-14}$	$\sim 2 \times 10^{-13}$	$(1.4 \pm 0.8) \times 10^{-13}$
$L_{\rm X}$ (erg s^{-1})	$\sim 3 \times 10^{31}$[e]	$\sim 1 \times 10^{32}$[f]	$(7 \pm 4) \times 10^{31}$

[a] Best-fit parameters of absorbed blackbody fit to the *XMM* spectra. N_H was frozen when fitting, so the uncertainties of the parameters, especially that of the kT, do not reflect the uncertainties on N_H; see text for details. Emission radius R_{bb} was inferred assuming a distance of 2.1 kpc (estimated from the dispersion measure; Hobbs et al. 2004).

[b] Absorbed X-ray flux, $f_{\rm abs}$ in the 0.1–2 keV range.

[c] Unabsorbed X-ray flux, $f_{\rm unabs}$, in the 0.1–2 keV range; the uncertainty was propagated from the uncertainties on the parameters and absorbed flux.

[d] When fitting with NSA model, the flux and luminosity are estimated using the `cflux` model in XSPEC.

[e] Bolometric X-ray luminosity derived assuming a distance of 2.1 kpc.

[f] Inferred X-ray luminosity in the 0.1–10 keV range assuming a distance of 2.1 kpc.

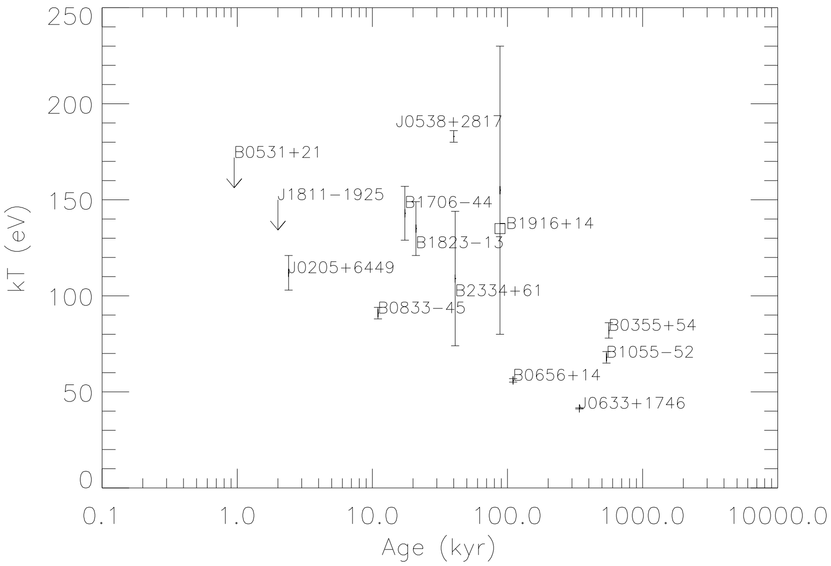

Figure 5.3 Observed temperature (kT) versus age for X-ray-detected radio pulsars. Note that for PSR B1916+14 we used the kT measured by allowing N_H to vary in a reasonable range; the same is not necessarily true for the other measurements; see original references in Table 5.2 for details.

acceptable (null hypothesis possibility of the fit > 0.01) range of kT is 0.08 to 0.23 keV (with blackbody radius range from ∼6 km to ∼0.2 km). This temperature range reflects reasonable uncertainties on N_H, and is quoted in the abstract and Figures 5.3 and 5.4 (see below).

The pn and MOS spectra could also be fit with a power-law model, with a best-fit N_H of $0.12^{+0.05}_{-0.07} \times 10^{22}$ cm^{-2} and a photon index of $\Gamma \sim 3.5^{+1.6}_{-0.7}$ (Table 5.1). The lack of source photons with energy above 2 keV results in a soft best-fit power-law model. This is rarely seen from other non-thermally emitting pulsars. Therefore, it is very unlikely that the X-ray emission of PSR B1916+14 is non-thermal.

A neutron-star hydrogen atmosphere (NSA) model (with magnetic field strength set to 10^{13} G; Zavlin et al., 1996; Pavlov et al., 1995) could also fit the pn and MOS spectra. However, the parameters are even less constrained in comparison with the blackbody model. We had to freeze the mass of the neutron star to 1.4 $M_\odot$ and the distance to 2.1 kpc to get a better-constrained fit ($\chi^2(\nu) = 14.3(17)$). The best-fit N_H

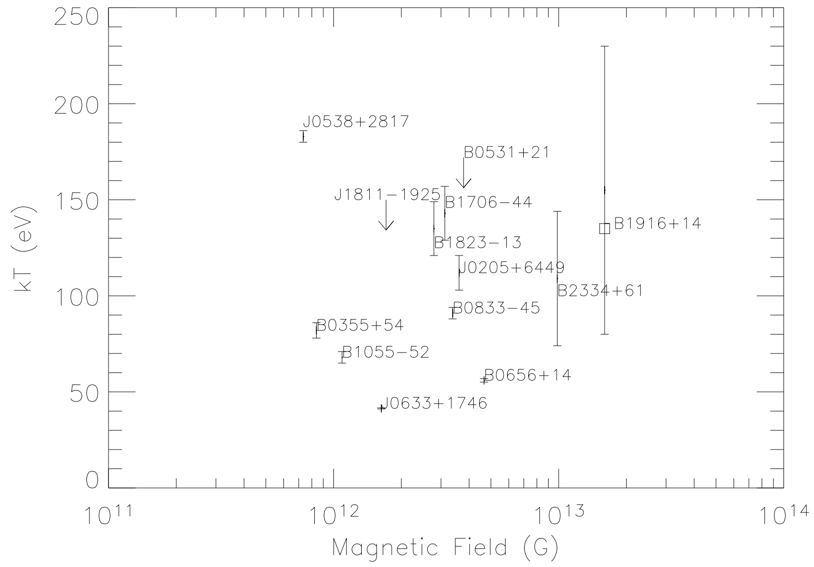

Figure 5.4 Observed temperature (kT) versus magnetic field strength for X-ray-detected radio pulsars. See caption for Figure 5.3 for caveats.

is $0.23^{+0.09}_{-0.04} \times 10^{22}\text{cm}^{-2}$, kT is 0.10 ± 0.04 keV, and the resulting best-fit neutron-star radius is ∼6 km. Unfortunately, the radius is not well constrained in this model and has a 1σ upper limit of 20 km. The model predicted 0.1–2 keV X-ray luminosity is $(7 \pm 4) \times 10^{31}\text{erg s}^{-1}$.

5.2.3 *Timing analysis*

To search for X-ray pulsations from PSR B1916+14 , we folded all the pn source events from a total 25 ks exposure without filtering for the background flares using 16 phase bins and a contemporaneous ephemeris which was derived from radio timing data obtained using the 76-m telescope at the Jodrell Bank Observatory (Hobbs et al., 2004). The MOS full-window mode data is useless for timing analysis because of its 2.7 s time resolution. A total of 374 pn photon events were extracted without filtering for background flares, all in the range of 0.1-2 keV, from a source region of $15''$ radius chosen to reduce the number of background photons and improve the signal-to-noise ratio. From the same energy band and the same CCD, 1945 events were found in a circular background region of $50''$ radius where no source was detected by the SAS tool `edetect_chain`. If the background is uniformly distributed, there should be 175±4 background photons in the source region. The folded and binned light curve was fit to a constant line. The best-fit χ^2 was 9.6 for 15 degrees of freedom. Therefore no significant pulsations were detected.

In order to determine an upper limit on the pulsed fraction, we simulated event lists with the same total number of counts as in the observed event list. The simulated event lists were generated assuming the signal has a sinusoidal profile starting at a random phase and a specified area pulsed fraction, where the area pulsed fraction is defined as the ratio of the pulsed part of profile to the entire profile. For a sinusoidal profile $F = A\sin\theta + B$, where F is the count rate, A is the amplitude, B is the DC level, and θ is the phase, the area pulsed fraction is $A/(2B + A)$. By specifying different area pulsed fractions, we found that, if we set the area pulsed fraction of the simulated event lists to 35%, then approximately 68% of them would be detected with $> 3\sigma$ significance. Because there are ∼175 background photons in the 374 photons from the source region, the 1σ area pulsed fraction upper limit of the pulsar is ~ 0.7. This is not an especially interesting constraint because the number of source photons was so small that even a highly pulsed signal could have gone undetected.

5.3 Discussion

The X-ray spectrum of PSR B1916+14 is soft, and therefore is most likely thermal. The blackbody temperature lies in the range of 0.08–0.23 keV, and the best-fit effective temperature of NSA model is 0.10 ± 0.04 keV. Given PSR B1916+14's age, its temperature is consistent with what one would expect ($kT \sim$ 0.07–0.11 keV) from minimal cooling models in which magnetic field is not considered (Page et al., 2006). Its estimated bolometric luminosity ($\sim 3 \times 10^{31}$erg s^{-1}; Table 5.1) is somewhat low when compared with the curves of Page et al. (2006), suggesting that the pulsar may have a light-element envelope. However the substantial uncertainties on the luminosity preclude a firm conclusion. On the other hand, fast cooling models predict much lower temperatures ($kT < 30$ eV; e.g. Yakovlev & Pethick 2004) which would be undetectable with current instruments. Therefore, fast cooling seems unlikely for PSR B1916+14 from our observation.

The small best-fit blackbody radius (0.8 ± 0.1 km; Table 5.1) suggests polar-cap reheating (see Chapter 1). If the emission of the pulsar is due to curvature radiation, return-current heating is predicted to give rise to an X-ray luminosity (see Harding & Muslimov 2001 and Eq. 7.2 in Kaspi et al. 2006 for details)

$$L_{+}^{(CR)} \simeq 10^{31}\mathrm{erg\ s}^{-1} \begin{cases} 0.4P^{-6/7}(\tau/10^{6})^{-1/7} & \text{if } P \leq 0.1(B/10^{12})^{4/9} \\ 1.0P^{-1/2} & \text{if } P \geq 0.1(B/10^{12})^{4/9}, \end{cases} \tag{5.1}$$

where τ is in yr, P is in s, and B is in G. For PSR B1916+14 , $L_{+}^{(CR)}$ is $\sim 9 \times 10^{30}\mathrm{erg\,s}^{-1}$, only a factor of ∼3 smaller than the estimated blackbody bolometric luminosity (see Table 5.1). If the emission is due to inverse Compton scattering, the return current heating will be much less effective (Harding & Muslimov, 2002). Given that the best-fit blackbody parameters are not well constrained, we cannot rule out return current heating as the origin of PSR B1916+14 's X-ray luminosity. We note that the NSA model (Section 5.2.2) yields a larger radius, although it is also not well constrained.

To compare the properties of PSR B1916+14 to those of other X-ray-detected radio pulsars, we have collected the temperature, magnetic field strength, and spin-down energy of a dozen such pulsars from the literature, and listed them in Table 5.2. For pulsars in this Table, we also made plots of their temperature versus age and magnetic field (Figs. 5.3 and 5.4, respectively). Given the large uncertainty on the temperature measurement from our short-exposure observation of PSR B1916+14 , we cannot conclude here whether thermal emission is consistent with minimal cooling or if the neutron star is hotter than lower-magnetic-field pulsars of the same age, as expected in some models (Pons et al., 2007; Aguilera et al., 2008). A longer observation in the future may be able to distinguish among thermal models.

However, we note with interest that the previously published temperature of PSR J0538+2817 is surprisingly high, in spite of its relatively large age (40 kyr) and relatively low magnetic field (7.3×10^{11} G; Table 5.2). In contrast to PSR B1916+14 , PSR J0538+2817's emission is unlikely to be from polar-cap reheating because of

Table 5.2. Parameters of the X-ray-detected Radio Pulsars

Name	Age[a](kyr)	kT^{b}(eV)	B^{c}(G)	$\dot{E}^{\mathrm{c}}(\mathrm{erg\,s^{-1}})$	Observatory	Spectral model[d]	Reference
B1916+14	88	135(45)	$1.6{\times}10^{13}$	5.1×10^{33}	*XMM*	BB	this work
B1055−52	540	68(3)	$1.1{\times}10^{12}$	3.0×10^{34}	*XMM*	BB+BB+PL	De Luca et al. 2005
J0633+1746 (Geminga)	340	41.4(0.1)	$1.6{\times}10^{12}$	3.2×10^{34}	*XMM*	BB+PL	Jackson & Halpern 2005
B0656+14	110	56.0(0.9)	$4.7{\times}10^{12}$	3.8×10^{34}	*XMM*	BB+BB+PL	De Luca et al. 2005
B0355+54	562	82(4)	$8.4{\times}10^{11}$	4.5×10^{34}	*ROSAT/Einstein*	BB	Slane 1994
J0538+2817	40[e]	183(3)	$7.3{\times}10^{11}$	4.9×10^{34}	*XMM*	BB	McGowan et al. 2003
B2334+61	41	109(35)	$9.9{\times}10^{12}$	6.2×10^{34}	*XMM*	BB+PL	McGowan et al. 2006
B1823−13	21	135(14)	$2.3{\times}10^{12}$	2.8×10^{36}	*Chandra*	BB	Pavlov et al. 2008
B1706−44	17.4	143(14)	$3.1{\times}10^{12}$	3.4×10^{36}	*Chandra*	BB+PL	Gotthelf et al. 2002
J1811−1925	2[f]	<150	$1.7{\times}10^{12}$	6.4×10^{36}	*Chandra*	BB+PL	Kaspi et al. 2006
B0833−45 (Vela)	11	91(3)	$3.4{\times}10^{12}$	6.9×10^{36}	*XMM*	BB+BB+PL	Manzali et al. 2007
J0205+6449	2.4[f]	112(9)	$3.6{\times}10^{12}$	2.7×10^{37}	*Chandra*	BB+PL	Slane et al. 2004
B0531+21 (Crab)	0.955[f]	<172	$3.8{\times}10^{12}$	4.6×10^{38}	*Chandra*	BB+PL	Weisskopf et al. 2004

[a] The spin-down age unless otherwise noted.

[b] The blackbody temperature or the temperature of the softer blackbody component as measured by fitting the data with different spectral models as listed in this Table.

[c] Numbers were found in the ATNF database (Manchester et al., 2005).

[d] BB: blackbody model; BB+PL: blackbody plus power-law model; BB+BB+PL: two blackbody plus power-law model.

[e] The age of PSR J0538+2817 estimated based on the proper motion of the pulsar from its associated SNR (Ng et al., 2007).

[f] The age of SNR with which the pulsar is associated, estimated based on its expansion rate: PSR J1811−1925 (Kaspi et al., 2006); PSR J0205+6449 (Chevalier, 2005). The age of PSR B0531+21 (Crab pulsar) is based on historical record.

the very high required efficiency for conversion of $\dot{E}$ to X-ray luminosity, $\sim 10^{-2}$, compared with the $\sim 5 \times 10^{-4}$ predicted by Equation 1 above for this pulsar. If correct, the high temperature suggests a wider range of possible temperatures for young neutron stars than is currently predicted. This would be a challenge to the Pons et al. (2007) model.

Although PSR B1916+14 is detected by *XMM* as a point source with no evidence of extended emission, it is still possible that extended emission was too faint to be detectable. Based upon the number of counts in the background region, we found that, in the 0.3–8 keV band, extended emission of surface brightness smaller than $\sim 3 \times 10^{-6}$ count $\mathrm{s}^{-1}\mathrm{arcsec}^{-2}$ would not be detected (with 3σ significance) in our observation. This limits our sensitivity for detecting a very faint pulsar wind nebula (PWN) like that of the Geminga pulsar, which has a surface brightness of $\sim 1 \times 10^{-6}$ count $\mathrm{s}^{-1}\mathrm{arcsec}^{-2}$ (Pavlov et al., 2006) in the same energy range, despite the fact that Geminga is closer by a factor of $\sim$8. Assuming there is an undetected PWN around PSR B1916+14 having a spectrum like that of the Geminga PWN (power law with index 1.0), we can estimate the upper limit of its surface brightness to be $\sim 3 \times 10^{-17}$ erg $\mathrm{cm}^{-2}\mathrm{s}^{-1}\mathrm{arcsec}^{-2}$, in the 0.3–8 keV range. If we further assume that the PWN is uniformly distributed in a circular region of radius $20''$, then this surface brightness upper limit corresponds to a PWN luminosity upper limit of $\sim 3\times10^{31}$ erg s^{-1}.

Geppert et al. (2004) showed that the presence of a very high magnetic field could cause inhomogeneous thermal conductivity in the neutron star crust and lead to the formation of hot spots on the neutron star surface. It could also cause strong radiative beaming of the thermal emission from the neutron star. These effects could give rise to highly pulsed X-rays, as in the $74 \pm 14\%$ pulsed fraction observed from the high-magnetic-field radio pulsar PSR J1119−6127 (Gonzalez et al., 2005). However, limited by the exposure time of the observation, we did not detect any X-ray pulsations from PSR B1916+14. Future longer observations will be useful for better constraining its pulsed fraction.

5.4 Summary

In this Chapter, the first X-ray detection of the high magnetic field radio pulsar PSR B1916+14 is reported. If magnetic-field decay heating (see Section 1.3) is present in this pulsar, it would most likely result in a higher surface temperature than what one would expect from initial cooling and return-current heating, given its age and low spin-down power. The X-ray spectrum of the pulsar can be well fitted with an absorbed blackbody with temperature in the range of 0.08-0.23 keV, or a neutron-star hydrogen atmosphere model with best-fit effective temperature of ∼0.10 keV, higher than expected from fast cooling models. However, because of the limited number of photons collected in our observation, the origin of the likely thermal emission is not well constrained by our short observation and is consistent with initial cooling or return-current heating. We found no pulsations in these data and set a 1σ upper limit on the pulsed fraction in the 0.1–2 keV band of ∼0.7. A deeper observation is needed in order to test for the presence of any magnetic-field decay heating.

6

Chandra Observations of the High-B RPP J1718−3718

The content of this Chapter is reported in the paper "*Chandra* Observations of the High-Magnetic-Field Radio Pulsar J1718−3718" published in the *Astrophysical Journal* (Zhu et al., 2011).

6.1 Introduction

As in the last Chapter, we aim to test the magnetic-field decay theory for the high-B pulsars by using X-ray observations. PSR J1718−3718 is a 3.3-s radio pulsar discovered in the Parkes Multi-beam Survey (Hobbs et al., 2004). It has very high magnetic field ($B = 7.4 \times 10^{13}$ G; second highest of all known RPPs, higher than that of AXP 1E 2259+586[1]), a relatively low $\dot{E} = 1.6 \times 10^{33} \mathrm{erg\,s^{-1}}$ and a characteristic age $\tau_c \equiv P/(2\dot{P}) = 34$ kyr. All of these make it a good target to search for thermal emission caused by the decay of the magnetic field.

PSR J1718−3718 has a DM of 373 $\mathrm{cm^{-3}pc}$ (Hobbs et al., 2004). Based on the DM and the NE2001 model (Cordes & Lazio, 2002), the best-estimated distance to the pulsar is ∼4.5 kpc. However, the NE2001 model provides a poor estimate of pulsars' distances when they are near the Galactic center (Gaensler et al., 2004). Indeed the distances estimated based on NE2001 for pulsars in the nearby clusters NGC[2] 6221 and NGC 6403 are a factor of ∼2–3 smaller than their true distances (Gaensler et al., 2008). Therefore, we suggest that the true distance of PSR J1718−3718 is probably in the range ∼4.5–10 kpc.

---

[1] http://www.physics.mcgill.ca/∼pulsar/magnetar/main.html

[2] New General Catalog (NGC)

An X-ray source was serendipitously detected at the radio position of PSR J1718−3718 in a 2002 *Chandra* observation. Kaspi & McLaughlin (2005) found that this X-ray source had a soft, thermal-like spectrum, and therefore is the likely X-ray counterpart of the radio pulsar. However, due to the limited photon statistics (see Table 6.1), the spectral results were not very constraining. Also the coarse time resolution (3.24 s) in the timed exposure mode observation prevented any pulsations from being detected. Deeper *Chandra* observations with higher time resolution were proposed and conducted in 2009. Interestingly, a large period glitch occurred between 2007 September and 2009 January (Manchester & Hobbs, 2011). Four *Chandra* X-ray observations, each separated by ∼ 2 months, were taken in the hope of detecting X-ray variability, possibly associated with the glitch, as occurred in the 2006 outburst of PSR J1846−0258 (Kuiper & Hermsen, 2009; Livingstone et al., 2010, e.g.).

Here we report on a temporal analysis of the four new *Chandra* observations of PSR J1718−3718, as well as on a spectral analysis which also includes the archival 2002 observation.

6.2 Observations and Results

Four observations of PSR J1718−3718 were taken with the *Chandra X-ray Observatory* (see Section 2.4) in 2009. Each had ∼33 ks of live time (see Table 6.1 for details). In these observations, the pulsar was positioned on the Advanced CCD Imaging Spectrometer (ACIS, Garmire et al. 2003) S3 chip with Y-offset of $0\farcm1$ and Z-offset of $0\farcm18$ from the aim point. The other ACIS chips were turned off. The data were taken in 1/8 subarray mode (only photon events from 1/8 of the CCD were read out in this mode), in order to achieve time resolution of 0.44 s, sufficient for timing this 3.3-s pulsar. In the 2002 observation, the pulsar was detected on the S2 chip of ACIS $\sim 8'$ off the aim point, with a total of 99 counts in the 0.8–2.0 keV band (Table 6.1; Kaspi & McLaughlin 2005).

We started our analysis with the level 2 event files, which are the products of the standard reprocessing III [1], and analyzed the data using the tools provided in `CIAO`[2] version 4.2 (`CALDB` version 4.2.0).

6.2.1 Imaging and Source Position

PSR J1718−3718 was detected in all five observations using the `celldetect` tool in `CIAO`. The best source positions as reported by `celldetect` were slightly different from one observation to another (Table 6.1). This is the result of the small pointing uncertainty of the *Chandra* satellite. We found the average source position to be R.A.=17:18:09.83(1) and Decl.= −37:18:51.5(2) (J2000), where the uncertainties are the standard deviation of the detected positions.

To look for extended emission, we compared the image of PSR J1718−3718 from each observation with a simulated point-source image generated by the *Chandra* ray tracer[3] (ChaRT, a.k.a the *Chandra* point-spread-function[PSF] simulator) and the `MARX`[4] tool in `CIAO 4.2`. We used ChaRT to produce a collection of rays that come from a point source of the same spectrum as PSR J1718−3718 (see §6.2.2). Then we employed `MARX` to project the rays onto the detector where PSR J1718−3718 was located. For the above-mentioned images, we removed the effect of pixel randomization[5] to improve their sharpness. The PSF broadening caused by the aspect reconstruction errors and ACIS pixelization were modeled by setting the `DitherBlur` parameter to $0\farcs2$ in `MARX`. We did not find any significant difference in the radial profile between the actual images of PSR J1718−3718 and the simulated images. We also aligned and merged all four PSR J1718−3718 images from the 2009 observations to a single image, using the `reproject_events` and `dmmerge` tools in `CIAO 4.2`. Again, no significant difference was found between the point source's radial profile in the merged image and in the simulated image. In summary, we found no evidence of extended emission in the 2009 *Chandra* observations of PSR J1718−3718 .

---

[1] http://cxc.harvard.edu/ciao/repro_iii.html

[2] http://cxc.harvard.edu/ciao/

[3] http://cxc.harvard.edu/chart/

[4] http://space.mit.edu/CXC/MARX/

[5] http://cxc.harvard.edu/ciao/why/acispixrand.html

Table 6.1. *Chandra* Observations of PSR J1718−3718

ObsID	Date	MJD	Frame Time (s)	Offset[a]	Live Time (ks)	R.A., Decl.[b](deg)	N_{src}, N_{bkg}[c]	Count Rate (s^{-1})	Flux[d]
2785	2002 May 13	52407	3.24	$8'.13$	55.7	259.54098(8),−37.31437(6)	99, 5	0.0017(2)	9(2)
10131	2009 Feb 19	54881	0.44	$0'.07$	32.0	259.54098(1),−37.31419(1)	81, 0.8	0.0025(3)	8(3)
10766	2009 May 15	54966	0.44	$0'.07$	33.3	259.54096(1),−37.31439(1)	82, 0.6	0.0024(3)	9(2)
10767	2009 Jul 28	55040	0.44	$0'.07$	34.2	259.54088(1),−37.31432(1)	66, 0.9	0.0019(2)	5(2)
10768	2009 Oct 23	55127	0.44	$0'.07$	34.1	259.54093(1),−37.31432(1)	73, 1	0.0021(3)	7(2)

[a] The pointing offset from PSR J1718−3718 .

[b] Position of the X-ray counterpart of PSR J1718−3718 reported by the `CIAO celldetect` tool. Numbers in parentheses are 1σ uncertainties in the last quoted digit. The uncertainties listed in this column were calculated using the source detection code, and are much smaller than the pointing uncertainty of *Chandra* .

[c] Total counts N_{src} and estimated background counts N_{bkg} in the source region in 0.8–2.0 keV.

[d] 0.8–2.0 keV absorbed flux in units of $10^{-15}\mathrm{erg\,s^{-1}cm^{-2}}$, measured from a joint fit of the spectra with N_{H} and kT fixed at their best-fit values.

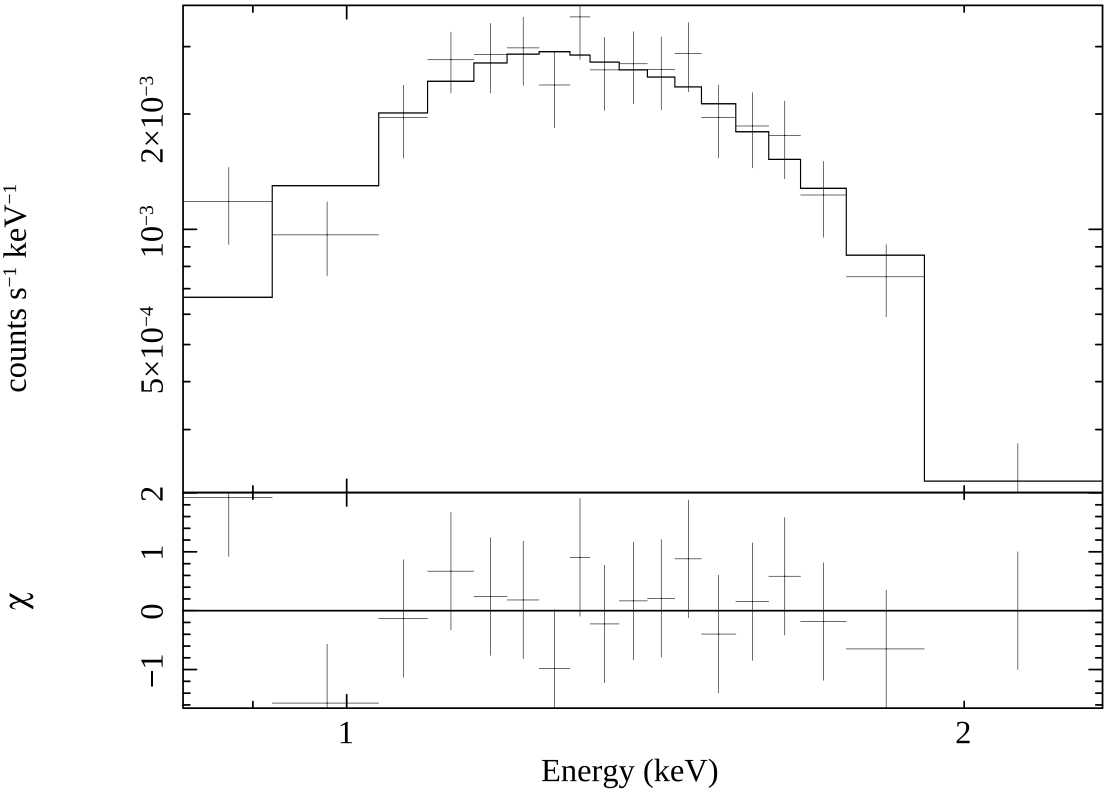

Figure 6.1 Summed *Chandra* ACIS spectrum of all five observations of PSR J1718−3718. The spectra are binned to contain a minimum of 20 counts per bin. The solid curve is the best-fit absorbed blackbody model. The χ in the bottom plot is defined as the difference between the value of the spectral bin and the model prediction, divided by the uncertainty of the spectral bin.

6.2.2 Spectroscopy

We extracted the spectrum of the pulsar from all five observations using the `psextract` script of `CIAO` 4.2. For the 2009 observations, we used a source region of radius $3''$. A source region of radius $9\overset{''}{.}8$ was used for the 2002 observation because the source was offset from the center of the field of view, where the PSF is broader. The background spectra were extracted from four circular regions of radius $10''$ centered around the pulsar for all the observations. The resulting source and background spectra were then combined with RMF and ARF files generated using `psextract` and grouped with a minimum of 15 counts per bin. We found that the spectra of the pulsar are soft, with very few counts above 2.0 keV. Thus for the following spectral analysis we used only the 0.8–2.0 keV band.

We fitted the five spectra separately with an absorbed blackbody model using `XSPEC`[1] version 12.5.0. In each source spectrum, there are 66–99 total counts in 0.8–2.0 keV (Table 6.1), so the best-fit model parameters could not be well constrained when fitting one spectrum at a time. We fitted all five spectra jointly with a single blackbody model, and found a good fit with a reduced χ^2 of 0.97 for 16 degrees of freedom. In a second joint fit, we allowed the normalization parameter to vary from observation to observation while fixing $N_{\rm H}$ and kT^{∞} at their best-fit values, and found that the inferred 0.8–2.0 keV absorbed fluxes were consistent with being constant (Table 6.1). This suggests that there are no statistically significant spectral or flux variations from observation to observation. Based on the 0.8–2 keV absorbed fluxes, we estimate a 3σ upper limit of 60% on any flux variations.

Because the individual spectra have very few spectral bins after grouping, hence poor spectral resolution, they cannot constrain the model parameters well. In order to mitigate this problem, we summed the five spectra into a single spectrum. The resulting summed spectrum was grouped with a minimum of 20 photons per bin, and had 18 spectral bins in 0.8–2.0 keV. The spectral resolution of the summed spectrum is much better than those of the individual spectra.

---

[1] http://heasarc.nasa.gov/docs/xanadu/xspec/

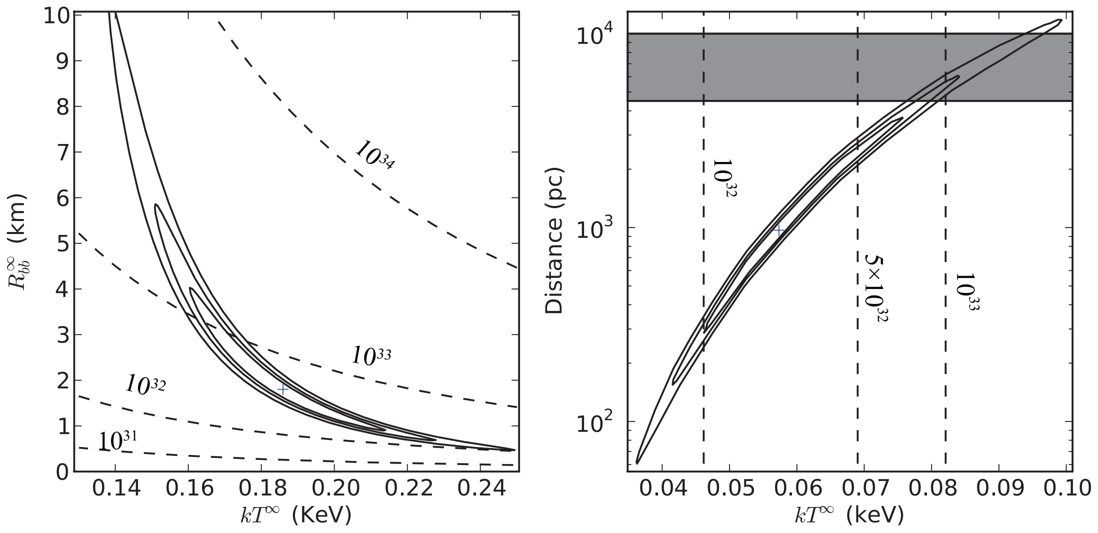

Figure 6.2 Left panel: 68%-, 90%- and 99%-confidence contours of R_{bb}^{∞} (assuming a fiducial distance of 4.5 kpc) and kT^{∞} from blackbody fitting. Right panel: confidence contours of pulsar distance and kT^{∞} from fitting with the NSA model with $B = 10^{13}$ G, assuming the neutron star radius $R = 10$ km ($R^{\infty} = 13$ km). The dashed lines in both panels are the contours of constant bolometric luminosity in units of erg s^{-1}. The shaded area in the right panel marks the region for which the pulsar's distance is 4.5–10 kpc.

We fitted the summed spectrum with a blackbody model, neutron star atmosphere model (NSA; Pavlov et al., 1995; Zavlin et al., 1996) and a power-law model, using the `wabs` model for interstellar absorption. Figure 6.1 shows a plot of the summed spectrum with the best-fit absorbed blackbody model.

We found a best-fit blackbody temperature of 186^{+19}_{-18} eV, corresponding to a blackbody radius of $1.8^{+1.7}_{-0.5}d_{4.5}$ km and a bolometric luminosity of $4^{+5}_{-2} \times 10^{32} d_{4.5}^{2}$ erg s^{-1} (assuming a fiducial distance d of 4.5 kpc). In order to explore the confidence range of the red-shifted temperature kT^{∞} and radius R_{bb}^{∞} for the blackbody model, we plotted their confidence contours in the left panel of Figure 6.2. This indicates the lowest possible kT^{∞} of 140 eV, corresponding to R_{bb}^{∞} ≈10 km and $L_{\rm bol}^{\infty} \approx 5 \times 10^{33}$ erg s^{-1} (higher than $\dot{E} = 1.6 \times 10^{33}$ erg s^{-1} of the pulsar).

The NSA model assumes that the X-ray emission of the pulsar comes from its entire surface. The best-fit local surface temperature kT is only 75^{+16}_{-10} eV ($kT^{\infty} = 57^{+12}_{-7}$ eV as seen from Earth), with a best-fit distance of $1.2^{+1.4}_{-0.7}$ kpc (much smaller than the estimated range of 4.5–10 kpc) assuming the neutron star has mass $1.4\,M_{\odot}$ and local radius 10 km. The best-fit parameters of the blackbody and NSA models are listed in Table 6.2. The highly magnetized NSA model assumes a B field of 10^{13} G, less than the inferred B of 7.4×10^{13} G for PSR J1718−3718 . We allowed the normalization parameter, which corresponds to $1/d^2$, where d is the distance of the neutron star, to vary when fitting the spectrum. We plot the confidence contours of the red-shifted effective surface temperature kT^{∞} and distance in Figure 6.2, right panel. Assuming the pulsar is at a distance between 4.5 kpc and 10 kpc, it should have a surface temperature between 75 eV and 97 eV and a bolometric luminosity $\gtrsim 10^{33}$ erg s^{-1}.

The best-fit absorbed power-law model has an unreasonably large photon index (> 8); therefore, we consider it no further. We also tried to fit the 0.8–10.0 keV summed spectrum with a Resonant Cyclotron Scattering model (RCS; (Rea et al., 2008)), but did not find a good fit (best reduced $\chi^2 = 2.4$ for 15 degrees of freedom); this is likely due to the lack of hard photon events in the source spectrum.

6.2.3 Variability and Pulse Profile

We adjusted the time stamps of the source events from all five observations to the solar system barycenter time using the `axbary` tool in `CIAO`. We binned the photon events of energy between 0.8 and 2.0 keV from the five observations evenly in time with 3.4 hr per bin. The resulting count rates were consistent with being constant with a 3σ upper limit of 48% on variations, therefore showing no evidence of significant variability on timescales of 3–9 hr. In order to look for variability on shorter timescales, we measured the intervals between the arrival times of every two photons in each observation. We found that they are consistent with the exponential distribution expected from a constant count rate, and therefore, show no evidence of flux variations.

Unlike the 2002 normal timed exposure mode observation that has time resolution 3.24 s, the later four 1/8 subarray observations have 0.44 s time resolution (Table

Table 6.2. Spectral models for PSR J1718−3718 and their best-fit parameters.

Parameters	Blackbody	Hydrogen Atmosphere[a]
N_H (10^{22} cm^{-2})	1.3 ± 0.2	$1.7^{+0.1}_{-0.2}$
kT^{∞} (eV)	186^{+19}_{-18}	57^{+12}_{-7}
R^{∞} (km)	$1.8^{+1.7}_{-0.5} d_{4.5}$	13 (fixed)
Distance[b] (kpc)	$\cdots$	$1.2^{+1.4}_{-0.7}$
$f_{\rm abs}$[c] (10^{-13} erg s^{-1} cm^{-2})	0.078 ± 0.004	0.077 ± 0.004
$f_{\rm unabs}$[d] (10^{-13} erg s^{-1} cm^{-2})	$0.7^{+0.4}_{-0.2}$	0.80 ± 0.04
L_X[e](10^{32} erg s^{-1})	$4^{+5}_{-2} d^2_{4.5}$	2^{+3}_{-1}
$\chi^2_{\nu}(\nu)$	0.7(15)	0.7(15)

[a] The NSA model for pulsar with $B = 10^{13}$ G and a pure hydrogen atmosphere. The values of neutron star surface temperature and radius $R = 10$ km were redshifted for observers at infinite distance according to $T^{\infty} = T(1-2GM/Rc^2)^{1/2}$ and $R^{\infty} = R(1-2GM/Rc^2)^{-1/2}$ with M fixed at $1.4M_{\odot}$.

[b] In the blackbody fit, a fiducial distance d of 4.5 kpc is used as a scaling factor for the best-fit parameters. In the NSA fit, distance is fitted.

[c] Absorbed X-ray flux in 0.8–2.0 keV.

[d] Unabsorbed X-ray flux in 0.8–2.0 keV.

[e] Bolometric luminosity. For the NSA model, it is calculated based only on the pulsar's best-fit surface temperature, and does not depend on distance. However, the best-fit distance in this fit is unreasonably small. If a more reasonable distance were assumed, the resulting best-fit temperature would likely become larger and thus imply a higher bolometric luminosity.

6.1) and therefore could be used to search for pulsations from this 3.3-s pulsar. We folded the events with energies between 0.8 and 2.0 keV from the 2009 observations into 8 phase bins based on a timing ephemeris obtained using the Parkes telescope (Manchester & Hobbs, 2011). The resulting pulse profile is shown in Figure 6.3. Significant pulsations are detected. We found the H test (de Jager, 1994) value of the summed profile is 44.5 and the best-fit reduced χ^2 is 7.0 for 7 degrees of freedom. Both correspond to null-hypothesis possibilities of $\sim 2 \times 10^{-8}$, clearly excluding the null hypothesis. We also measured an area pulsed fraction (the fractional counts above the minimum; Gonzalez et al. 2010) of 52%±13% in the 0.8–2.0 keV band and a max-min pulsed fraction $(N_{\rm max} - N_{\rm min})/(N_{\rm max} + N_{\rm min})$ of 60%±13%.

In Figure 6.3, we also plot the folded pulse profiles from individual observations. Not all of them were significantly pulsed. For instance, when fitted with a constant, the pulse profile of the 2009 February 19 observation gives a best-fit reduced χ^2 of 0.9 for 7 degrees of freedom and a H value of 3, which do not exclude the null hypothesis (Table 6.3). Through numerical simulations, we have verified that with only 81 counts and assuming Poisson noise, it is possible for a source having 52% pulsed fraction to produce a pulse profile of such low significance. We simulated 10000 pulse profiles with a source with area pulsed fraction of 52%, and found that 209 of them show lower pulse significance than in the February 19 observation. Thus, even if the pulsar's profile did not change between 2009 February 19 and July 28, there is ~2% chance of observing a pulse profile similar to the February 19 one. Taking the number of trials into account, the low pulse significance of this observation does not provide strong evidence for a change in the pulsed fraction.

We fitted the X-ray pulse profile with a sinusoidal function to find its peak phase and compared it with that of the radio pulse after correcting for the effect of dispersion due to the interstellar medium. The radio pulse leads X-ray pulse by 0.01 ± 0.03 in phase. Thus, they are consistent with being aligned.

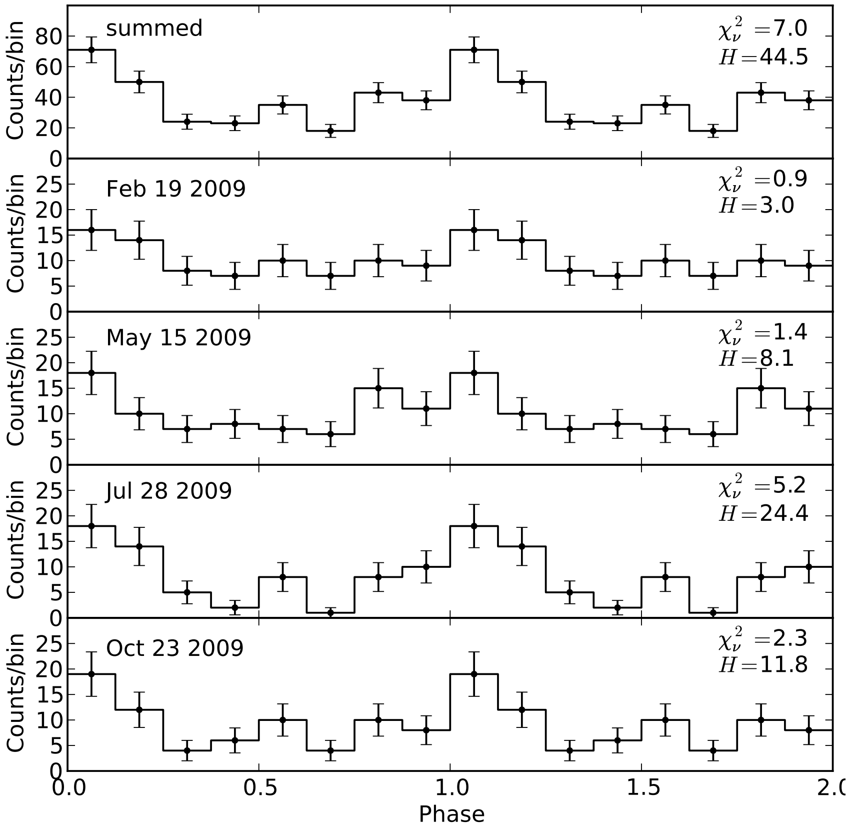

Figure 6.3 Pulse profiles for PSR J1718−3718 in the 0.8–2.0 keV energy range. Also given in the plot are the reduced χ^2 values for 7 degrees of freedom from fitting the profile with a constant. The peak of the pulsar's radio pulse aligns with zero phase in this plot.

Table 6.3. Significance of the X-ray pulsations of PSR J1718−3718 .

Observation	χ^2	$P_{\rm null}^{\chi^2}$	H value	$P_{\rm null}^{H}$
Summed	49.0	2×10^{-8}	44.5	2×10^{-8}
2009 Feb 19	6.2	0.5	3.0	0.3
2009 May 15	10.1	0.2	8.1	0.04
2009 Jul 28	36.6	6×10^{-6}	24.4	6×10^{-5}
2009 Oct 23	16.2	0.02	11.8	0.009

6.3 Discussion

We have reported on four new *Chandra* observations, plus a reanalysis of one archival observation, of the young, high-B rotation-powered pulsar PSR J1718−3718. We found no evidence of magnetar-like flux variability in PSR J1718−3718 from our *Chandra* observations, and set a 3σ upper limit on any flux variability of 60% in the 0.8–2 keV band. However, the possibility that a magnetar-like outburst, such as that observed from PSR J1846−0258 in 2006 which lasted for only few weeks, happened in the span of our observations could not be ruled out.

PSR J1718−3718 's X-ray spectrum is soft and thermal, and is well fit by a blackbody model. Fitting its summed spectrum with a blackbody model, we found a high blackbody temperature of 186^{+19}_{-18} eV (Table 6.2), and a corresponding best-fit blackbody radius of $1.8^{+1.7}_{-0.5} d_{4.5}$ km. Such an emission radius is consistent with radiation from hot spots. However, it is not consistent with polar caps heated by return currents because of the unusually high X-ray efficiency ($L^{\infty}_{bb}/\dot{E} = 0.3 d^{2}_{4.5}$). By contrast, models for polar-cap heating predict that no more than $\sim 10^{-3}$ of the spin-down luminosity should be converted to thermal radiation (Harding & Muslimov, 2001). Note that if the distance is larger than 4.5 kpc, this conclusion is only strengthened. Indeed at 10 kpc, $L^{\infty}_{bb} > \dot{E}$. Based on the confidence contours of kT^{∞} and R^{∞}_{bb} (left panel of Figure 6.2), we cannot completely exclude a blackbody fit of $kT^{\infty} = 140$ eV and $R^{\infty}_{bb} = 10 d_{4.5}$ km. However, the measured 52%±13% area pulsed fraction suggests that the surface temperature of the pulsar cannot be uniform. Given the pulsar's spin-down age of 34 kyr, a surface temperature of 140 eV is still higher than what one would expect (60–90 eV, Page et al., 2006) from a minimum cooling model for the neutron star surface without considering the effects of the magnetic field. Interestingly, the 186 eV best-fit blackbody temperature is similar to those found for the high-B PSRs J1119−6127, J1734−3333, J1819−1458 (see Table 6.4 for details and references) and the transient AXP XTE J1810−197 when it was in quiescence between 1980 and 1993 (Gotthelf et al., 2004b, $kT^{\infty} = 180 \pm 10$ eV).

On the other hand, fitting the spectrum with a NSA model leads to a best-

Table 6.4. Surface temperatures measured for high-B pulsars, normal pulsars, and XINSs.

PSR	τ_c(kyr)	B (G)	kT^{∞}_{bb}(eV)	R^{∞}_{bb}(km)[D(kpc)]	$L^{\infty}_{bb}/\dot{E}^{\sharp}$	references
B0950+08	18000	2.4×10^{11}	<41.0	10[0.3]	<0.06	Becker et al. 2004
B1929+10†	3100	5.2×10^{11}	300^{+20}_{-30}	$0.033^{+0.006}_{-0.005}$[0.4]	3×10^{-4}	Misanovic et al. 2008
J0538+2817	40	7.3×10^{11}	181 ± 3	2.23 ± 0.01[1.5]	0.01	Ng et al. 2007
B0355+54†	564	8.4×10^{11}	200^{+96}_{-70}	$0.12^{+0.16}_{-0.07}$[1.0]	7×10^{-5}	McGowan et al. 2007
B0823+26	4900	9.6×10^{11}	<43.0	10[0.3]	<0.10	Becker et al. 2004
B1055−52	535	1.1×10^{12}	68 ± 3	$12.3^{+1.5}_{-0.7}$[0.8]	0.01	De Luca et al. 2005
J0633+1746	342	1.6×10^{12}	41.4 ± 0.1	9 ± 1[0.2]	9×10^{-4}	De Luca et al. 2005
J1811−1925	23	1.7×10^{12}	<150	10[5.0]	<0.001	Kaspi et al. 2006
J1740+1000	114	1.8×10^{12}	70^{+10}_{-20}	7.0[1.4]	7×10^{-4}	Misanovic et al. 2011
B1823−13	21	2.8×10^{12}	97^{+4}_{-5}	6.3[4.0]	2×10^{-4}	Pavlov et al. 2008
B1706−44	18	3.1×10^{12}	143 ± 14	3.6 ± 0.9[2.5]	2×10^{-4}	Gotthelf et al. 2002
B0833−45	11	3.4×10^{12}	93 ± 3	$5.1^{+0.4}_{-0.3}$[0.3]	4×10^{-5}	Manzali et al. 2007
B1046−58	20	3.5×10^{12}	<95.0	10[2.7]	$<5 \times 10^{-4}$	Gonzalez et al. 2006
J0205+6449	2.4	3.6×10^{12}	112 ± 9	11[3.2]	9×10^{-5}	Slane et al. 2004
B0531+21	0.96	3.8×10^{12}	<172	16[1.7]	$<6 \times 10^{-5}$	Weisskopf et al. 2004
B0656+14	111	4.7×10^{12}	56.0 ± 0.9	21^{+3}_{-4}[0.3]	0.01	De Luca et al. 2005
J1357−6429†	7.3	7.8×10^{12}	160^{+40}_{-30}	1.0[4.1]	3×10^{-5}	Chang et al. 2011
B2334+61	41	9.9×10^{12}	109 ± 35	1.7[3.1]	8×10^{-4}	McGowan et al. 2006
J1856−3754*	3800	1.5×10^{13}	63.5 ± 0.2	6.2 ± 0.1[0.2]	24	Burwitz et al. 2003
B1916+14	88	1.6×10^{13}	130^{+100}_{-50}	0.8 ± 0.1[2.1]	0.005	Zhu et al. 2009
J2143+0654*	3700	2.0×10^{13}	104 ± 4	3.1[0.4]	76	Kaplan & van Kerkwijk 2009b
B0154+61	197	2.1×10^{13}	<73.0	10[1.7]	<0.6	Gonzalez et al. 2004b
J0720−3125*	1900	2.5×10^{13}	90 ± 4	6.4[0.4]	73	Haberl et al. 2006
J0806−4123*	3300	2.5×10^{13}	87 ± 11	1.3[0.2]	8	Kaplan & van Kerkwijk 2009a
J0847−4316	790	2.7×10^{13}	<100	10[3.4]	<58	Kaplan et al. 2009
J1846−0257	442	2.7×10^{13}	<120	10[5.2]	<38	Kaplan et al. 2009
J1308+2127*	1500	3.4×10^{13}	100 ± 2	4.1[0.5]	54	Schwope et al. 2007
J1119−6127	1.8	4.1×10^{13}	210 ± 10	2.7 ± 0.7[8.4]	8×10^{-4}	Safi-Harb & Kumar 2008
J0420−5022*	109	4.2×10^{13}	45 ± 3	3.3[0.3]	0.01	Haberl et al. 2004
J1846−0258	0.88	4.9×10^{13}	<250	2.7[6.0]	$<5 \times 10^{-4}$	Livingstone et al. 2011
J1819−1458	117	5.0×10^{13}	120 ± 20	2.1 ± 0.4[3.6]	0.4	Rea et al. 2009a
J1734−3333	8.1	5.2×10^{13}	250^{+130}_{-80}	1^{+3}_{-1}[6.1]	0.01	Olausen et al. 2010
J1814−1744	85	5.5×10^{13}	···	···	···	Pivovaroff et al. 2000
J1718−3718	34	7.4×10^{13}	189^{+15}_{-22}	$1.8^{+1.7}_{-0.6}$[4.5]	0.3	This work
J1847−0130	83	9.4×10^{13}	···	···	···	McLaughlin et al. 2003

$^{\sharp}$The ratio of the pulsar's bolometric luminosity ($L^{\infty}_{bb} \equiv 1.28 \times 10^{35} (R^{\infty}_{bb})^2 (kT)^4 \mathrm{erg\ s}^{-1}$) to spin down power ($\dot{E}$).

*XINSs.

†These pulsars have very small blackbody radius $R^{\infty}_{bb} \leq 1\,\mathrm{km}$ and $L^{\infty}_{bb}/\dot{E} \leq 10^{-3}$. Their thermal radiation is likely coming from hot spots caused by return current heating. Therefore they are not included in Figure 6.4.

estimated surface temperature of 75–97 eV (assuming a neutron star mass of $1.4M_\odot$, a local radius of 10 km, and a pulsar distance of 4.5–10 kpc), consistent with standard cooling. We note, however, that the magnetic field strength assumed in the NSA model is 10^{13} G, almost one order of magnitude smaller than the spin-down-inferred value. Therefore, the results of the NSA model fit should be taken with caution.

Attempting to explain the X-ray thermal emission observed from magnetars, XINSs and some high-B pulsars, Arras et al. (2004), Pons et al. (2007) and Aguilera et al. (2008) constructed neutron-star cooling models in which pulsars with magnetic fields higher than 10^{13} G are significantly heated by field decay. The key evidence to support this theory is an intriguing possible correlation found between the pulsar's blackbody temperature T and spin-down magnetic field B ($T \propto B^{1/2}$; see Chapter 1 Equation 1.1) based on a sample of magnetars, XINSs and some RPPs (Pons et al., 2007). However, their analysis did not consider high-B RPPs. Searches for evidence of magnetic-field-decay heating have been conducted on several high-B pulsars, e.g., PSRs J1814−1744 (Pivovaroff et al., 2000), J1847−0130 (McLaughlin et al., 2003), B0154+61 (Gonzalez et al., 2004b), J1119−6127 (Gonzalez et al., 2005), J1718−3718 (Kaspi & McLaughlin, 2005), B1916+14 (Zhu et al., 2009) and J1734−3333 (Olausen et al., 2010), and X-ray counterparts were found in some cases. Their spectra, however, have not yet been sufficiently well constrained to prove the existence of significant magnetic-field-decay heating. For a recent review on high-magnetic-field pulsars, see Ng & Kaspi (2010).

With our new data and spectral analysis of PSR J1718−3718 , we are unable to confirm that it is heated by magnetic field decay. This is mainly because the non-magnetized neutron star cooling models predict a large range of surface temperatures for a given pulsar age. However, we can compare the surface temperatures of several high-B RPPs with those of normal RPPs, provided that the temperatures were measured using the same spectral model. In Figure 6.4, we plot blackbody kT^∞ versus age for a collection of pulsars including some high-B pulsars (see Table 6.4). From this plot, one can see that the blackbody temperatures of the high-B pulsars appear

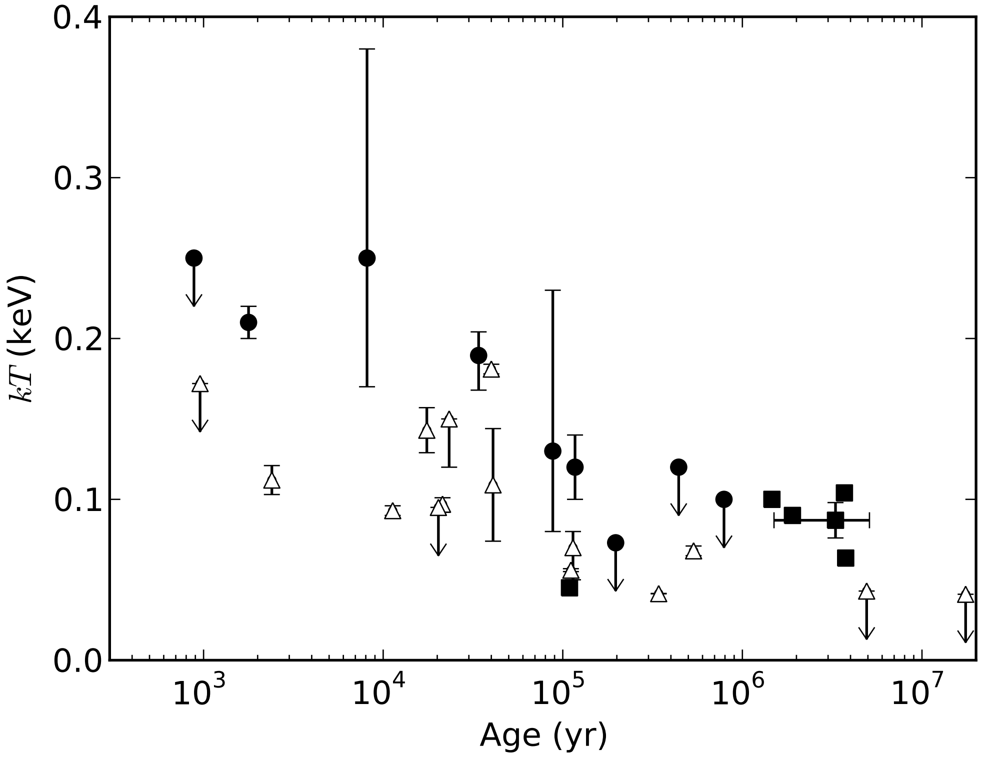

Figure 6.4 Blackbody temperatures versus characteristic ages ($P/(\dot{P}(n-1))$, where n is the measured braking index, assuming $n = 3$ if it is not measured) of high-B pulsars (filled circles), normal pulsars (open triangles), and XINSs (filled squares). References are listed in Table 6.4.

to be in general higher than those of the normal pulsars of the same age.

We also looked for the same T-B correlation showed by Pons et al. (2007) in a kT^∞ versus B plot, but the temperatures of the pulsars are too scattered to discern a trend. This could be because our sample has a small range of B but a large range of ages.

Note that three pulsars listed in Table 4 (PSRs B1929+10, B0355+54 and J1357−6449) are not plotted in Figure 6.4. This is because they all exhibit a large kT^∞ with very small blackbody radius, $R_{bb}^\infty \lesssim 1\,\mathrm{km}$, consistent with return-current heating. Return-current heating affects mostly the high-$\dot{E}$ pulsars, for example the Vela pulsar (B0833-45; $\dot{E} = 6.9 \times 10^{36}\,\mathrm{erg\,s^{-1}}$). The Vela pulsar was observed to exhibit a two blackbody spectrum, with one blackbody having best-fit $kT_{\mathrm{bb}} = 91\,\mathrm{eV}$ and $R_{\mathrm{bb}} = 5.1\,\mathrm{km}$ and the other $kT_{\rm BB} = 186\,{\rm eV}$ and $R_{\rm BB} = 0.73\,{\rm km}$ (Manzali et al., 2007). Such a pulsar, if at the same distance as PSR J1718−3718 and observed with *Chandra* for 100 ks, will show a spectrum similar to what we observed from PSR J1718−3718 . However, we argue that return-current heating is unlikely to be present from the high-B PSRs and XINSs. This is because most of them, including PSR J1718−3718 , ($B > 10^{13}\,{\rm G}$, see Table 6.4) have $\dot{E}$ much smaller than that of Vela. If their X-ray luminosity were the result of return current heating, it would imply an X-ray efficiency of $L^{\infty}_{\rm bb}/\dot{E} \gtrsim 10^{-3}$, clearly inconsistent with the current model and observations of return-current heating (Harding & Muslimov, 2001). Note that Vela-like X-ray spectra were also observed from the nearby pulsars, PSRs B1055−52, B0656+14 and J0633+1746. In these cases, only the $kT^{\infty}_{\rm bb}$ of the cool surface was used. For the other RPPs, it is possible that their blackbody temperatures are also higher because of return currents, but these sources nevertheless provide interesting upper limits on any non-return current thermal emission.

6.4 Summary

In summary, our *Chandra* observations of PSR J1718−3718 have revealed, for the first time, X-ray pulsations at the pulse period, as well as a thermal spectrum of blackbody temperature somewhat higher than for other rotation-powered pulsars having the same age. We have found a high bolometric to spin-down luminosity ratio, ∼0.3 for a distance of 4.5 kpc, and higher for more realistic, larger distances. Although we cannot rule out standard passive cooling, as a model fit with a neutron-star atmosphere model yields a lower surface temperature, we have considered the possibility that PSR J1718−3718 exhibits enhanced thermal emission due to magnetic-field decay, as predicted by models of magneto-thermal evolution (Arras et al., 2004; Pons et al., 2007; Aguilera et al., 2008). We have compiled such measurements for the other high- and low-B rotation-powered pulsars, and find a hint that those of higher B are generally hotter than low-B pulsars of the same age. However deeper observations of high- and low-B pulsars are required to confirm this possibility.

7

Conclusions

7.1 Summary

In the previous Chapters, I presented our work on the studies of two magnetars and two high-B RPPs. In order to learn more about the physics in magnetar outburst, we studied the X-ray afterglow of the AXP 1E 2259+586after its 2002 outburst (Chapter 3) using *XMM* observations. In order to find out the relation between magnetar glitch and variability, we studied the flux history of the frequently glitching AXP 1E 1841−045 based on archival X-ray data (Chapter 4). In order to study the effect of very high magnetic field on the cooling of RPPs, we studied the X-ray spectrum of the high-B RPPs B1916+14 (Chapter 5) and J1718−3718 (Chapter 6) using *XMM* and *Chandra* observations, respectively. Here I summarize the conclusions of the previous Chapters as well as some recent progress in related fields, and discuss planned and possible future observations.

7.2 Magnetar Variability

In Section 1.2.2, I introduced the twisted magnetic field model of magnetars (Thompson et al., 2002). In this model the magnetar's magnetosphere is defined by a twisted dipolar magnetic field, which induces large-scale electrical currents. This model suggests that the persistent X-ray emission of magnetars comes from the hot surface of the neutron star, additionally heated by return electrical currents in the magnetosphere, with some of the thermal photons from the stellar surface scattered to higher energy by high speed electrons in the magnetosphere through a resonant scattering process. Magnetar bursts and outbursts may be the result of sudden twisting of the external magnetic field caused by a crustal deformation or fracture. This model has been very successful in explaining many magnetar behaviours, and is continuously being refined (e.g. Beloborodov 2009).

Our paper (Zhu et al. 2008; Chapter 3) studied the long-term radiative evolution of AXP 1E 2259+586 after its 2002 outburst. 1E 2259+586 went through a major outburst in June 2002 (Kaspi et al., 2003; Woods et al., 2004). This was the first SGR-like outburst observed from an AXP. I studied the X-ray flux decay of the pulsar based on ten *XMM* observations taken before and after the outburst in a time span of more than 3 years. I found that the AXP was still hotter and brighter than pre-outburst as of mid-2005, ∼3 years after the outburst. On a time scale of several years, the AXP's flux decayed from the outburst following a power-law of index -0.69 ± 0.03, similar to those found in the flux decay of SGR 1900+14's 1998 outburst (~ -0.9; Feroci et al. 2003) and SGR 1627−41's 1998 outburst (~ -0.47; Kouveliotou et al. 2003). The power-law decay and its index are consistent with the power-law decay of index $-2/3$ predicted by Lyubarsky et al. (2002). In their magnetar outburst model, the X-ray afterglow is from the cooling of the neutron-star crust after it was heated by magnetic field energy released during the outburst.

However, not all AXP outbursts have shown the same flux decay trend. The transient AXP XTE J1810−197 exhibited an outburst in 2003. Although its pulsed flux as measured by *RXTE* was found to be decaying in a power-law of index $-0.75^{+0.22}_{-0.33}$ (Ibrahim et al., 2004), its total flux as measured by *Chandra* from 2003 to 2006 was found to be decaying exponentially with a time scale of 233.5 days (Gotthelf & Halpern, 2007). In recent years, more AXP outbursts have been observed. The AXP CXOU J164710.2−455216 exhibited an outburst on September 21, 2006. The AXP was found to have brightened by a factor of ∼ 100 (Israel et al., 2007; Woods et al., 2011) following its outburst. The AXP 1E 1547.0−5408 exhibited two outbursts in 2008 and 2009 (Ng et al., 2011) and possibly another one between 2006 and 2007 (Halpern et al., 2008). The 2006 outburst of AXP CXOU J164710.2−455216 decayed in total flux (2–10 keV, unabsorbed) following a power-law of index -0.306 ± 0.005, whereas the 2009 outburst of 1E 1547.0−5408 followed a power-law decay of index -0.21 ± 0.01. The decay trend observed from these later AXP outbursts are similar to those observed from 1E 2259+586 and the SGRs, but not as steep. It seems that Lyubarsky et al. (2002)'s cooling of the outer crust model is not sufficient to explain the X-ray afterglow of all the AXP outbursts.

I found a strong correlation between hardness and flux for 1E 2259+586 as seen in the flux evolution of other AXPs such as XTE J1810−197 (Gotthelf & Halpern, 2007), 1E 1048.1−5937 (Tam et al., 2008), 1E 1547.0−5408 (Scholz & Kaspi, 2011) and J164710.2−455216 (Israel et al., 2007). Such a correlation is expected in the twisted magnetic field model because it predicts increased scattering optical depth when the twist is larger in the magnetosphere. Note however that a similar prediction is also made by Özel & Guver (2007) in their thermally emitting magnetar model, in which the spectral hardening and flux enhancement are both the result of the magnetar's surface getting hotter, no variable magnetospheric twist were invoked, only the thermal emission from the magnetar surface and magnetospheric scattering. A detailed, more quantitative modeling of the hardness-flux correlation of each of these magnetars is needed to distinguish the two models.

In addition, an interesting correlation was found between the area pulsed fraction (PF; see Section 3.3.2 for details) and the unabsorbed flux of 1E 2259+586. A similar correlation was found from XTE J1810−197 (Gotthelf & Halpern, 2007). However, in contrast, a clear anti-correlation between PF and flux was observed from 1E 1048.1−5937 (Tiengo et al., 2005; Gavriil et al., 2006; Tam et al., 2008) and from 1E 1547.0−5408 (Ng et al., 2011). Therefore, the relation between PF and flux appears to vary from pulsar to pulsar, and probably depends on the emission geometry. Detailed modeling of magnetar outbursts and the variation of pulse profiles is being conducted (Albano et al., 2010; Zane et al., 2011); any such model will have to account for the variety of PF-flux correlations observed from AXPs.

AXPs are now established to exhibit significant X-ray variability and be prolific glitchers. For example, one of the largest glitches seen so far, from AXP 1E 2259+586, was accompanied by major radiative changes, including bursts and a factor of ∼20 pulsed and persistent flux increase (Kaspi et al., 2003; Woods et al., 2004). Dib et al. (2009) showed that glitches in AXP 1E 1048.1−5937 were also accompanied with radiative enhancements. In the context of the twisted magnetic field model (Thompson et al., 2002), these bursts and outbursts are thought to be the result of sudden yielding of the neutron-star crust to the enormous internal stresses built up because of the decay of internal magnetic field of the magnetar. However, there are also AXP outbursts that are not accompanied by rotational anomalies such as glitches. For instance, the 2006 outburst of the AXP CXOU J164710.2−455216 (Woods et al., 2011) has been shown to be consistent with no glitch having occurred, in spite of early claims otherwise (Israel et al., 2007). An open issue is whether AXP glitches are generically accompanied by radiative changes. This is highly relevant for understanding magnetar physical properties. In our paper (Zhu & Kaspi 2010; Chapter 4), I reported on an analysis of archival X-ray data from the AXP 1E 1841−045, obtained between 1993 and 2007. This AXP has exhibited three glitches between 2002 and 2007, as determined by *RXTE* monitoring since 1999. I searched for evidence of phase-averaged flux variability that could be present if glitches in AXPs are usually accompanied by radiative changes. I found no evidence for glitch-correlated flux changes from this source between 1999 and 2007, supporting the existence of radiatively silent glitches in AXPs. This suggests that the glitches of AXPs do not necessarily always result in significant energy release in the neutron star crust or magnetosphere. A more detailed discussion on how this finding impacts our understanding of AXP glitches is provided in the discussion section of Chapter 4.

Interestingly, a SGR-like burst from 1E 1841−045 was detected by *Swift* on May 6, 2010 (Kumar & Safi-Harb, 2010). A factor of 2 increase in the total flux was found in a 0.5-hr post-burst *Swift*-XRT observation. A burst like this one, had it not been detected by *Swift* (launched in 2004; Section 2.1) and without the post-burst flux enhancement lasting for more than a few months, would not have been detected in our searching.

7.3 High-B PSRs

As I introduced in Section 1.1.2, the observational manifestations of the neutron-star population are remarkably diverse. There are the most common RPPs, the rare XINSs, and the luminous magnetars. Different classes of pulsars have distinctive observational properties and behaviours, linking to different physical conditions or sources of power. The RPPs and the magnetars are the two extremes of pulsars, one powered by rotational energy and the other by magnetic energy. Recent studies of the XINSs (Kaplan & van Kerkwijk, 2009a) showed that their X-ray luminosities are comparable to or higher than their spin-down power and significantly higher than those of the normal RPPs of the same characteristic age. In the mean time, models of neutron-star magneto-thermal evolution (Arras et al., 2004; Pons et al., 2007; Aguilera et al., 2008) have been proposed, suggesting a connection between XINSs' high surface temperature and their apparent higher ($\sim 10^{13}$ G) spin-down magnetic fields. These models further suggest that the XINSs can be explained as the evolutionary outcome of magnetars or high-B pulsars. Kaspi (2010) pointed out that, if these models were right, then the family of isolated neutron stars could be united by a primary defining parameter – the magnetic field of the neutron star. As a test of this idea of unification, we should expect to find common properties of the RPPs and magnetars in their "in-betweens," the high-B RPPs. This is the motivation behind the decade-long X-ray observation campaign of the high-B pulsars conducted by the McGill pulsar group. Our papers on PSR B1916+14 (Zhu et al. 2009; Chapter 5) and PSR J1718−3718 (Zhu et al. 2011; Chapter 6) are part of this campaign. For a general introduction of X-ray observations of high-B pulsars, please see Section 1.3.

In my paper on *XMM* X-ray observations of the high-B PSR B1916+14 (Zhu et al. 2009; Chapter 5), I reported the first X-ray detection of this source. I found a surface temperature of 0.08–0.23 keV for the pulsar when fitting its X-ray spectrum with a blackbody model, and an effective temperature of $\sim 0.10\,\mathrm{keV}$ when fitting with a hydrogen neutron star atmosphere model (NSA). I found no significant pulsations and set a 1σ upper limit of 0.7 on pulsed fraction. Deeper observations are needed in order to constrain the pulsar's cooling history or detect its pulsations.

In my paper on *Chandra* observations of the high-B PSR J1718$-$3718 (Zhu et al. 2011; Chapter 6), based on five *Chandra* observations of total $\sim 160\,\mathrm{ks}$ exposure time, I found a blackbody temperature of $186^{+19}_{-18}\,\mathrm{eV}$, and bolometric luminosity of $L^{\infty}_{bb} = 4^{+5}_{-2} \times 10^{32}\,\mathrm{erg\,s^{-1}} \sim 0.3\dot{E}$ for a distance of 4.5 kpc. I also detected, for the first time, X-ray pulsations at the pulsar's period, with a pulsed fraction of 52%±13%. The blackbody temperature is slightly higher than predicted by standard neutron star cooling models, however, the effective surface temperature when fitting the spectrum with a NSA model is still consistent with standard cooling.

I compiled measurements of the blackbody temperatures of all X-ray detected high-B RPPs (including our measurement of PSR B1916+14) as well as those of low-B RPPs, except for a few pulsars of which thermal emission is obviously dominated by return current heating. We find, for the first time, suggestive evidence for the former being on average hotter than the latter (see Figure 6.4). If this is true, it suggests that the cooling of high-B pulsars may be delayed by the presence of high magnetic fields as predicted in the magneto-thermal evolutionary model, and that they might evolve into one of the XINSs in $\sim 10^6$ yr. Future deeper X-ray observations of more high-B pulsars are needed to confirm this.

7.4 Concluding Remarks

This thesis was written in an exciting era of X-ray astronomy. Thanks to the excellent observational quality in timing, imaging, and spectroscopy of *RXTE*, *Chandra*, *XMM*, *Swift* and other observatories, lots of new and diverse phenomena were observed from magnetars, and more detailed theoretical models are being developed. Our work on AXP outbursts and variability is part of this endeavor. Similarly our observations of high-B RPPs are part of a long-term campaign to study the influence of very high magnetic fields in RPPs. But because the RPPs are not usually very luminous, they take long and deep observations to observe, and our group cannot get the required observing time on them all at once. However, with the help of the next generation X-ray mission which will probably have several times more collecting area than *XMM* , we should be able to constrain the temperatures for most high-B pulsars well enough to conclude on whether they are truly hotter than the low-B ones. In the mean time, a target of opportunity observation plan has been undertaken by Prof. Kaspi, in which a list of high-B pulsars will be monitored regularly at radio wavelength to detect any big glitches from them; and once a glitch is detected, an X-ray observation of the pulsar will be triggered to look for glitch-related X-ray variability as seen in some AXPs and RPPs (PSR J1846$-$0258; Section 1.3), although, as we have shown, this does not always happen (1E 1841$-$045 ; Chapter 4). These efforts may help further establish the connection between the RPPs and magnetars, and bring us one step closer to the 'grand unification' of neutron stars.

Appendix

List of Acronyms

ACIS Advanced CCD Imaging Spectrometer (*Chandra*; Garmire et al. 2003) v

ARF Auxiliary Response File 72

ASM All Sky Monitor (*RXTE*; (Levine et al., 1996)) 32

ATHENA Advanced Telescope for High Energy Astrophysics 34

ATNF Australia Telescope National Facility 2

AXP Anomalous X-ray Pulsar vii

BAT Burst Alert Telescope (*Swift*) 31

CCD Charge Coupled Device 30

DM Dispersion Measure 26

EOS Equation of State 4

EPIC European Photon Imaging Camera (*XMM*) 37

FOV Field of View 31

FWHM Full Width of Half Maximum 37

GIS Gas Imaging Spectrometer (*ASCA*) 31

GRB Gamma-ray Burst 12

HETG High Energy Transmission Grating (*Chandra*) 34

HEXTE High Energy X-ray Timing experiment (*RXTE*) 32

HRC High Resolution Camera (*Chandra*) 34

IR infrared 50

IXO International X-ray Observatory 34

LETG Low Energy Transmission Grating (*Chandra*) 34

LMC Large Magellanic Cloud 12

MJD Modified Julian Date 53

NGC New General Catalog 100

NSA Neutron Star Atmosphere model 25

PCA Proportional Counter Array (*RXTE*) 32

PCU Proportional Counter Unit (*RXTE*) 54

PSF Point Spread Function 37

PWN Pulsar Wind Nebula 24

RCS Resonant Cyclotron Scattering model 107

RGS Reflecting Grating Spectrometer (*XMM*) 34

RMF Redistribution Matrices File 72

RPP Rotation-powered Pulsar vii

RRAT	Rotating Radio Transient	23
RXTE	Rossi X-ray Timing Explorer	31
SAS	Science Analysis System (*XMM*)	46
SIS	Solid-state Imaging Spectrometer (*ASCA*)	31
SGR	Soft Gamma Repeater	vii
SNR	Supernova Remnant	1
TES	Transition Edge Sensor	33
MOS	Metal Oxide Semiconductor	31
XINS	X-ray Isolated Neutron Star	10
XIS	X-ray Imaging Spectrometer (*Suzaku*)	31
XMM	X-ray Multimirror Mission	18
XRS	X-ray spectrometer (*Suzaku*)	31

XRT X-ray Telescope (*Suzaku*, *Swift*) 31

BIBLIOGRAPHY

Aguilera, D. N., Pons, J. A., & Miralles, J. A. 2008, ApJ, 673, L167

Albano, A., Turolla, R., Israel, G. L., Zane, S., Nobili, L., & Stella, L. 2010, ApJ, 722, 788

Alpar, M. A. 2007, Ap&SS, 308, 133

Alpar, M. A., Anderson, P. W., Pines, D., & Shaham, J. 1981, ApJ, 249, L29

Arnaud, K. A., George, I. M., & Tennant, A. F. 1992, Legacy, 2, 65

Arons, J. 1983, ApJ, 266, 215

Arras, P., Cumming, A., & Thompson, C. 2004, ApJ, 608, L49

Baade, W., & Zwicky, F. 1934, Proc. Nat. Acad. Sci., 20, 254

Barrett, H. H., & Horrigan, F. A. 1973, Appl. Opt., 12, 2686

Barthelmy, S. D., et al. 2005, Space Sci. Rev., 120, 143

Baykal, A., & Swank, J. 1996, ApJ, 460, 470

Baym, G., Pethick, C., & Pines, D. 1969, Nature, 224, 673

Becker, W., Weisskopf, M. C., Tennant, A. F., Jessner, A., Dyks, J., Harding, A. K., & Zhang, S. N. 2004, ApJ, 615, 908

Beloborodov, A. M. 2009, ApJ, 703, 1044

Beloborodov, A. M., & Thompson, C. 2007, ApJ, 657, 967

Borkowski, K. J., Lyerly, W. J., & Reynolds, S. P. 2001, ApJ, 548, 820

Burke, B. E., Mountain, R. W., Daniels, P. J., Cooper, M. J., & Dolat, V. S. 1994, IEEE Transactions on Nuclear Science, 41, 375

Burrows, D. N., et al. 2000, in Society of Photo-Optical Instrumentation Engineers (SPIE) Conference Series, Vol. 4140, Society of Photo-Optical Instrumentation Engineers (SPIE) Conference Series, ed. K. A. Flanagan & O. H. Siegmund, 64–75

Burwitz, V., Haberl, F., Neuhäuser, R., Predehl, P., Trümper, J., & Zavlin, V. E. 2003, A&A, 399, 1109

Busboom, A., Elders-Boll, H., & Schotten, H. D. 1998, Experimental Astronomy, 8, 97

Camilo, F., Kaspi, V. M., Lyne, A. G., Manchester, R. N., Bell, J. F., D'Amico, N., McKay, N. P. F., & Crawford, F. 2000, ApJ, 541, 367

Camilo, F., Ransom, S., Halpern, J., Reynolds, J., Helfand, D., Zimmerman, N., & Sarkissian, J. 2006, Nature, 442, 892

Camilo, F., Ransom, S. M., Halpern, J. P., & Reynolds, J. 2007a, ApJ, 666, L93

Camilo, F., et al. 2007b, ApJ, 669, 561

Campana, S., Rea, N., Israel, G. L., Turolla, R., & Zane, S. 2007, A&A, 463, 1047

Chang, C., Pavlov, G. G., & Kargaltsev, O. 2011, ApJ, submitted

Chatterjee, P., & Hernquist, L. 2000, ApJ, 543, 368

Chatterjee, P., Hernquist, L., & Narayan, R. 2000, ApJ, 534, 373

Cheng, K. S., Ho, C., & Ruderman, M. 1986a, ApJ, 300, 500

—. 1986b, ApJ, 300, 522

Chevalier, R. A. 2005, ApJ, 619, 839

Cline, T., Frederiks, D. D., Golenetskii, S., Hurley, K., Kouveliotou, C., Mazets, E., & van Paradijs, J. 2000, ApJ, 531, 407

Cocke, W. J., Disney, M. J., & Taylor, D. J. 1969, Nature, 221, 525

Corbet, R. H. D., Smale, A. P., Ozaki, M., Koyama, K., & Iwasawa, K. 1995, ApJ, 443, 786

Cordes, J. M., & Lazio, T. J. W. 2002, astro-ph/0207156

Davies, J. G., Lyne, A. G., & Seiradakis, J. H. 1972, Nature, 240, 229

de Jager, O. C. 1994, ApJ, 436, 239

De Luca, A., Caraveo, P. A., Mereghetti, S., Negroni, M., & Bignami, G. F. 2005, ApJ, 623, 1051

den Herder, J. W., et al. 2001, A&A, 365, L7

Dib, R. 2009, PhD thesis, McGill University (Canada)

Dib, R., Kaspi, V. M., & Gavriil, F. P. 2007, ApJ, 666, 1152

Dib, R., Kaspi, V. M., & Gavriil, F. P. 2008a, in American Institute of Physics Conference Series, Vol. 983, 40 Years of Pulsars: Millisecond Pulsars, Magnetars and More, ed. C. Bassa, Z. Wang, A. Cumming, & V. M. Kaspi, 262–264

Dib, R., Kaspi, V. M., & Gavriil, F. P. 2008b, ApJ, 673, 1044

—. 2008c, ApJ, 673, 1044

—. 2009, ApJ, 702, 614

Duncan, R. C., & Thompson, C. 1992, ApJ, 392, L9

Duncan, R. C., & Thompson, C. 1996, in AIP Conf. Proc. 366: High Velocity Neutron Stars, ed. R. E. Rothschild & R. E. Lingenfelter (New York: AIP Press), 111

Durant, M., & van Kerkwijk, M. H. 2006, ApJ, 650, 1082

Eichler, D., & Shaisultanov, R. 2010, ApJ, 715, L142

Enoto, T., et al. 2009, ApJ, 693, L122

Espinoza, C. M., Lyne, A. G., Kramer, M., Manchester, R. N., & Kaspi, V. M. 2011a, ApJ submitted

Espinoza, C. M., Lyne, A. G., Stappers, B. W., & Kramer, M. 2011b, MNRAS, 538

Esposito, P., et al. 2010, MNRAS, 405, 1787

Fahlman, G. G., & Gregory, P. C. 1981, Nature, 293, 202

Fenimore, E. E., & Cannon, T. M. 1978, Appl. Opt., 17, 337

Feroci, M., et al. 2003, ApJ, 596, 470

Forman, W., Jones, C., Cominsky, L., Julien, P., Murray, S., Peters, G., Tananbaum, H., & Giacconi, R. 1978, ApJS, 38, 357

Gaensler, B. M., Madsen, G. J., Chatterjee, S., & Mao, S. A. 2008, PASA, 25, 184

Gaensler, B. M., van der Swaluw, E., Camilo, F., Kaspi, V. M., Baganoff, F. K., Yusef-Zadeh, F., & Manchester, R. N. 2004, ApJ, 616, 383

Garmire, G. P., Bautz, M. W., Ford, P. G., Nousek, J. A., & Ricker, G. R. 2003, Proc. SPIE, 4851, 28

Gavriil, F. P., Gonzalez, M. E., Gotthelf, E. V., Kaspi, V. M., Livingstone, M. A., & Woods, P. M. 2008, Science, 319, 1802

Gavriil, F. P., & Kaspi, V. M. 2002, ApJ, 567, 1067

—. 2004, ApJ, 609, L67

Gavriil, F. P., Kaspi, V. M., & Woods, P. M. 2002, Nature, 419, 142

—. 2004, ApJ, 607, 959

Gavriil, F. P., Kaspi, V. M., & Woods, P. M. 2006, ApJ, 641, 418

Geppert, U., Küker, M., & Page, D. 2004, A&A, 426, 267

Ghosh, P. 2007, Rotation and Accretion Powered Pulsars (World Scientific Publishing Co)

Giacconi, R., et al. 1979, ApJ, 230, 540

Giaconni, R., Gursky, H., Paolini, F. R., & Rossi, B. 1962, Phys. Rev. Lett., 9, 439

Gold, T. 1968, Nature, 218, 731

Goldreich, P., & Julian, W. H. 1969, ApJ, 157, 869

Gonzalez, M. E., Dib, R., Kaspi, V. M., Woods, P. M., Tam, C. R., & Gavriil, F. P. 2010, ApJ, 716, 1345

Gonzalez, M. E., Kaspi, V. M., Camilo, F., Gaensler, B. M., & Pivovaroff, M. J. 2005, ApJ, 630, 489

Gonzalez, M. E., Kaspi, V. M., Lyne, A. G., & Pivovaroff, M. J. 2004a, ApJ, 610, L37

—. 2004b, ApJ, 610, L37

Gonzalez, M. E., Kaspi, V. M., Pivovaroff, M. J., & Gaensler, B. M. 2006, ApJ, 652, 569

Gotthelf, E. V., & Halpern, J. P. 2007, ApJ, 664, L35

Gotthelf, E. V., Halpern, J. P., Buxton, M., & Bailyn, C. 2004a, ApJ, 605, 368

—. 2004b, ApJ, 605, 368

Gotthelf, E. V., Halpern, J. P., & Dodson, R. 2002, ApJ, 567, L125

Gotthelf, E. V., & Vasisht, G. 1998, New Astronomy, 3, 293

Gotthelf, E. V., Vasisht, G., & Dotani, T. 1999, ApJ, 522, L49

Götz, D., et al. 2007, A&A, 475, 317

Göğüş, E., et al. 2010, ApJ, 718, 331

Gregory, P. C., & Fahlman, G. G. 1980, Nature, 287, 805

Gunson, J., & Polychronopulos, B. 1976, MNRAS, 177, 485

Gursky, H., Solinger, A., Kellogg, E. M., Murray, S., Tananbaum, H., Giacconi, R., & Cavaliere, A. 1972, ApJ, 173, L99+

Güver, T., Özel, F., & Göğüş, E. 2008a, ApJ, 675, 1499

—. 2008b, ApJ, 675, 1499

Güver, T., Özel, F., Göğüş, E., & Kouveliotou, C. 2007, ApJ, 667, L73

Haberl, F. 2007, Ap&SS, 181

Haberl, F., Turolla, R., de Vries, C. P., Zane, S., Vink, J., Méndez, M., & Verbunt, F. 2006, A&A, 451, L17

Haberl, F., et al. 2004, A&A, 424, 635

Halpern, J. P., Gotthelf, E. V., Reynolds, J., Ransom, S. M., & Camilo, F. 2008, ApJ, 676, 1178

Harding, A. K., & Muslimov, A. G. 2001, ApJ, 556, 987

—. 2002, ApJ, 568, 862

Helfand, D. J., Gotthelf, E. V., & Halpern, J. P. 2001, ApJ, 556, 380

Hewish, A., Bell, S. J., Pilkington, J. D. H., Scott, P. F., & Collins, R. A. 1968, Nature, 217, 709

Hobbs, G., Lyne, A. G., Kramer, M., Martin, C. E., & Jordan, C. 2004, MNRAS, 353, 1311

Holloway, N. J. 1973, Nature, 246, 6

Hoyle, F., Narlikar, J., & Wheeler, J. A. 1964, Nature, 203, 914

Hulleman, F., van Kerkwijk, M. H., & Kulkarni, S. R. 2000, Nature, 408, 689

Hulse, R. A., & Taylor, J. H. 1974, ApJ, 191, L59

Hurley, K., et al. 1999, Nature, 397, 41

Hurley, K., et al. 2005, Nature, 434, 1098

Ibrahim, A. I., et al. 2004, ApJ, 609, L21

Irwin, K. D., Hilton, G. C., Wollman, D. A., & Martinis, J. M. 1996, Applied Physics Letters, 69, 1945

Israel, G. L., Campana, S., Dall'Osso, S., Muno, M. P., Cummings, J., Perna, R., & Stella, L. 2007, ApJ, 664, 448

Israel, G. L., Götz, D., Zane, S., Dall'Osso, S., Rea, N., & Stella, L. 2007, A&A, 476, L9

Israel, G. L., et al. 2010, MNRAS, 408, 1387

Iwasawa, K., Koyama, K., & Halpern, J. P. 1992, PASJ, 44, 9

Jackson, M. S., & Halpern, J. P. 2005, ApJ, 633, 1114

Jahoda, K., Markwardt, C. B., Radeva, Y., Rots, A. H., Stark, M. J., Swank, J. H., Strohmayer, T. E., & Zhang, W. 2006, ApJS, 163, 401

Jansen, F., et al. 2001, A&A, 365, L1

Joseph, W. 1979, Nuclear Instrument and Methods, 162, 587

Juett, A. M., Marshall, H. L., Chakrabarty, D., & Schulz, N. S. 2002, ApJ, 568, L31

Kaneko, Y., et al. 2010, ApJ, 710, 1335

Kaplan, D. L., Esposito, P., Chatterjee, S., Possenti, A., McLaughlin, M. A., Camilo, F., Chakrabarty, D., & Slane, P. O. 2009, MNRAS, 400, 1445

Kaplan, D. L., & van Kerkwijk, M. H. 2005, ApJ, 628, L45

Kaplan, D. L., & van Kerkwijk, M. H. 2009a, ApJ, 705, 798

—. 2009b, ApJ, 692, L62

Kargaltsev, O., & Pavlov, G. G. 2008, in American Institute of Physics Conference Series, Vol. 983, 40 Years of Pulsars: Millisecond Pulsars, Magnetars and More, ed. C. Bassa, Z. Wang, A. Cumming, & V. M. Kaspi, 171–185

Kaspi, V. M. 2007, Ap&SS, 308, 1

Kaspi, V. M. 2010, Proceedings of the National Academy of Science, 107, 7147

Kaspi, V. M., & Boydstun, K. 2010, ApJ, 710, L115

Kaspi, V. M., Gavriil, F. P., Chakrabarty, D., Lackey, J. R., & Muno, M. P. 2001, ApJ, 558, 253

Kaspi, V. M., Gavriil, F. P., Woods, P. M., Jensen, J. B., Roberts, M. S. E., & Chakrabarty, D. 2003, ApJ, 588, L93

Kaspi, V. M., & McLaughlin, M. A. 2005, ApJ, 618

Kaspi, V. M., Roberts, M. S. E., & Harding, A. K. 2006, in Compact Stellar X-ray Sources, ed. W. H. G. Lewin & M. van der Klis (UK: Cambridge University Press)

Keller, C. U. 1995, Cell Mole Life Sci, 51, 710

Kern, B., & Martin, C. 2002, Nature, 415, 527

Kippenhahn, R., & Weigert, A. 1967, Zeitschrift fuer Astrophysics, 65, 251

Kondratiev, V. I., McLaughlin, M. A., Lorimer, D. R., Burgay, M., Possenti, A., Turolla, R., Popov, S. B., & Zane, S. 2009, ApJ, 702, 692

Kothes, R., Uyaniker, B. ., & Yar, A. 2002, ApJ, 576, 169

Kouveliotou, C., et al. 1998, Nature, 393, 235

Kouveliotou, C., et al. 2003, ApJ, 596, L79

Koyama, K., Hoshi, R., & Nagase, F. 1987, PASJ, 39, 801

Koyama, K. e. a. 2007, PASJ, 59, 23

Kuiper, L., & Hermsen, W. 2009, A&A, 501, 1031

Kuiper, L., Hermsen, W., den Hartog, P., & Collmar, W. 2006, ApJ, 645, 556

Kumar, H. S., & Safi-Harb, S. 2008, ApJ, 678, L43

—. 2010, ApJ, 725, L191

Landau, L. D. 1938, Nature, 141, 333

Large, M. I., Vaughan, A. E., & Mills, B. Y. 1968, Nature, 220, 340

Laros, J. G., et al. 1987, ApJ, 320, L111

Lattimer, J. M., & Prakash, M. 2001, ApJ, 550, 426

Levin, L., et al. 2010, ApJ, 721, L33

Levine, A. M., Bradt, H., Cui, W., Jernigan, J. G., Morgan, E. H., Remillard, R., Shirey, R. E., & Smith, D. A. 1996, ApJ, 469, L33+

Link, B., & Cutler, C. 2002, MNRAS, 336, 211

Link, B., & Epstein, R. I. 1996, ApJ, 457, 844

Livingstone, M. A., Kaspi, V. M., & Gavriil, F. P. 2005a, ApJ, 633, 1095

—. 2010, ApJ, 710, 1710

Livingstone, M. A., Kaspi, V. M., Gavriil, F. P., & Manchester, R. N. 2005b, ApJ, 619, 1046

Livingstone, M. A., Kaspi, V. M., Gotthelf, E. V., & Kuiper, L. 2006, ApJ, 647, 1286

Livingstone, M. A., Ng, C., Kaspi, V. M., Gavriil, F. P., & Gotthelf, E. V. 2011, ApJ, 730, 66

Longair, M. S. 1997, High Energy Astrophysics, Volume 2 (2nd Edition) (Cambridge: Cambridge University Press)

Lyne, A. G., Pritchard, R. S., Graham-Smith, F., & Camilo, F. 1996, Nature, 381, 497

Lyne, A. G., Pritchard, R. S., & Smith, F. G. 1993, MNRAS, 265, 1003

Lyubarsky, Y., Eichler, D., & Thompson, C. 2002, ApJ, 580, L69

Manchester, R. N., & Hobbs, G. 2011, ApJ, 736, L31+

Manchester, R. N., Hobbs, G. B., Teoh, A., & Hobbs, M. 2005, VizieR Online Data Catalog, 7245, 0

Manchester, R. N., & Taylor, J. H. 1977, Pulsars (San Francisco: Freeman)

Manzali, A., De Luca, A., & Caraveo, P. A. 2007, ApJ, 669, 570

Mazets, E. P., Aptekar, R. L., Butterworth, P. S., Cline, T. L., Frederiks, D. D., Golenetskii, S. V., Hurley, K., & Il'Inskii, V. N. 1999, ApJ, 519, L151

Mazets, E. P., & Golenetskii, S. V. 1981, Ap&SS, 75, 47

Mazets, E. P., Golenetskii, S. V., Ilinskii, V. N., Apetkar, R. L., & Guryan, Y. A. 1979, Nature, 282, 587

McGarry, M. B., Gaensler, B. M., Ransom, S. M., Kaspi, V. M., & Veljkovik, S. 2005, ApJ, 627, L137

McGowan, K. E., Kenea, J. A., Zane, S., Cordova, F. A., Cropper, M., Ho, C., Sasseen, T., & Vestrand, W. T. 2003, ApJ, 591, 380

McGowan, K. E., Vestrand, W. T., Kennea, J. A., Zane, S., Cropper, M., & Córdova, F. A. 2007, Ap&SS, 308, 309

McGowan, K. E., Zane, S., Cropper, M., Vestrand, W. T., & Ho, C. 2006, ApJ, 639, 377

McLaughlin, M. A., et al. 2003, ApJ, 591, L135

McLaughlin, M. A., et al. 2006, Nature, 439, 817

Melikidze, G. I., Gil, J., & Szary, A. 2007, in WE-Heraeus Seminar on Neutron Stars and Pulsars 40 years after the Discovery, ed. W. Becker & H. H. Huang, 157–+

Mereghetti, S. 2008a, A&A Rev., 15, 225

—. 2008b, A&A Rev., 15, 225

Mereghetti, S., Götz, D., Mirabel, I. F., & Hurley, K. 2005, A&A, 433, L9

Misanovic, Z., Pavlov, G. G., & Garmire, G. P. 2008, ApJ, 685, 1129

Misanovic, Z., Pavlov, G. G., & Kargaltsev, O. 2011, ApJ, in preparation

Mitsuda, K. e. a. 2007, PASJ, 59, 1

Morii, M., Sato, R., Kataoka, J., & Kawai, N. 2003, PASJ, 55, L45

Morii, M., et al. 2008, in American Institute of Physics Conference Series, Vol. 983, 40 Years of Pulsars: Millisecond Pulsars, Magnetars and More, ed. C. Bassa, Z. Wang, A. Cumming, & V. M. Kaspi, 268–270

Muslimov, A. G., & Harding, A. K. 2004, ApJ, 606, 1143

Ng, C., Slane, P. O., Gaensler, B. M., & Hughes, J. P. 2008, ApJ, 686, 508

Ng, C.-Y., & Kaspi, V. M. 2010, ArXiv:1010.4592

Ng, C.-Y., Romani, R. W., Brisken, W. F., Chatterjee, S., & Kramer, M. 2007, ApJ, 654, 487

Ng, C.-Y., et al. 2011, ApJ, 729, 131

Ohashi, T. e. a. 1996, PASJ, 48, 157

Olausen, S. A., Kaspi, V. M., Lyne, A. G., & Kramer, M. 2010, ApJ, 725, 985

Ostriker, J. P., & Gunn, J. E. 1969, ApJ, 157, 1395

Özel, F. 2001, ApJ, 563, 276

Özel, F., & Guver, T. 2007, ApJ, 659, L141

Özel, F., Güver, T., & Göğüş, E. 2008, in American Institute of Physics Conference Series, Vol. 983, 40 Years of Pulsars: Millisecond Pulsars, Magnetars and More, ed. C. Bassa, Z. Wang, A. Cumming, & V. M. Kaspi, 254–258

Pacini, F. 1967, Nature, 216, 567

—. 1968, Nature, 219, 145

Paczyński, B. 1971, ARAA, 9, 183

Paczyński, B. 1992, Acta Astron., 42, 145

Page, D., Geppert, U., & Weber, F. 2006, Nuclear Physics A, 777, 497

Pavlov, G. G., Kargaltsev, O., & Brisken, W. F. 2008, ApJ, 675, 683

Pavlov, G. G., Sanwal, D., & Zavlin, V. E. 2006, ApJ, 643, 1146

Pavlov, G. G., Shibanov, Y. A., Zavlin, V. E., & Meyer, R. D. 1995, in The Lives of the Neutron Stars (NATO ASI Series), ed. A. Alpar, Ü. Kiziloğlu, & J. van Paradis (Dordrecht: Kluwer), 71–90

Pines, D. 1980, Science, 207, 597

Pivovaroff, M., Kaspi, V. M., & Camilo, F. 2000, ApJ, 535, 379

Pons, J. A., Link, B., Miralles, J. A., & Geppert, U. 2007, Physical Review Letters, 98, 071101

Radhakrishnan, V., & Manchester, R. N. 1969, Nature, 222, 228

Rea, N., & Esposito, P. 2011, in High-Energy Emission from Pulsars and their Systems, ed. D. F. Torres & N. Rea, 247–+

Rea, N., Oosterbroek, T., Zane, S., Turolla, R., Méndez, M., Israel, G. L., Stella, L., & Haberl, F. 2005, MNRAS, 361, 710

Rea, N., Zane, S., Turolla, R., Lyutikov, M., & Götz, D. 2008, ApJ, 686, 1245

Rea, N., et al. 2009a, ApJ, 703, L41

—. 2009b, MNRAS, 396, 2419

—. 2010, Science, 330, 944

Richards, D. W., & Comella, J. M. 1969, Nature, 222, 551

Ruderman, M. 1969, Nature, 223, 597

Ruderman, M. A., & Sutherland, P. G. 1975, ApJ, 196, 51

Safi-Harb, S., & Kumar, H. S. 2008, ApJ, 684, 532

Sasaki, M., Plucinsky, P. P., Gaetz, T. J., Smith, R. K., Edgar, R. J., & Slane, P. O. 2004, ApJ, 617, 322

Sato, T., Bamba, A., Nakamura, R., & Ishida, M. 2010, PASJ, 62, L33

Scholz, P., & Kaspi, V. M. 2011, ApJ in press

Schreier, E., Levinson, R., Gursky, H., Kellogg, E., Tananbaum, H., & Giacconi, R. 1972, ApJ, 172, L79+

Schwope, A. D., Hambaryan, V., Haberl, F., & Motch, C. 2007, Ap&SS, 308, 619

Shapiro, S. L., & Teukolsky, S. A. 1983, Black Holes, White Dwarfs and Neutron Stars. The Physics of Compact Objects (New York: Wiley–Interscience)

Shklovsky, I. S. 1967, ApJ, 148, L1+

Slane, P. 1994, ApJ, 437, 458

Slane, P., Helfand, D. J., van der Swaluw, E., & Murray, S. S. 2004, ApJ, 616, 403

Smith, R. C. 1995, Observational Astrophysics

Snowden, S. L. 2002, ArXiv:astro-ph/0203311

Staelin, D. H., & Reifenstein, III, E. C. 1968, Science, 162, 1481

Strüder, L., et al. 2001, A&A, 365, L18

Sturrock, P. A. 1971, ApJ, 164, 529

Tam, C. R., Gavriil, F. P., Dib, R., Kaspi, V. M., Woods, P. M., & Bassa, C. 2008, ApJ, 677, 503

Tam, C. R., Kaspi, V. M., Gaensler, B. M., & Gotthelf, E. V. 2006, ApJ, 652, 548

Tam, C. R., Kaspi, V. M., van Kerkwijk, M. H., & Durant, M. 2004, ApJ, 617, L53

Tanaka, Y., Inoue, H., & Holt, S. S. 1994, PASJ, 46, L37

Tananbaum, H., Gursky, H., Kellogg, E. M., Levinson, R., Schreier, E., & Giacconi, R. 1972, ApJ, 174, L143+

Thompson, C., & Duncan, R. C. 1993, ApJ, 408, 194

Thompson, C., & Duncan, R. C. 1995, MNRAS, 275, 255

Thompson, C., & Duncan, R. C. 1996, ApJ, 473, 322

Thompson, C., Lyutikov, M., & Kulkarni, S. R. 2002, ApJ, 574, 332

Tiengo, A., Mereghetti, S., Turolla, R., Zane, S., Rea, N., Stella, L., & Israel, G. L. 2005, A&A, 437, 997

Torii, K., Kinugasa, K., Katayama, K., Tsunemi, H., & Yamauchi, S. 1998, ApJ, 503, 843

Truemper, J. 1993, Science, 260, 1769

Turner, M. J. L., et al. 2001, A&A, 365, L27

Turolla, R. 2009, in Astrophysics and Space Science Library, ed. W. Becker, Vol. 357, 141

van der Horst, A. J., et al. 2010, ApJ, 711, L1

van Kerkwijk, M. H., & Kaplan, D. L. 2008, ApJ, 673, L163

van Paradijs, J., Taam, R. E., & van den Heuvel, E. P. J. 1995, A&A, 299, L41

Vancura, O., Blair, W. P., Long, K. S., & Raymond, J. C. 1992, ApJ, 394, 158

Vanderhill, M. J., Borken, R. J., Bunner, A. N., Burstein, P. H., & Kraushaar, W. L. 1975, ApJ, 197, L19

Vasisht, G., & Gotthelf, E. V. 1997, ApJ, 486, L129

Vasisht, G., Gotthelf, E. V., Torii, K., & Gaensler, B. M. 2000, ApJ, 542, L49

Wang, Z., Bassa, C., Kaspi, V. M., Bryant, J. J., & Morrell, N. 2008, ApJ, 679, 1443

Weisskopf, M. C., Brinkman, B., Canizares, C., Garmire, G., Murray, S., & Van Speybroeck, L. P. 2002, PASP, 114, 1

Weisskopf, M. C., O'Dell, S. L., Paerels, F., Elsner, R. F., Becker, W., Tennant, A. F., & Schwarz, D. A. 2004, ApJ, 601, 1050

Wells, D. C., Greisen, E. W., & Harten, R. H. 1981, A&AS, 44, 363

Weltevrede, P., Johnston, S., & Espinoza, C. M. 2011, MNRAS, 411, 1917

Wolter, H. 1952, Ann. Physik, 10, 94

Woods, P. M., Kaspi, V. M., Gavriil, F. P., & Airhart, C. 2011, ApJ, 726, 37

Woods, P. M., Kouveliotou, C., Göğüş, E., Finger, M. H., Swank, J., Smith, D. A., Hurley, K., & Thompson, C. 2001, ApJ, 552, 748

Woods, P. M., & Thompson, C. 2006, in Compact Stellar X-ray Sources, ed. W. H. G. Lewin & M. van der Klis (UK: Cambridge University Press)

Woods, P. M., et al. 1999, ApJ, 519, L139

Woods, P. M., et al. 1999, ApJ, 524, L55

—. 2004, ApJ, 605, 378

—. 2005, ApJ, 629, 985

Zane, S., Albano, A., Turolla, R., Israel, G. L., Nobili, L., & Stella, L. 2011, ArXiv e-prints

Zane, S., Cropper, M., Turolla, R., Zampieri, L., Chieregato, M., Drake, J. J., & Treves, A. 2005, ApJ, 627, 397

Zavlin, V. E., Pavlov, G. G., & Shibanov, Y. A. 1996, A&A, 315, 141

Zhu, W., & Kaspi, V. M. 2010, ApJ, 719, 351

Zhu, W., Kaspi, V. M., Dib, R., Woods, P. M., Gavriil, F. P., & Archibald, A. M. 2008, ApJ, 686, 520

Zhu, W., Kaspi, V. M., Gonzalez, M. E., & Lyne, A. G. 2009, ApJ, 704, 1321

Zhu, W. W., Kaspi, V. M., McLaughlin, M. A., Pavlov, G. G., Ng, C.-Y., Manchester, R. N., Gaensler, B. M., & Woods, P. M. 2011, ApJ, 734, 44

Zombeck, M. V., Chappell, J. H., Kenter, A. T., Moore, R. W., Murray, S. S., Fraser, G. W., & Serio, S. 1995, in Society of Photo-Optical Instrumentation Engineers (SPIE) Conference Series, Vol. 2518, Society of Photo-Optical Instrumentation Engineers (SPIE) Conference Series, ed. O. H. Siegmund & J. V. Vallerga, 96–106